Structural Parameters of Compact Stellar Systems

Juan Pablo Madrid

Presented in fulfillment of the requirements
of the degree of Doctor of Philosophy

May 2013

Faculty of Information and Communication Technology
Swinburne University

Abstract

The objective of this thesis is to establish the observational properties and structural parameters of compact stellar systems that are brighter or larger than the "standard" globular cluster. We consider a standard globular cluster to be fainter than $M_V \sim -11$ mag and to have an effective radius of ∼3 pc. We perform simulations to further understand observations and the relations between fundamental parameters of dense stellar systems. With the aim of establishing the photometric and structural properties of Ultra-Compact Dwarfs (UCDs) and extended star clusters we first analyzed deep F475W (Sloan g) and F814W (I) Hubble Space Telescope images obtained with the Advanced Camera for Surveys. We fitted the light profiles of ∼5000 point-like sources in the vicinity of NGC 4874 — one of the two central dominant galaxies of the Coma cluster. Also, NGC 4874 has one of the largest globular cluster systems in the nearby universe. We found that 52 objects have effective radii between ∼10 and 66 pc, in the range spanned by extended star clusters and UCDs. Of these 52 compact objects, 25 are brighter than $M_V \sim -11$ mag, a magnitude conventionally thought to separate UCDs and globular clusters. We have discovered both a red and a blue subpopulation of Ultra-Compact Dwarf (UCD) galaxy candidates in the Coma galaxy cluster.

Searching for UCDs in an environment different to galaxy clusters we found eleven Ultra-Compact Dwarf and 39 extended star cluster candidates associated with the fossil group NGC 1132. UCD and extended star cluster candidates are identified through the analysis of their structural parameters, colors, spatial distribution, and luminosity using deep Hubble Space Telescope observations in two filters: the F475W (Sloan g) and F850LP (Sloan z). Two types of UCDs are identified in the vicinity of NGC 1132, one type shares the same color and luminosity of the brightest globular clusters and traces the onset of the mass-size relation. The second kind of UCD is represented by the brightest UCD candidate, a M32-type object, with an effective radius of $r_h = 77.1$ pc, located at ~ 6.6 kpc from the nucleus of NGC 1132. This UCD candidate is likely the remaining nucleus of a minor merger with the host galaxy. UCDs are found to extend the mass-metallicity relation found in globular clusters to higher luminosities.

A spectroscopic follow up of Ultra-Compact Dwarf candidates in the fossil group NGC 1132 is undertaken with the Gemini Multi Object Spectrograph (GMOS). These new Gemini spectra confirm the presence of six UCDs in the fossil group NGC 1132. The ensemble of UCDs have an average radial velocity of $< v_r >= 6966 \pm 85$ km/s and a velocity dispersion of $\sigma_v = 169 \pm 18$ km/s characteristic of poor galaxy groups.

To determine the physical mechanisms that shape the size and mass distribution of

compact stellar systems we carry out direct N-body simulations in a realistic Milky Way-like potential using the code NBODY6. Based on these simulations a new relationship between scale size and galactocentric distance is derived: the scale size of star clusters is proportional to the hyperbolic tangent of the galactocentric distance. The half-mass radius of star clusters increases systematically with galactocentric distance but levels off when star clusters orbit the galaxy beyond $\sim$40 kpc. These simulations show that the half-mass radius of individual star clusters varies significantly as they evolve over a Hubble time, more so for clusters with shorter relaxation times, and remains constant through several relaxation times only in certain situations when expansion driven by the internal dynamics of the star cluster and the influence of the host galaxy tidal field balance each other. Indeed, the radius of a star cluster evolving within the inner 20 kpc of a realistic galactic gravitational potential is severely truncated by tidal interactions and does not remain constant over a Hubble time. Furthermore, the half-mass radius of star clusters measured with present day observations bears no memory of the original cluster size. Stellar evolution and tidal stripping are the two competing physical mechanisms that determine the present day size of globular clusters. These simulations also show that extended star clusters when formed at large galactocentric distances can remain fully bound to the host galaxy.

Direct N-body simulations of globular clusters in a realistic Milky Way-like potential are also carried out using the code NBODY6 to determine the impact of the host galaxy disk mass and geometry on the survival of star clusters. A relationship between disk mass and star cluster dissolution timescale is derived. These N-body models show that doubling the mass of the disk from 5×10^{10} $M_{\odot}$ to 10×10^{10} $M_{\odot}$ halves the dissolution time of a satellite star cluster orbiting the host galaxy at 6 kpc from the galactic center. Different geometries in a disk of identical mass can determine either the survival or dissolution of a star cluster orbiting within the inner 6 kpc of the galactic center. Disk geometry has measurable effects on the mass loss of star clusters up to 15 kpc from the galactic center. A simulation performed at 6 kpc from the galactic center with a fine output time step show that at each disk crossing the outer layers of star clusters experience an increase in velocity dispersion of $\sim$0.11 km/s, or 5.2% of the average velocity dispersion in the outer section of star clusters.

Acknowledgements

It is my pleasure to thank my supervisor Jarrod Hurley for his support and invaluable input during this work. Jarrod was always available and invariably in good spirits during all of our interactions in the past years. I am grateful for Jarrod's advice that spanned many aspects of my life. I am most privileged to have worked with Jarrod as my supervisor for this endeavour.

I would like to thank my associate supervisor Alister Graham for supporting the application that enabled me to receive the fellowship that I used to do this work. Alister also gave important input for the work carried out during the first part of my PhD.

My wife Laura Schwartz moved to Australia thus allowing me to carry out this PhD thesis. Without her support this work would not have been possible.

I would like to thank Matthew Bailes for building the Centre for Astrophysics and Supercomputing (CAS) where this work was carried out. CAS became a research centre known worldwide under his leadership. Matthew was also a champion of students interests and wellbeing during his tenure as Director of the Centre. Elizabeth Thackray took diligent care of endless administrative taks making my life much easier, thank you.

I would like to thank Carlos Donzelli from the Córdoba Observatory in Argentina for his unmatched hospitality during two productive visits while doing this PhD.

The Centre for Astrophysics at Swinburne University has a student body from all corners of the world making it a unique United Nations of Astrophysics. I would like to thank Annie Hughes for her insightful advice during this thesis, I very much missed Annie's presence and input during the second part of this PhD. Anna Sippel and Guido Moyano were great team members and helped me solve many bugs encountered in the simulations presented here. The following students, postdocs, and their partners were helpful in many different ways during the completion of this work: Francesco Pignatale, Carlos Contreras, Jeff Cooke, Evelyn Caris, Adrian Malec, Paul Coster, Peter Jensen, Sofie Ham, Gonzalo Diaz, Bil Dullo, Lina Levin, Kathrin Wolfinger, Ben Barsdell, Marie Martig, Jonathan Whitmore, Lee Spitler, Anna Zelenko, Max Bernyk, Giulia Savorgnan, Rebecca Allen.

Facilities and Funding Acknowledgements

Parts of this thesis are based on observations made with the NASA/ESA Hubble Space Telescope, obtained at the Space Telescope Science Institute, which is operated by AURA, Inc., under NASA contract NAS5-26555.

Part of this thesis is based on observations obtained at the Gemini Observatory, which is operated by the Association of Universities for Research in Astronomy, Inc., under a cooperative agreement with the NSF on behalf of the Gemini partnership: the National Science Foundation (United States), the Science and Technology Facilities Council (United Kingdom), the National Research Council (Canada), CONICYT (Chile), the Australian Research Council (Australia), Ministério da Ciência, Tecnologia e Inovação (Brazil) and Ministerio de Ciencia, Tecnología e Innovación Productiva (Argentina). The Gemini data for this thesis were obtained under program GN-2012B-Q-10 of the Argentinian time share.

Analysis of the Gemini data was funded with a travel grant from the Australian Nuclear Science and Technology Organization (ANSTO). The access to major research facilities is supported by the Commonwealth of Australia under the International Science Linkages Program.

Most of the simulations presented in this work were performed on the gSTAR national facility at Swinburne University of Technology. gSTAR is funded by Swinburne and the Australian Government Education Investment Fund.

Thesis Publications

Madrid, J. P., Graham, A. W., Harris, W. E., Goudfrooij, P., Forbes, D. A., Carter, D. Blakeslee, J. P., Spitler, L. R., Ferguson, H. C. 2010, "Ultra-Compact Dwarfs in the Core of the Coma Cluster", *The Astrophysical Journal*, 722, 1707.

Madrid, J. P., 2011, "Ultra-compact Dwarfs in the Fossil Group NGC 1132", *The Astrophysical Journal Letters*, 737, L13.

Madrid, J. P., Hurley, J. R., Sippel, A. C., 2012, " The Size Scale of Star Clusters", *The Astrophysical Journal*, 756, 167.

Madrid, J. P. & C. J. Donzelli 2013, "Gemini Spectroscopy of Ultra-Compact Dwarfs in the Fossil Group NGC 1132", *The Astrophysical Journal*, 770, 158.

Madrid, J. P., Hurley, J. R., Martig, M., 2013, "The Impact of Galaxy Geometry and Mass Evolution on the Survival of Star Clusters", submitted to *The Astrophysical Journal*

Declaration

This thesis contains no material that has been accepted for the award of any other degree or diploma. To the best of my knowledge, this Thesis contains no material previously published or written by another author, except where due reference is made in the text of the thesis. All work presented is that of the author. All figures and text were created by the author and I remain solely responsible for this work, with the exceptions listed below.

Much of the material in Chapters 2 through 5 was drawn from the publications Madrid et al. (2010), Madrid (2011), Madrid et al. (2012), Madrid & Donzelli (2013), and Madrid et al. (2013). I acknowledge helpful discussions and critical feedback that were provided by my co-authors and the anonymous referees during the preparation of these publications. Both my principal and associate supervisors were coauthors of the relevant publications during which I received their guidance and input.

Madrid et al. (2010) is based on data acquired during the Hubble Space Telescope General Observer Program 10861. As it is common practice in this field, this paper has several coauthors for different reasons: David Carter was the Principal Investigator of the Coma Cluster Treasury Survey. Harry Ferguson was the United States administrative Co-I and Paul Goodfrooij was responsible for the data release used in the paper. Bill Harris, John Blakeslee, Duncan Forbes and Lee Spitler provided enlightening editorial comments, suggested research pathways, caught several typos, and suggested relevant references, often their own. I am thankful to them for supporting this project.

Madrid, Hurley, & Sippel (2012) has fellow team member Anna Sippel as a coauthor in recognition of her help debugging the simulations and her technical guidance with `NBODY6`.

Madrid & Donzelli (2013) Carlos Donzelli provided importance guidance during the reduction of the Gemini Multi-Object Spectrograph data.

Madrid, Hurley, & Martig (2013) has Marie Marig as a coauthor for her input setting up the initial values of the simulations presented in this publication. Marie also provided several relevant references.

I would like to thank Ingo Misgeld for providing Figure 1.1 of this thesis and the explicit permission to reproduce it in this work. This figure was originally published under Misgeld

& Hilker (2011).

Narae Hwang kindly converted the x-axis of Figure 5.5 to kiloparsecs in order to facilitate my comparison with the simulations presented in Chapter 5. This figure was originally published in Hwang et al. (2011) and is reproduced here with permission.

Figure 3.1 was made with the same HST data used for the study of the Fossil Group NGC 1132, the color composition and layout were made by the Hubble Heritage Team. All images created by this team are free of copyright.

I am responsible for the entire text and content of this work.

Juan P. Madrid
May 2013

Contents

List of Tables

List of Figures

1 Introduction

1.1 Fundamental Structural Parameters of Compact Stellar Systems

Globular clusters are spherical associations of thousands or even millions of stars held together by gravity. In our galaxy, globular clusters are located in the halo and are believed to be one of the oldest stellar systems of the universe (older than 11 billion years). Open clusters are the younger relatives of globular clusters with ages of less than 10 billion years and are located around the plane of the galactic disk. Open clusters often contain gas and dust contrary to globular clusters which are believed to have lost all their gas and dust content. Open clusters are also less dense, and generally less massive than globular clusters. Globular clusters are an increasingly diverse family. During the last decade the discovery of stellar systems brighter, larger, and more massive than the "standard" star cluster has blurred the distinction between globular clusters and dwarf galaxies.

We consider a standard globular cluster to be fainter than $M_V \sim -11$ mag and to have an effective radius of $\sim$3 pc. This thesis is aimed at studying the photometric and structural parameters of compact stellar systems ranging from star clusters to Ultra-Compact Dwarf galaxies (UCDs; Phillipps et al. 2001). We also intend to understand the physical mechanisms that shape the size distribution of these low mass stellar systems going from 10^4 to $10^6 M_\odot$. Indeed, the linear scale sizes of low-mass stellar systems such as open clusters, globular clusters, nuclear star clusters, extended star clusters, and Ultra-Compact Dwarfs are determined by physical factors that are poorly understood. The variables influencing the size of these stellar systems, generally satellites of a host galaxy, are many and the parameter space of these variables is vast. Factors that carve the observed size distribution of stellar structures are, among others, the orbits and distance to the center of the host galaxy at which star clusters evolve, their metallicity, concentration,

stellar populations, and environment (e.g. Bertin & Varri 2008). The presence of black holes, either stellar or of intermediate mass, has severe implications for the dynamical evolution of low-mass stellar systems as well (Baumgardt et al. 2004).

Star clusters in the mass range from 10^4 to $10^6 M_\odot$ remain outside the resolution of cosmological simulations that seek to represent the large scale structure of the universe. A notable attempt to model the formation of globular cluster formation in cosmological simulations was made by Kravtsov & Gnedin (2005). Established observational results such as the almost universal size of globular clusters (half-light radius of $\sim$3 pc: Jordán et al. 2005) remain unexplained. Moreover, galactic globular clusters either underfill or overfill the radius predicted by tidal theory (Webb et al. 2013). Extended star clusters found by Mackey et al. (2006) in the Andromeda galaxy are in better agreement with tidal theory: these are objects with sizes between those of globular clusters and UCDs (Harris et al. 2011).

Through a combination of observations and numerical simulations we will determine the major physical mechanisms that build the size distribution of observed star clusters. We will be able to better understand the mass loss rates of low-mass stellar systems over a Hubble time and attempt to solve some of the following outstanding questions: What are the physical mechanisms that make a primordial stellar system become a globular cluster, an extended star cluster or a UCD? What are the true scaling relations of hot stellar systems (Misgeld & Hilker 2011)?

1.2 Scale Sizes and Color Bimodality of Globular Cluster Systems

From an observational stand point the half-light radius (r_h) is a structural parameter of star clusters that is often measured. This radius, also usually referred to as the effective radius, is the radius that contains half of the light of a star cluster or stellar system in general. Other radii commonly used to estimate the sizes of star clusters and easily obtained in numerical simulations are the half-mass radius, and the tidal radius. The former is self described by its name and the latter is the distance from the center where the gravitational force of the cluster and that of the external field imposed by the galaxy balance each other. We will see in Chapter 5 that half-light radius and half-mass radius are proportional to each other with a proportionality constant of order unity.

Reliable structural parameters of star clusters were initially obtained in the Milky Way and the Local Group. The second and third generation of instruments onboard the Hubble

Space Telescope such as the Wide Field Planetary Camera 2 (WFCP2) enabled precise photometry and measurements of the effective radius of globular clusters out to the Virgo distance (16.1 Mpc; Tonry et al. 2001). For instance, Kundu et al. (1999) were able to determine the median size of globular clusters in M87 to be $r_h = 2.5$ pc, similar to the median size of clusters in the Milky Way which is $r_h = 3.0$ pc.

Larsen et al. (2001) used WFPC2 data to study the globular cluster systems of 17 nearby elliptical galaxies, and were able to establish general trends and shared characteristics of extragalactic globular cluster systems. The bimodal color distribution of globular clusters is one of the important observations carried out by Larsen et al. (2001). For most of the 17 globular cluster systems studied by these authors, two Gaussians provide a much better fit than a single Gaussian to the color distribution of globular clusters. Globular cluster systems are thus divided into two subpopulations: a blue, metal-poor subpopulation, and a red, metal-rich subpopulation. Spectroscopic evidence of this bimodality has existed since the early 80s (e.g. Zinn & West 1984). The origin of this color bimodality is to this day the subject of debate and has been explained only by *ad hoc* hypotheses (e.g. West et al. 2004) with the recent exception of Tonini (2013). Interestingly Larsen et al. (2001) find that red (metal-rich) globular clusters are 20% smaller than blue (metal-poor) globular clusters.

Like most galaxies with rich Globular Cluster Systems (GCSs), the cD galaxies of Virgo (M87: Peng et al. 2009; Harris 2009b) and Fornax (NGC 1399: Dirsch et al. 2003) display evident bimodality in their color distribution. Bimodal fits to the GCS around NGC 3311, the central cD galaxy of the Hydra galaxy cluster, also reveal the presence of a red (metal-rich) and a blue (metal-poor) subpopulation (Wehner et al. 2008). Six additional giant elliptical galaxies studied by Harris (2009a) also show clear bimodality.

The paradigmatic color bimodality of globular cluster systems (Brodie & Strader 2006) brings a new interesting question to the field: metal-rich clusters are more compact than their metal poor counterparts (e.g. Madrid et al. 2009). This established observational fact received only ailing theoretical explanations until the recent work of Sippel et al. (2012) who show using numerical simulations that metallicity effects can account for the observable size differences.

A challenge to the metallicity bimodality was posited by Yoon et al. (2006). These authors agree the observational results reporting color bimodality in globular cluster systems. Yoon et al. (2006), however, challenge the assumption that this observed color bimodality translates into a metallicity bimodality. In order to have a metallicity bimodality derived from observations of colors the relationship between color and metallicity needs to be

linear. Yoon et al. (2006) showed that non-linear color-metallicty relations exist. The results of Yoon et al. (2006) were in turn challenged by more recent work that claims that the observed color bimodality reflects an underlying bimodal metallicity distribution (e.g. Brodie et al. 2012).

The Advanced Camera for Surveys (ACS) onboard the HST with its superb resolution and bigger field of view had a positive and significant impact on our understanding of extra-galactic globular cluster systems (Brodie & Strader 2006). ACS provided data of exquisite photometric accuracy and a somewhat large field of view ($202'' \times 202''$ Mack et al. 2003). The ACS Virgo Cluster Survey (ACS VCS) set a milestone in our understanding of globular clusters by studying the properties of 100 globular cluster systems associated with galaxies of the Virgo Cluster. Jordán et al. (2005, ACS VCS Paper X) measured the effective radius of thousands of globular clusters and established that the effective radius is independent of luminosity. Jordán et al. (2005) also find that r_h increases with increasing galactocentric distance, a fact that was missed by early studies using WFPC2. Kundu et al. (1999) failed to observe the increase of r_h with projected galactocentric distance for the globular clusters associated with M87 using WFCP2 data – the trend is apparent for this galaxy with the wider field of view of the ACS (Jordán et al. 2005, Madrid et al. 2009).

1.3 Mind the Gap in the Fundamental Plane Relations of Compact Stellar Systems

Star clusters have traditionally defined a narrow set of relations between fundamental structural parameters (Harris 2010). Within the parameter space defined by size and magnitude star clusters appeared to have a branch on their own, distinct from elliptical galaxies and also different from dwarf spheroidals galaxies, see Figure 1.1 (Misgeld & Hilker 2011).

There is an alleged discontinuity in the fundamental relations between compact elliptical galaxies and globular clusters (Misgeld & Hilker 2011) highlighted by a marked scarcity of compact stellar systems with characteristic scale sizes between 10 and 100 parsecs. A clear gap in the distribution of compact stellar systems is also found in the Faber-Jackson (1976) relation of velocity dispersion and magnitude. Is the gap in the structural relations between 10 and 100 parcsecs real or the product of selection effects?

Gilmore et al. (2007) have interpreted the gap in the parameter space defined by compact stellar systems as a sign of two distinct families of objects, reflecting the intrinsic properties of dark matter. Globular clusters would belong to a family of dark matter-free

stellar systems while dwarf and compact ellipticals form the branch where dark matter is present or even dominant. Gilmore et al. (2007) postulate that dark matter halos have cored mass distributions with characteristic scale sizes of more than 100 pc. It is accepted that globular clusters have no dark matter. Ultra-Compact Dwarfs and compact ellipticals have higher mass-to-light ratios than globular clusters and might be the smallest luminous stellar systems with dark matter (Hasegan et al. 2005). Compact ellipticals might also harbor supermassive black holes, see the discussion of Graham (2002) on M32.

Compact elliptical galaxies are indeed rare, but is the range in sizes between 10 and 100 pc truly forbidden for stellar systems? Historically, most studies working on the Fundamental Plane relations of compact stellar systems focus on either globular clusters with a characteristic scale size of 3 pc (Jordán et al. 2005) or elliptical galaxies with sizes greater than 100 pc (Misgeld & Hilker 2011).

1.4 Brighter, Larger, and More Massive than the Standard Globular Cluster

Compact stellar systems that deviate in size from the standard $\sim 2.5 - 3$ pc radius of globular clusters have received much attention and have been reported and discussed in the literature during the last decade. Those compact stellar systems larger and brighter than globular clusters such as Ultra-Compact Dwarfs have structural parameters that place them in the gap discussed above.

Ultra-compact dwarfs are a relatively newly discovered class of stellar system (Hilker et al. 1999; Drinkwater et al. 2000) and their origin is not yet clearly established. In color, and structural parameters, UCDs lie between supermassive globular clusters and compact dwarf elliptical galaxies. Not surprisingly, the origin of UCDs has been linked to both globular clusters and dwarf elliptical galaxies (Hilker 2006, and references therein). The defining characteristics of Ultra-Compact Dwarfs are sizes between 10 and 100 parsecs (i.e. in the size scale *gap*), masses between 10^4 to $10^6 M_{\odot}$, and are generally considered to be brighter than $M_V \sim -11$ mag (Mieske et al. 2006).

UCDs are typically associated with galaxy clusters and were originally identified in Fornax (Hilker et al. 1999; Drinkwater et al. 2000, 2003). Subsequent searches in other galaxy clusters revealed that, far from being an oddity to Fornax, UCDs were present in all major galaxy clusters in the nearby universe. Indeed, the presence of UCDs was reported in several additional galaxy clusters: Virgo, Centaurus, Hydra, Abell S040 and Abell 1689 (Evstigneeva et al. 2008; Chilingarian & Mamon 2008; Mieske et al. 2004,

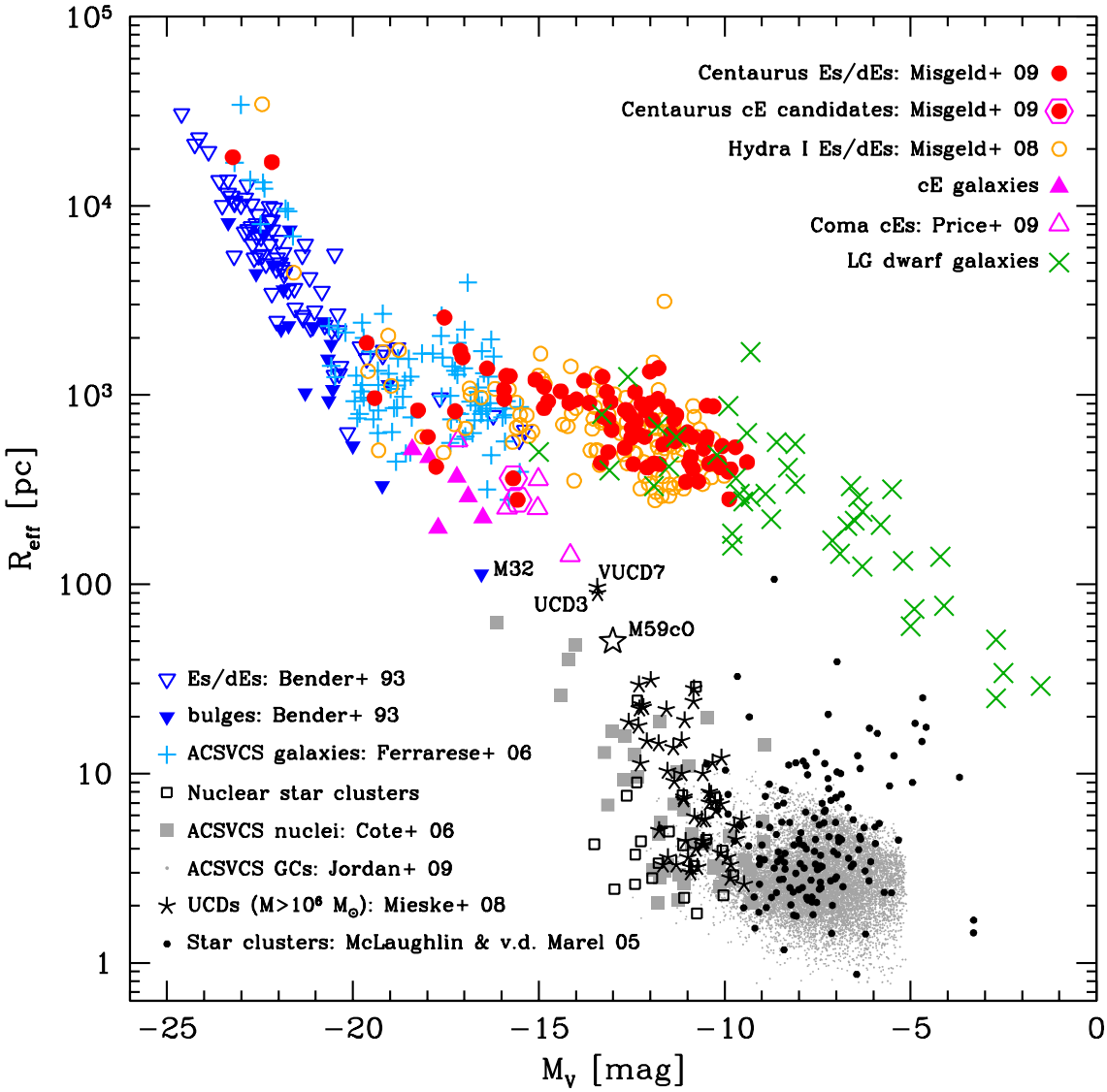

Figure 1.1 Size-Luminosity Diagram for hot stellar systems over ten orders of magnitude in mass (Misgeld & Hilker 2011). Figure kindly provided by Ingo Misgeld and reproduced with permission. cE stands for compact elliptical galaxies, and LG dwarf stands for Local Group dwarf galaxies, i.e. dwarf spheroidals and ultra-faint dwarfs.

2007; Wehner & Harris 2007; Blakeslee & Barber DeGraaff 2008). However, Romanowsky et al. (2009) report the presence of UCDs in the galaxy group hosting NGC 1407. Most recently, a spectroscopically confirmed UCD in the low density environment surrounding the Sombrero Galaxy was discovered by Hau et al. (2009). See also Brüns & Kroupa (2012) and their comprehensive set of references therein. UCDs are difficult to find since they are often mistaken for stars, or simply bright globular clusters, and their structural parameters can only be derived using the Hubble Space Telescope. The formation of UCDs and possible links between UCDs and globular clusters (either red or blue) remains a subject of debate.

In the analysis of the color-magnitude diagram (CMD) of the NGC 3311 GCS, Wehner & Harris (2007; their Figure 1) find an "upward" extension towards brighter magnitudes of the red subpopulation. This continuation to brighter magnitudes (and higher masses) is absent among the blue subpopulation. Wehner & Harris (2007) postulate that given their magnitudes ($i' \leq 22.5$ mag) and inferred masses ($> 6 \times 10^6 M_\odot$), the extension of the CMD corresponds to Ultra-Compact Dwarfs. While Wehner & Harris (2007) suggest that UCDs are the bright extension of the GCS, the ground-based data used for their work do not allow them to derive characteristic radii for their UCD candidates. Peng et al. (2009) over-plotted 18 objects with extended effective radii ($r_h > 10$ pc) on their CMD of the M87 GCS. Some of these objects are confirmed UCDs or Dwarf/Globular Transition Objects (Hasegan et al. 2005) and most of them lie exactly at the bright end of the blue subpopulation of globular clusters. Are UCDs the extension to brighter magnitudes of the blue or the red subpopulation of globular clusters?

1.5 Fainter but Larger than the Standard Globular Cluster

During the last decade discoveries of stellar systems larger than globular clusters and not necessarily brighter have also been reported – some of these new systems are even fainter than the "standard" globular cluster. Larsen & Brodie (2000) and Brodie & Larsen (2002) reported what they called "faint fuzzies" as satellites of the lenticular galaxy NGC 1023. These "faint fuzzies" are extended star clusters with radii between 7 and 15 parsecs with luminosities as faint as $M_V \sim 6.2$ mag. Faint and extended star clusters have also been discovered as satellites of the Andromeda galaxy (Huxor et al. 2005; Mackey et al. 2006). Da Costa et al. (2009) published the discovery of an extended star cluster with an effective radius of 22 parsecs in the Sculptor Group Dwarf Elliptical Galaxy Sc-dE1.

The least luminous galaxy was reported to be Segue 1 (Geha et al. 2009). This object is

an Ultra-Faint Dwarf spheroidal galaxy (M_V=-1.5 mag) with an effective radius of 29 pc. These stellar systems are Milky Way satellites dominated by dark matter and are claimed to assuage the missing galaxy problem (e.g. Geha et al. 2009). Observationally, these systems are generally detected and studied with only a few tens or a few hundreds of stars (Muñoz et al. 2012).

Extended and faint stellar clusters are difficult to detect observationally and the discoveries cited above, most of them outside the Milky Way, rely on the sensitivity and resolution of the Hubble Space Telescope. Given the observational challenge to detect extended star clusters, numerical simulations have become a natural option to study the properties of these faint stellar systems (Hurley & Mackey 2010).

1.6 Numerical Simulations: From N to N

Direct experimentation often carried out in chemistry or other branches of the physical sciences is impossible in astrophysics. The essay tube used in chemistry has been replaced by the computer in astrophysics. Our current understanding of star cluster evolution and galaxy formation, among other concepts, is established through simulations. Phenomena modelled decades ago remain valid today: from the early work of von Hoerner (1957) in star clusters to the elegant and well presented simulations of Toomre & Toomre (1972) in galaxy interactions.

Using the new computational capacity given to us by the introduction of Graphic Processing Units (GPUs) in astrophysical calculations we test the main physical mechanisms that are believed to determine the size and mass of compact stellar systems. The new found computer power that is available today allows us to perform advanced N-body models to study the impact of galactic tides as well as the effects of disk shocking on star clusters. GPU-based simulations of stellar systems of $\sim$100 000 stars can be carried out in a few weeks, a feat impossible to achieve a few years ago. These simulations allow us to obtain the entire picture of the evolution of star clusters over a Hubble time. The N-body models enable us to test different parameters that we deem relevant to explain the origin of the observed sizes and masses of compact stellar systems.

The direct N-body models used in this thesis are just one approach to model the evolution of star clusters. Heggie & Hut (2002) give clear taxonomy of the different approaches to study star cluster evolution with the main families being: scaling models, fluid models, Fokker Planck models, and N-body models. Perhaps the main competitor to the direct summation N-body models presented here is the Monte Carlo approach. In Monte Carlo

simulations of star clusters the Fokker-Planck equation is solved in an statistical way. The Fokker-Planck equation is an approximation of the Boltzmann equation that describes the distribution function of a stellar system (Binney & Tremaine 1987). Instead of calculating the equations of motion for all particles the Monte Carlo approach uses a finite number of particles to sample the distribution function of the ensemble of stars (Giersz 1998; Hypki & Giersz 2013). One of the advantages of Monte Carlo simulations is the large number of particles N that can be modelled. For example, Giersz & Heggie (2011) recently presented a full-scale Monte Carlo model of the massive globular cluster 47 Tucanae that improved our understanding of this well observed object.

In the simulations of star clusters presented here star clusters are considered collisional systems, that is, systems where two body interactions are important in determining the dynamical evolution of the entire system. This is in contrast, for instance, to elliptical galaxies that are generally considered collisionless systems.

1.7 This Thesis

In Chapter 2 we use data taken under the Coma Cluster Treasury Survey to study the properties of Ultra-Compact Dwarfs and extended star clusters around NGC 4874. This dataset is particularly interesting since one single ACS image contains more than 5000 globular cluster candidates. The richness of this dataset allows us to better characterize the photometric properties of UCDs and their link with the two subpopulations of globular clusters.

Chapter 3 presents a search for UCDs and extended star clusters in the fossil group NGC 1132. This fossil group is at the same distance as the Coma Cluster, i.e. $D = 100$ Mpc. This search is also carried out using ACS data. The galactic environment of a fossil group is very different to the galaxy cluster studied in Chapter 2. This work will allow us to determine how common UCDs are and assert the fact that their existence is independent from host galaxy type.

Chapter 4 is dedicated to the spectroscopic follow-up of the UCD candidates discovered in Chapter 3. We have obtained Gemini Multi-Object Spectrograph multislit data of the brightest UCD candidates in the fossil group NGC 1132. The spectroscopic work is an important validation of the photometric method used in the previous two chapters. With the new Gemini data we also confirm the discovery of a M32 counterpart in the fossil group NGC 1132.

In Chapter 5 advanced N-body simulations of star clusters are presented. These nu-

merical simulations are aimed at understanding the physical mechanisms that determine the size scale of compact stellar systems. These numerical simulations follow the evolution of star clusters through a Hubble time and are designed to better understand the role of galactic tides on the size of star clusters.

Chapter 6 contains detailed N-body simulations of star clusters undergoing disk shocking. These N-body models evaluate the impact of disk shocking on the mass loss and survival rates of star clusters. Different disk geometries and different disk masses are evaluated.

Chapter 7 summarizes the main findings of this thesis and presents future avenues of research in the field.

2

Ultra-Compact Dwarfs and Extended Star Clusters in the Coma Cluster

We analyze high resolution Advanced Camera for Surveys (ACS) data of the core of the Coma cluster, the richest galaxy cluster in the nearby Universe (Colless 2001). The Coma cluster provides the unique opportunity to study a very large number of distinct galaxies within a small area of the sky, as shown in Figure 2.1. Coma contains a diverse sample of stellar systems ranging from globular clusters to giant elliptical galaxies. The core of this cluster contains two giant elliptical galaxies (NGC 4874 and NGC 4889) with globular cluster systems that, when combined, have more than 30000 members (Blakeslee & Tonry 1995; Harris et al. 2009). We specifically study an ACS pointing containing NGC 4874, one of the two central galaxies of Coma, and the only central galaxy with ACS imaging. The globular cluster system of NGC 4874 alone has an estimated *minimum* of 18700 members (Harris et al. 2009), the largest published globular cluster system.

We derive a color-magnitude diagram for this immense GCS allowing us to clearly define its color distribution. We also estimate the structural parameters of sources that show extended structure using ISHAPE (Larsen 1999), especially designed software to derive the structural parameters of slightly resolved astronomical objects. We find that 52 objects have effective radii $\gtrsim$10 pc. These objects have colors, and magnitudes similar to the brightest globular clusters. We postulate that these objects constitute the UCD and Extended Star Cluster (ESC) population of the core of the Coma Cluster.

There is a vast terminology to define objects larger than GCs and smaller than dwarf elliptical galaxies: Intermediate Mass Object, Dwarf Galaxy Transition Object (DGTO), extended star clusters, etc. (see Hilker 2006 for a review).[1] UCDs, in particular, are

[1]We were not inmune to this overabundance of terms. The contents of this chapter were published using the acronym DGTO. We use Extended Star Cluster in subsequent publications.

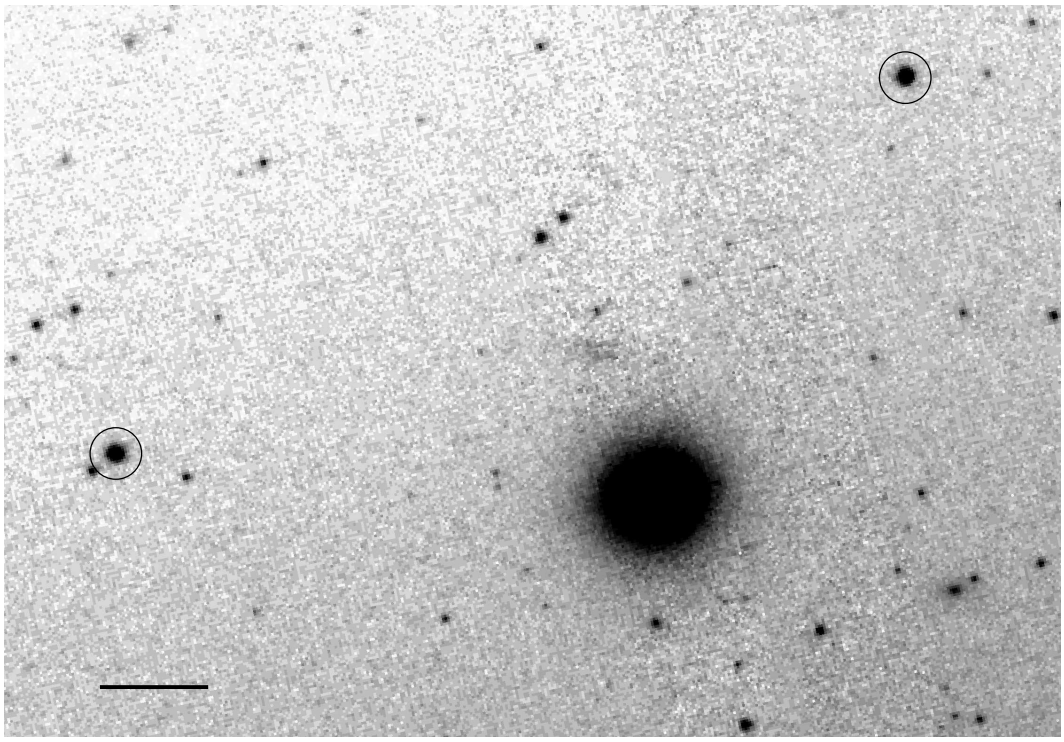

Figure 2.1 Section of the HST/ACS image illustrating the rich diversity of stellar systems in the core of the Coma cluster. The brightest galaxy is CcGV19a, classified as a compact elliptical by Price et al. (2009). Two UCD candidates are indicated with circles. Several members of the rich globular cluster system of NGC 4874 are also clearly visible. The center of this image is located at ∼24 kpc NE from NGC 4874 (not shown in this figure). The diffuse halo of this central dominant galaxy is apparent as a diagonal light gradient across the field of view from bottom right to top left. The bar on the lower left is 1 kpc in length. North is up and east is left.

conventionally defined as objects with radii of ∼10-100 pc, although departures from this size range have been reported (e.g. Evstigneeva et al. 2008). A commonly quoted lower limit for the mass of UCDs is 2×10^6 $M_\odot$ (Mieske et al. 2008) and their magnitude limit is typically $M_V \lesssim -11$ mag (Mieske et al. 2006). UCDs also have higher mass-to-light ratios (M/L ∼6 to 9) than globular clusters and the presence of dark matter in these stellar systems is still under debate (Hasegan et al. 2005; Dabringhausen et al. 2008). In this chapter we will refer to the ensemble of 52 objects with an effective radius $\gtrsim$ 10 pc as UCD/ESCs. The term UCDs will be reserved for the subset of 25 objects which are additionally brighter than the luminosity requirement for the UCD label. We should note at this point that the magnitude, mass, and size limits that distinguish the low mass stellar systems discussed above are somewhat arbitrary and currently used as working definitions.

Independent methods give estimates of the distance to the Coma cluster between 84 and 108 Mpc, see Table 1 of Carter et al. (2008). We adopt a fiducial distance of 100 Mpc and thus a scale of 23 pc per 0.05 arseconds (one ACS pixel). This is an accurate distance to Coma that was adopted by the HST Coma Cluster Survey.

2.1 Data

We use data taken during the Coma Cluster Survey (Carter et al. 2008). This HST Treasury program was able to obtain eighteen pointings of the core of the Coma Cluster with the ACS Wide Field Channel detector before the electronics failure of the instrument. Each field comprises imaging in two different filters: F475W (similar to Sloan g) and F814W (Cousins I; Mack et al. 2003).

The science data from this observing program were prepared through a dedicated pipeline that is described in detail by Carter et al. (2008). The final images were created using the PYRAF task MULTIDRIZZLE (Koekemoer et al. 2002). We use the public data products from the second release of the Coma Cluster Treasury program which provide the best relative alignment between the two filters. In the nomenclature of the second data release, we use field number 19 with target name Coma 3-5. The exposure times for this field are 2677 s and 1400 s for the F475W and F814W filters, respectively.

2.2 PSF

We build the PSF using the DAOPHOT package within PYRAF. We perform photometry of candidate stars using the task PHOT, the selection of optimal stars is carried out using PSTSELECT which selects 12 bright, uncrowded, and unsaturated stars across the field. The

computation of a luminosity weighted PSF is done with the task PSF. ISHAPE requires the PSF to be oversampled by a factor of ten, that is the pixel size should be a tenth of the native pixel size of the science image. We create an oversampled PSF with the task SEEPSF, and we provide the resulting PSF as input to ISHAPE. While several options to calculate the PSF for the HST exist, it has been shown that with the sequence of DAOPHOT tasks described above a reliable and accurate model of the PSF core can be constructed (Spitler et al. 2006; Price at al. 2009).

2.3 Detection

We median filter the images in both bands with a box size of 41×41 pixels and then subtract the result from the original images to obtain a residual free of galaxy light. We thus facilitate the detection of the position of point-like sources. A first catalogue of sources is generated running SExtractor (Bertin & Arnouts 1996) on the image created by adding the median-subtracted images of the two filters. Within SExtractor we use a detection threshold of five pixels with a 3σ level above the background in order to trigger an extraction. A lower detection limit would generate a large number of spurious detections while more conservative parameters would leave globular clusters undetected.

We perform a first round of careful visual inspection of all detections and eliminate spurious sources such as background galaxies and objects along the edge of the chip. We use a novel method to carry out a secondary visual inspection of our 4976 remaining detections. We take advantage of the short computation time needed to derive an initial set of structural parameters with ISHAPE. In order to discard spurious sources from our analysis we follow the steps described below. With the initial set of structural parameters obtained with ISHAPE we create a list of objects with dubious values such as very large ellipticity or conspicuously large effective radii ($r_h \gtrsim 100$ pc) for visual inspection. By virtue of the high-resolution imaging of the ACS we can determine that most of these objects are background galaxies, irregular structures, or gradients of surface brightness without link to any real source. Examples of objects flagged and eliminated due to their suspicious structural parameters (i.e. large ellipticity or large effective radius) are presented in Figure 2.2. Using this method we are able to eliminate 170 false detections in a short time. We are left with 4806 sources, most of them globular clusters belonging to the NGC 4874 GCS.

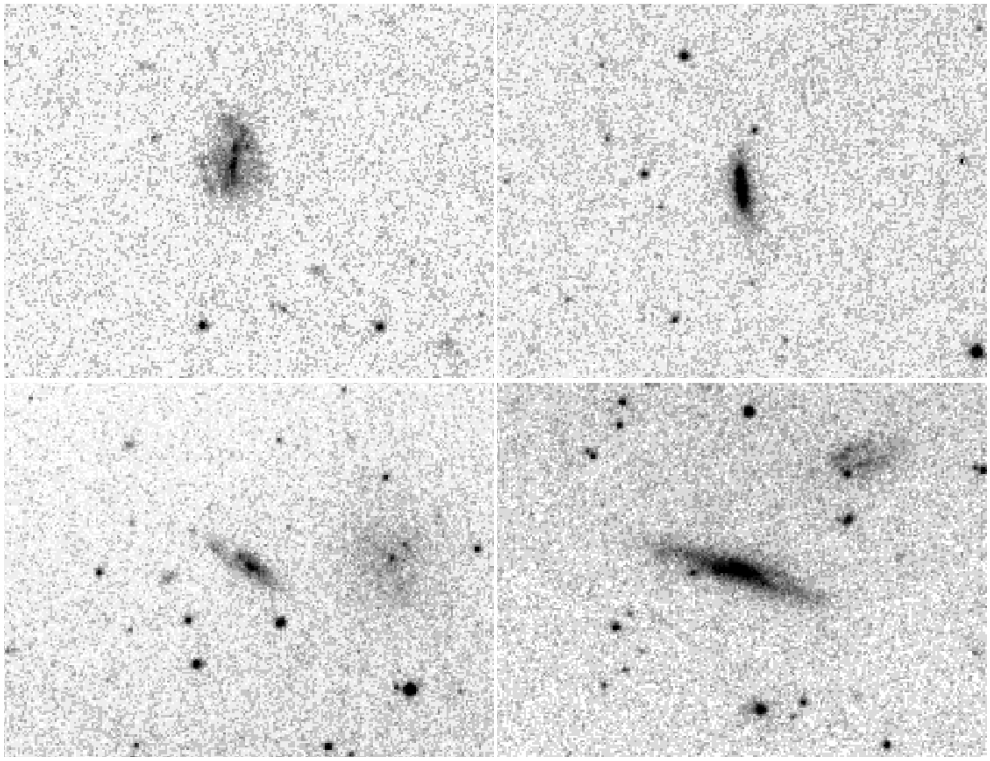

Figure 2.2 Four examples of spurious detections eliminated based on their suspicious structural parameters. These sources are background galaxies in all likelihood and have effective radii that would correspond to hundreds of parsecs if they were at the distance of Coma.

2.4 Structural Parameters

2.4.1 Effective Radius

As we mentioned in Chapter 1, the high resolution of the Hubble Space Telescope has enabled the measurement of structural parameters of vast numbers of extragalactic globular clusters. Using WFPC2 data, Larsen et al. (2001) derived size estimates of globular clusters in seventeen nearby, early-type galaxies and found that the majority of these clusters have effective radii of two to three parsecs. Based on ACS data, and an independent technique, Jordán et al. (2005) derived the effective radii of thousands of globular clusters within 100 early-type galaxies in the Virgo cluster and report a median GC effective radius of 2.7 ± 0.35 pc. Masters et al. (2010), studying the globular clusters around 43 early-type galaxies in the Fornax cluster found that the median r_h of a GC is 2.9 ± 0.3 pc. These results are in remarkable agreement with size measurements of GCs in spirals (Spitler et al. 2006; Harris et al. 2010) and with the known median effective radii of Galactic globular clusters, i.e. $< r_h >= 3.2$ pc (Harris et al. 1996). At present, no correlation has been found between the luminosity (or mass) of globular clusters and their effective radius (McLaughlin 2000), however their median r_h is $\sim$ 3pc.

We fit the light profiles of 4806 sources using ISHAPE (Larsen 1999), a software commonly used to derive the structural parameters of barely resolved astronomical objects, such as extragalactic globular clusters. ISHAPE convolves the point-spread function with an analytical model of the surface brightness profile and searches for the best fit to the data by varying the full width half maximum (FWHM) of the synthetic profile. The output given by ISHAPE for each source comprises the effective radius (or equivalently half-light radius), the ratio of the minor over major axis, the position angle, the signal-to-noise level S/N, and the reduced χ^2 (or goodness of fit).

Within ISHAPE the user can choose from several analytical models for the light profile that will be used during the fitting process, e.g. King, Sérsic, Gaussian. We adopt a King profile with a concentration parameter of $c = 30$: the concentration parameter c is defined as the ratio of the tidal radius over the core radius $c = r_t/r_c$ (King 1962, 1966).

The value of $c = 30$ accurately represents the average concentration parameter for Milky Way, M31, and NGC 5128 globular clusters (Harris et al. 1996; Harris 2009a and references therein). Moreover, the concentration parameters for UCDs in Fornax and Virgo derived by Evstigneeva et al. (2008) are consistent with a choice of $c = 30$. In addition, by using $c = 30$ we facilitate comparison with similar studies, e.g. Blakeslee & Barber DeGraaff (2008). Also, quantitative tests show that for partially resolved objects

the solution for r_h is very insensitive to the particular choice of c (Harris et al. 2010).

A signal-to-noise ratio of $S/N > 50$ is necessary to obtain reliable measurements of the structural parameters with ISHAPE. As mentioned above, the S/N is calculated by ISHAPE and is part of its output for each object. This requirement for the S/N was demonstrated through extensive testing of ISHAPE by Harris (2009a). Of our initial 4806 sources for which we derived structural parameters, 631 sources conform to this S/N requirement simultaneously in both bands. Hereafter, when considering structural parameters we will refer only to those 631 objects with S/N>50 in both bands.

At the distance of the Coma cluster, namely 100 Mpc, the effective radius of a globular cluster ($\sim$3 pc) is equivalent to six milliarcseconds, a radius practically irrecoverable in ACS/WFC data with a pixel size of 0.05 arcseconds. Using WFPC2 data, Harris et al. (2009a) demonstrated that at the distance of Coma objects with $r_h < 6$ pc have light profiles indistinguishable from those of stars. As expected, the vast majority of clusters for which we attempted to obtain reliable structural parameters remain unresolved and thus an estimate of their effective radius cannot be made, see Figure 2.3. However, with ISHAPE we find 52 sources that are positively resolved.

We derive the structural parameters of all sources independently in both bands. We minimize systematics between the two measurements by strictly following the same set of steps. We also use the same set of stars to create both PSFs. In Figure 2.3 we present the ratio r_{hF475W}/r_{hF814W} plotted against r_{hF814W}. This figure shows how the ratio converges to $\sim$1 at $r_{hF814W} > 9$ pc. At larger radii (> 10 pc) the agreement between the two measurements is excellent and reveals a small but real offset. This small but significant difference (12%) in the value of r_h in these two bands can be expected owing to physical reasons, notably color gradients within globular clusters, as shown by Larsen et al. (2008). These authors find that r_h can vary by up to 60% between the measurements in blue (F333W) and red (F814W) bands. For our measurements of UCD/ESCs the median of the ratio r_{hF475W}/r_{hF814W} is $0.88^{+0.03}_{-0.02}$.

We select as UCD/ESC candidates only those objects that are resolved in *both* bands. The vertical line in Figure 2.3 shows that all objects with $r_{hF814W} \geqslant 9.2$ pc are consistently resolved in both bands. Most of the UCD/ESC candidates (45 of them) have an effective radius larger than 10 pc in at least one band, the minimum size commonly quoted for UCDs (Mieske et al. 2004). We include in our list of candidates seven objects slightly below this, somewhat arbitrary, cut: these seven objects have an $r_h \geqslant 9.5$ in one band and are within the errors ($\pm$0.006 arcseconds or $\pm$2.8 pc, Harris 2009a) in agreement with the standard size definition of UCDs. Objects resolved in one band but having zero size

in the other are rejected as UCD/ESC candidates, see Figure 2.3.

We also explore the impact of the fitting radius in pixels (FITRAD) that we use as an input of ISHAPE. The UCD candidates are barely resolved in the ACS images, that is, they have a FWHM of ~ 3 pixels. ISHAPE is limited to a fit radius of a few pixels (Blakeslee & Barber DeGraaff 2008) and the optimal fitting radius is the result of a balance between signal and noise, similar to the evolution of the S/N ratio as a function of aperture radius in photometric measurements. The selection of candidates is carried out using a FITRAD=6 pixels. The consistency of the measurements with FITRAD=6 pixels is shown in Figure 2.3 where we compare the values of r_h in both bands.

ISHAPE yields robust values of effective radius independent of the model selected by the user, i.e. the value of r_h measured with a King profile is expected to be similar to r_h obtained using a Sérsic profile. We exploit this property of ISHAPE in Figure 2.4. The aim of Figure 2.4 is twofold: we show the impact on the value of r_h measured by ISHAPE of i) two different analytical models, and ii) two different fitting radii. The values of r_h returned by ISHAPE should be equivalent for different (but reasonable) analytical models of the surface brightness profile. In fact, a King profile (King 1962, 1966) with a concentration parameter of c=30, and a Sérsic model (Sérsic 1968) with a Sérsic index of $n = 2$ are equivalent for our measurements. This is particularly true for the smaller UCD candidates as noted by Evstigneeva et al. (2008). A larger fitting radius, FITRAD=15 pixels instead of FITRAD=6 pixels, gives generally a larger r_h. Given that a larger fitting radius is more appropriate for bigger sources, we report in Table 2.1 the values obtained using FITRAD=15 pixels for those sources with $r_h > 25$ pc in the initial run with FITRAD=6 pixels.

Globular clusters have a median r_h of $\sim$3 pc but their size distribution extends up to eight parsecs (Harris 2009a, Masters et al. 2010). UCDs studied by Evstigneeva et al. (2008) range in r_h between 4.0 and 93.2 pc while Blakeslee & Barber DeGraaff (2008) report UCDs with r_h ranging from 11.2 to 90.3 pc with a tentative gap between large globular clusters (or the most compact UCDs) with $r_h < 20$ pc and large UCDs with $r_h > 40$ pc. We find objects with r_h almost continuously spanning the range from 10 to 40 pc: we find no indication for a break in the size distribution of these compact stellar systems.

Metal-poor globular clusters are on average $\sim 25\%$ larger than metal-rich ones. This size difference has been well documented by several studies (Jordán et al. 2005; Spitler et al. 2006, Harris 2009a; Masters et al. 2010). This size difference has been explained as the result of mass segregation combined with the metallicity dependence of main sequence

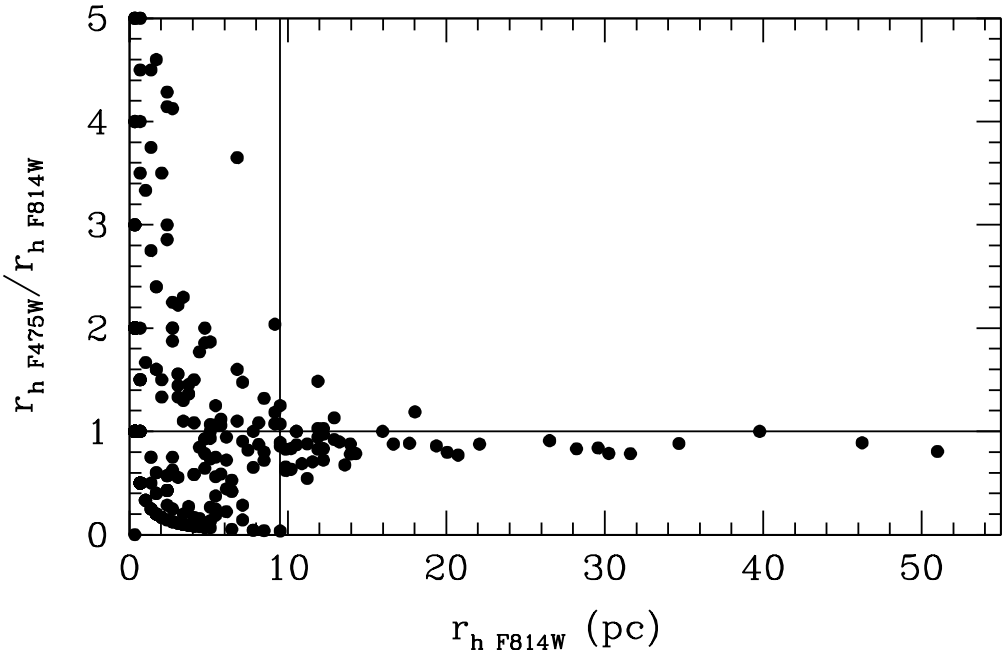

Figure 2.3 Ratio of r_h in the two bands vs. r_h in the F814W filter for all systems with S/N>50 (FITRAD=6 PIXELS). This plot reveals how standard globular clusters cannot be resolved at the Coma distance. On the other hand, all objects with $r_{hF814W} \geqslant 9.2$ pc are consistently resolved in both bands as marked by the vertical line. Measurement for objects larger than 10 pc are reasonably consistent between the two bands. This plot provides an estimate of the measurement errors, assuming that there is no physical reason for a size difference between the two bands.

stars (Jordán 2004). Harris (2009a) postulates that the conditions of formation can also be responsible for this size difference while Larsen & Brodie (2003) argue that a size-galactocentric distance trend and projection effects are the decisive factors. The recent work of Sippel et al. (2012) shows that primordial metallicity differences can account for the observed size difference of the two subpopulations of globular clusters. The correlation between size and color (or metallicity) observed for globular clusters is blurred at higher masses. In our sample blue UCD/ESC candidates have a median effective radius of $12.2^{+1.7}_{-0.5}$ pc while the median r_h for red UCD/ESC candidates is $11.9^{+4.2}_{-0.6}$ pc, there is thus no indication of any significant difference in median effective radius between these two groups.

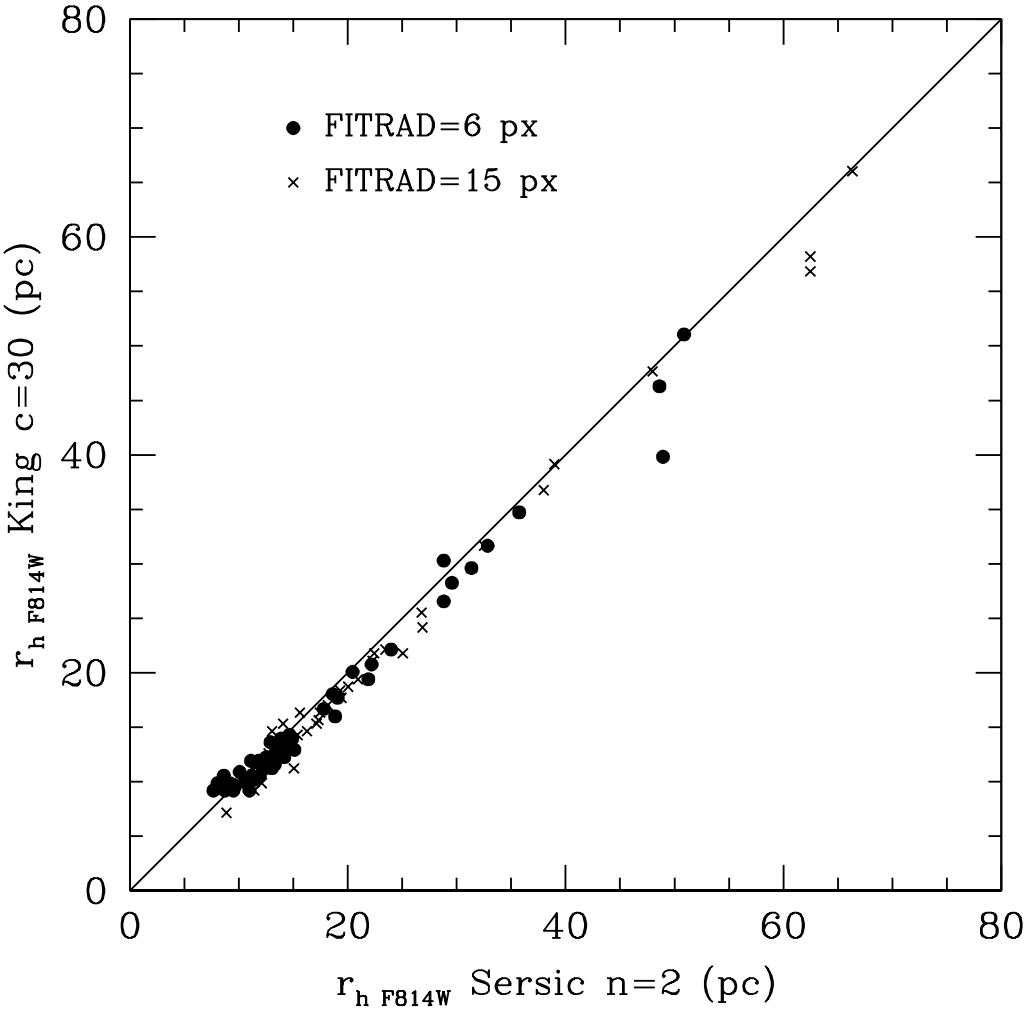

Figure 2.4 Effective radii measured by ISHAPE using different analytical models and different fitting radii (FITRAD, in pixels). The effective radius derived by ISHAPE using different analytical models shows excellent agreement. For the largest UCD candidates a larger fitting radius yields a larger effective radius. The errors of these measurements are: ±0.006 arcseconds or ±2.8 pc, (Harris 2009a).

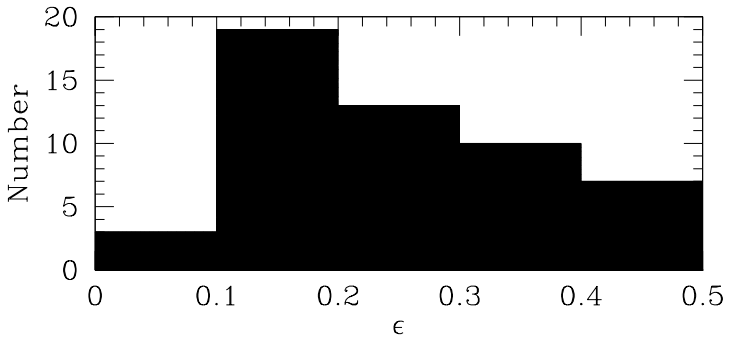

Figure 2.5 Ellipticity distribution for UCD/ESC candidates. A peak in the distribution is evident at ~ 0.15, and we find only three nearly spherical objects with $\epsilon < 0.1$.

2.4.2 Ellipticity

ISHAPE computes the minor/major (b/a) axis ratio for each object. We use this ratio to derive the ellipticity ($\epsilon = 1 - b/a$) and to set a selection limit of $0 \leq \epsilon < 0.5$ for our UCD/ESC candidates. This selection limit is commonly used in UCD studies (e.g. Blakeslee & Barber DeGraaff 2008) as a safeguard against background spirals masquerading as UCDs.

Figure 2.5 shows the ellipticity values of our UCD/ESC candidates which span the whole range set by our selection criterion. The smallest ellipticity of this sample is 0.03, only three candidates have an ellipticity of less than 0.1. Blakeslee & Barber DeGraaff (2008) found that all their UCD candidates have an ellipticity between 0.16 and 0.46. The largest ellipticity in our sample of UCD candidates is 0.49 and the median of the distribution is 0.24.

The complete list of UCD/ESC candidates with their effective radius and ellipticity is presented in Table 2.1. Given that ISHAPE measures the effective radius along the major axis, we apply a correction to obtain the circularized effective radius that we present in Table 2.1:

$$r_{h,circularized} = r_{h,ishape}\sqrt{(1-\epsilon)}$$

2.5 Photometry

We perform photometric measurements with the task PHOT of the PYRAF/DAOPHOT package. We execute aperture photometry with a four pixel radius and apply an aperture

correction following the formulas of Sirianni et al. (2005). We use the ACS/WFC Vega zero points for each filter that we obtain from the updated tables maintained by the Space Telescope Science Institute, i.e. $m_{F475W} = 26.163$ mag, and $m_{F814W} = 25.520$ mag (Sirianni et al. 2006). Note that the main catalogue of sources for the Coma Treasury Survey uses AB magnitudes (Hammer et al. 2010). Foreground Galactic extinction is calculated using E(B-V)=0.009 mag (from NED) and the extinction ratios of Sirianni et al. (2005), from which we obtain $A_{F475W} = 0.032$ mag and $A_{F814W} = 0.016$ mag.

We obtain photometric measurements of 4806 sources in F475W and F814W. Most of these sources are globular clusters likely belonging to the NGC 4874 GCS. As shown in Figure 2.1, crowding is not an issue in our data.

2.5.1 Color-Magnitude Diagram

In the color-magnitude diagram of Figure 2.6 we also plot the size information derived with ISHAPE. Unresolved globular clusters belonging to the NGC 4874 GCS are plotted as black dots. Some of these globular clusters might also be intracluster globular clusters of Coma similar to those found in the Virgo cluster (Williams et al. 2007; Lee et al. 2010). UCD/ESC candidates are plotted as filled red circles. Our UCD/ESC candidates coincide in color with the brightest members of the metal-poor and metal-rich subpopulations of globular clusters.

The color distribution of the brightest GCs is clearly defined in the CMD. Background galaxies removed while cleaning spurious detections have different colors than globular clusters. This was demonstrated by Dirsch et al. (2003; their Figure 3) studying a field containing the NGC 1399 GCS and a background field; see also Harris (2009b) for his study of contamination in the M87 field. Moreover, evolutionary synthesis models predict that elliptical galaxies of any age, which are the background objects most likely to appear as UCDs, have colors $(B - I) > 1.9$ (Buzzoni 2005).

Mieske et al. (2004) set a magnitude limit of $M_V < -11.5$ mag for their UCD selection criteria while Hasegan et al. (2005) adopt $M_V < -10.8$ mag. Mieske et al. (2006) identified a metallicity break and thus set the onset of the size-luminosity relation at $M_V < -11$ mag. Assuming $V-I = 1.1$ mag and a distance modulus to the Coma Cluster of $(m-M) = 35.0$ mag we find that UCDs should have $m_I < 22.9$ mag if we set a selection limit of $M_V < -11$ mag. We have assumed $I \approx F814W$ (Sirianni et al. 2005).

There are 110 objects in total with $m_{F814W} < 22.9$ mag in the color-magnitude diagram of Figure 2.6, i.e. above the horizontal bar, and 25 of these objects also have effective radii characteristic of UCDs. These 110 objects are of similar or higher mass than ω Centauri

($2.5 \times 10^6 M_\odot$, van de Ven et al. 2006). Higher resolution data should reveal that the remaining 85 objects have an extended structure given that $\sim 2 \times 10^6 M_\odot$ marks the onset of a size-luminosity relation for stellar structures (Hasegan et al. 2005; Forbes et al. 2008; Murray 2009). We also present the color histogram in the bottom panel of Figure 2.6, which is consistent with the histogram presented by Harris et al. (2009).

Table 2.1: **Position, magnitude, color, effective radius, ellipticity, and FITRAD of UCD/ESC Candidates.**
Columns 1 & 2: x and y position in pixels of the ACS Camera; Columns 3 & 4: RA and Dec (J2000); Column 5: magnitude in the F814W band; Column 6: F475W-F814W color; Column 7: r_h in F475W in pc; Column 8: r_h in F814W in pc; Column 9: Ellipticity in F814W; Column 10: Circularized effective radius $r_h, circ$ (F814W) in pc; Column 11: FITRAD in pixels used for the given measurement.

X	Y	RA	Dec	m_{F814W}	Color	r_{hF475W}	r_{hF814W}	ϵ	$r_h, circ$	FITRAD
(1)	(2)	(3)	(4)	(5)	(6)	(7)	(8)	(9)	(10)	(11)
387	2015	12:59:39.22	27:59:54.7	19.76	1.74	41.9	47.7	0.28	40.5	15
2390	1217	12:59:40.60	27:58:08.4	21.14	1.70	34.0	36.8	0.22	28.7	15
1252	284	12:59:44.94	27:58:54.4	21.54	1.78	8.5	9.5	0.27	8.1	6
2894	1482	12:59:39.22	27:57:46.5	21.62	1.83	14.6	16.7	0.14	15.4	6
1979	2093	12:59:37.68	27:58:37.6	21.68	1.63	15.6	17.7	0.34	14.4	6
1836	1658	12:59:39.40	27:58:40.1	21.68	1.49	12.6	12.2	0.17	11.2	6
3130	1110	12:59:40.41	27:57:31.1	21.74	1.59	11.9	9.5	0.34	7.7	6
3481	819	12:59:41.21	27:57:10.9	21.77	1.60	11.2	11.9	0.20	10.6	6
2212	2273	12:59:36.83	27:58:28.1	21.81	1.72	10.5	10.5	0.24	9.2	6
1764	1338	12:59:40.64	27:58:40.3	21.90	1.63	8.8	12.2	0.15	11.3	6
1527	1046	12:59:41.91	27:58:48.9	22.06	1.51	6.1	11.2	0.03	11.1	6
2698	2380	12:59:36.06	27:58:05.4	22.07	1.70	16.0	20.1	0.18	18.2	6
2291	1943	12:59:37.99	27:58:20.8	22.10	1.42	24.1	26.5	0.32	21.9	6
2891	3754	12:59:30.83	27:58:10.2	22.26	1.45	6.5	9.9	0.27	8.4	6
2554	2612	12:59:35.31	27:58:14.9	22.33	1.66	54.1	66.0	0.04	64.7	15
2845	3357	12:59:32.33	27:58:08.4	22.40	1.84	9.9	11.2	0.11	10.6	6
2001	282	12:59:44.36	27:58:17.8	22.44	1.67	7.5	10.9	0.35	8.8	6
2031	1159	12:59:41.09	27:58:25.4	22.53	1.50	8.5	10.2	0.14	9.5	6
2625	2513	12:59:35.62	27:58:10.4	22.67	1.47	8.2	9.9	0.15	9.1	6
2235	1601	12:59:39.30	27:58:20.0	22.74	1.39	19.4	22.1	0.15	20.4	6
3785	2816	12:59:33.60	27:57:16.8	22.77	1.72	9.9	11.9	0.20	10.6	6
909	907	12:59:42.90	27:59:17.7	22.78	1.76	8.2	9.5	0.17	8.7	6
3863	1438	12:59:38.62	27:56:58.7	22.84	1.38	9.9	9.2	0.27	7.8	6
3539	1368	12:59:39.14	27:57:13.8	22.85	1.54	11.9	12.2	0.39	9.6	6
4121	3518	12:59:30.74	27:57:07.6	22.87	1.47	10.2	9.5	0.26	8.2	6
3124	1713	12:59:38.19	27:57:37.7	22.94	1.48	16.0	16.0	0.32	13.2	6
1440	2503	12:59:36.59	27:59:08.3	22.94	1.39	9.9	9.2	0.47	6.7	6
602	1346	12:59:41.52	27:59:37.2	23.00	1.44	26.6	31.7	0.14	29.4	15
746	2071	12:59:38.73	27:59:37.7	23.05	1.39	16.0	20.7	0.15	19.1	6
3507	1900	12:59:37.20	27:57:20.9	23.10	1.83	10.9	13.9	0.24	12.2	6
3359	1864	12:59:37.45	27:57:27.7	23.12	1.84	10.5	10.5	0.46	7.7	6
3311	2469	12:59:35.25	27:57:36.4	23.14	1.54	6.5	10.2	0.15	9.4	6

Table 2.1 – *Continued from previous page*

X	Y	RA	Dec	m_{F814W}	Color	r_{hF475W}	r_{hF814W}	ϵ	$r_h, circ$	FITRAD
1559	1350	12:59:40.76	27:58:50.5	23.14	1.54	8.2	11.6	0.43	8.7	6
1644	925	12:59:42.26	27:58:41.9	23.26	1.36	6.1	9.9	0.43	7.4	6
2368	3758	12:59:31.23	27:58:35.9	23.27	1.47	12.2	13.9	0.40	10.8	6
3025	3667	12:59:31.05	27:58:02.8	23.34	1.43	9.2	10.5	0.20	9.4	6
520	3837	12:59:32.38	28:00:07.1	23.46	1.74	55.1	56.9	0.21	50.6	15
3733	988	12:59:40.39	27:57:00.4	23.56	1.39	11.9	12.9	0.38	10.2	6
2480	2474	12:59:35.88	27:58:17.1	23.58	1.49	10.2	12.2	0.11	11.5	6
2110	2783	12:59:35.03	27:58:38.4	23.59	1.19	17.7	11.9	0.36	9.5	6
3116	1645	12:59:38.44	27:57:37.4	23.61	1.34	23.8	30.3	0.16	27.7	6
4144	4187	12:59:28.25	27:57:13.4	23.82	1.54	11.9	13.3	0.24	11.6	6
1926	1293	12:59:40.68	27:58:31.9	23.92	1.28	21.4	18.0	0.15	16.6	6
2049	1744	12:59:38.92	27:58:30.6	23.92	1.76	10.9	9.2	0.44	6.9	6
2665	1936	12:59:37.72	27:58:02.4	23.95	1.38	50.0	58.2	0.28	49.4	15
1986	1331	12:59:40.49	27:58:29.4	23.96	1.45	24.8	39.2	0.38	24.9	6
2841	1994	12:59:37.37	27:57:54.4	24.00	1.29	16.7	19.4	0.14	18.0	6
1772	2446	12:59:36.54	27:58:51.4	24.01	1.32	11.2	14.3	0.26	12.3	6
1948	1780	12:59:38.86	27:58:35.9	24.03	1.29	9.2	13.6	0.49	9.7	6
1243	1857	12:59:39.13	27:59:11.2	24.07	1.54	18.7	9.2	0.45	6.8	6
1452	1850	12:59:38.99	27:59:00.9	24.16	1.33	12.2	11.9	0.12	11.2	6
2131	1838	12:59:38.51	27:58:27.6	24.22	1.34	14.6	12.9	0.28	11.0	6

2.5.2 Size-Magnitude

We attempt to show the onset of the size luminosity relation in Figure 2.7. This figure is divided in four quadrants that are limited by the luminosity limit of UCDs and the ability of our data to obtain reliable size estimates, i.e. a size of $\sim$ 9.2 pc. Among the large scatter of the data points characteristic of such a plot (Masters et al. 2010; Forbes et al. 2008) we find that the fraction of unresolved stellar structures brighter than the minimum luminosity limit is particularly low around $m_{F814W} \sim 22$ mag, *a hint* of the onset of a size-luminosity dependence. More data points are needed to confirm this trend.

2.5.3 Color Bimodality

We use the software R for our statistical calculations presented in this work. R is a freely available, open source environment for statistical computing. The code RMIX, run within R, is specially designed to evaluate the mixture of multiple distributions within a histogram. RMIX is particularly well suited for the analysis of the underlying distributions present in the color-magnitude diagram. The code and its application to the analysis of a CMD has been presented, for example, by Wehner et al. (2008) and Harris (2009a).

The CMD of globular cluster systems is expected to be bimodal and, as noted earlier, for central dominant galaxies this bimodality should be evident. The bimodal UCD color distribution sits atop a bimodal globular cluster distribution well identified for GCs brighter than F814W < 24 mag, see both panels of Figure 2.8.

We use the best bimodal fit to the color distribution of the 52 UCD/ESC candidates to estimate the color boundary between blue and red UCD candidates (Figure 2.8). We define this point as the intersection of the two Gaussians fitting each subpopulation (Peng et al. 2006). We thus set the boundary between blue and red UCD/ESC candidates at F475W-F814W = 1.61. According to this fit, 63% of our UCD/ESCs belong to the blue subpopulation, while 37% are red. For UCDs only (i.e. $M_V < -11$ mag), 44% of them are blue and 56% are red.

The brightest candidates are thus red. Self-enrichment models developed by Bailin & Harris (2009) predict a mass-metallicity relationship (MMR) for the most luminous globular clusters (with masses $> 10^6 M_\odot$). Due to self-enrichment blue massive globular clusters and UCDs are expected to migrate in color towards the red. The visible effect of this mass-metallicity relationship in the CMD is the truncation towards higher luminosities of the blue subpopulation of globular clusters and a red color for the brightest UCDs, as observed in Figure 2.8.

2.6 Spatial Distribution

In Figure 2.9 we plot the spatial distribution of globular clusters, UCD/ESC candidates and large galaxies in the ACS frame. At the Coma distance an ACS/WFC field of view covers an area of ~ 100 kpc^2. A clear over-density of globular clusters appears to be associated with NGC 4874 and to a lesser extent with NGC 4873. No over-density is visible around NGC 4871. In this image, NGC 4874 is off-center, towards the edge of the field of view. The adjacent ACS field was part of the original Coma Cluster Treasury Survey observing program but was not acquired due to the failure of the instrument. A definitive conclusion on the spatial distribution of UCD/ESC candidates is difficult to reach without the missing adjacent field. With the available data we observe that UCD/ESC candidates appear to congregate around NGC 4874 and more importantly their spatial distribution is not random. The non-uniformity of the spatial distribution of UCD/ESC candidates and their colors argue against background sources masquerading as UCD/ESCs.

The cumulative fraction of globular clusters and UCD/ESC candidates as a function of radial distance to NGC 4874 is plotted in Figure 2.10. Both stellar systems follow

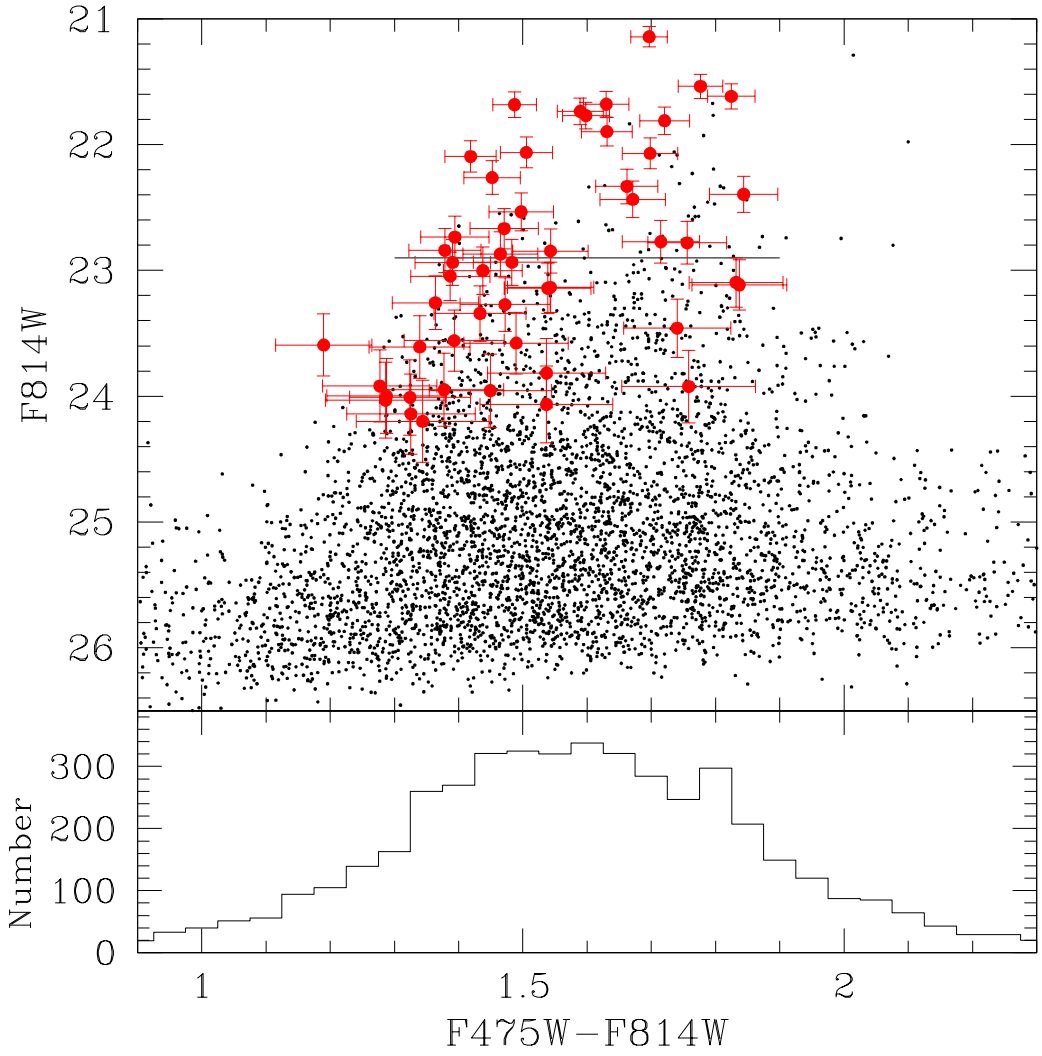

Figure 2.6 Top panel: Color-Magnitude Diagram of the globular cluster system and UCD candidates around NGC 4874. Unresolved globular clusters are plotted as black dots while resolved UCDs are shown as red circles. The horizontal bar marks $M_V = -11$ mag. Bottom panel: Color histogram for all globular clusters. The standard bimodality is blurred owing to photometric uncertainties at faint magnitudes.

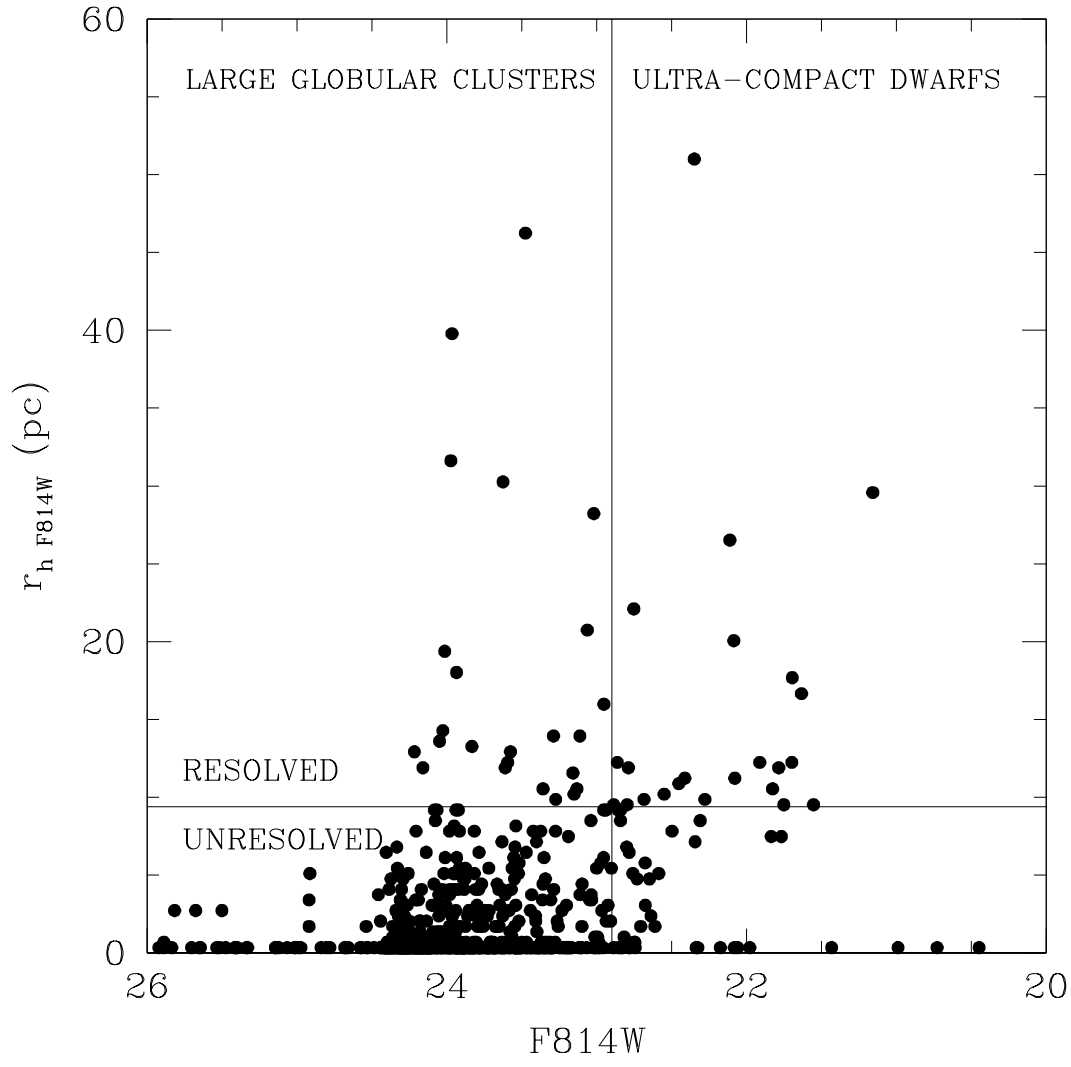

Figure 2.7 Magnitude versus effective radius for all objects with S/N > 50. This diagram is divided in four quadrants delimited by the minimum luminosity for UCDs and the ability of our data to resolve the compact stellar objects we study.

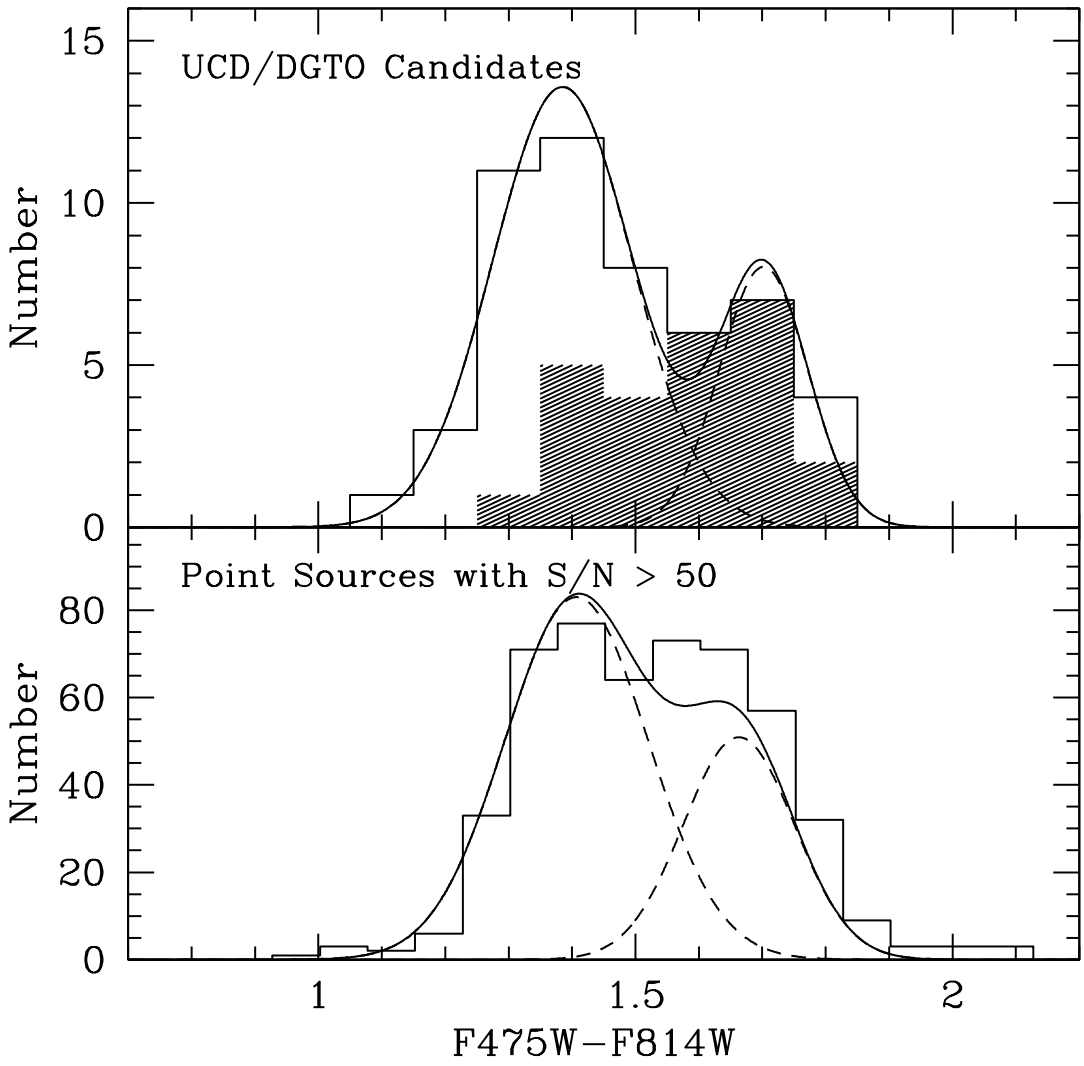

Figure 2.8 Top panel: Color distribution of 52 UCD/ESC candidates (DGTO≡ESC). We also over-plot the best bimodal fit to the distribution. Each Gaussian pair describes the red and blue subpopulation. The mean color for the blue subpopulation is 1.39 mag with a dispersion of $\sigma = 0.11$ mag while the mean color for the red subpopulation is 1.70 mag with $\sigma = 0.07$ mag. The shaded histogram corresponds to 25 UCD candidates, i.e. $M_V \lesssim -11$ mag. Bottom panel: color histogram for all 631 sources for which we attempt to derive structural parameters, i.e. objects with S/N > 50 – most of which are point sources.

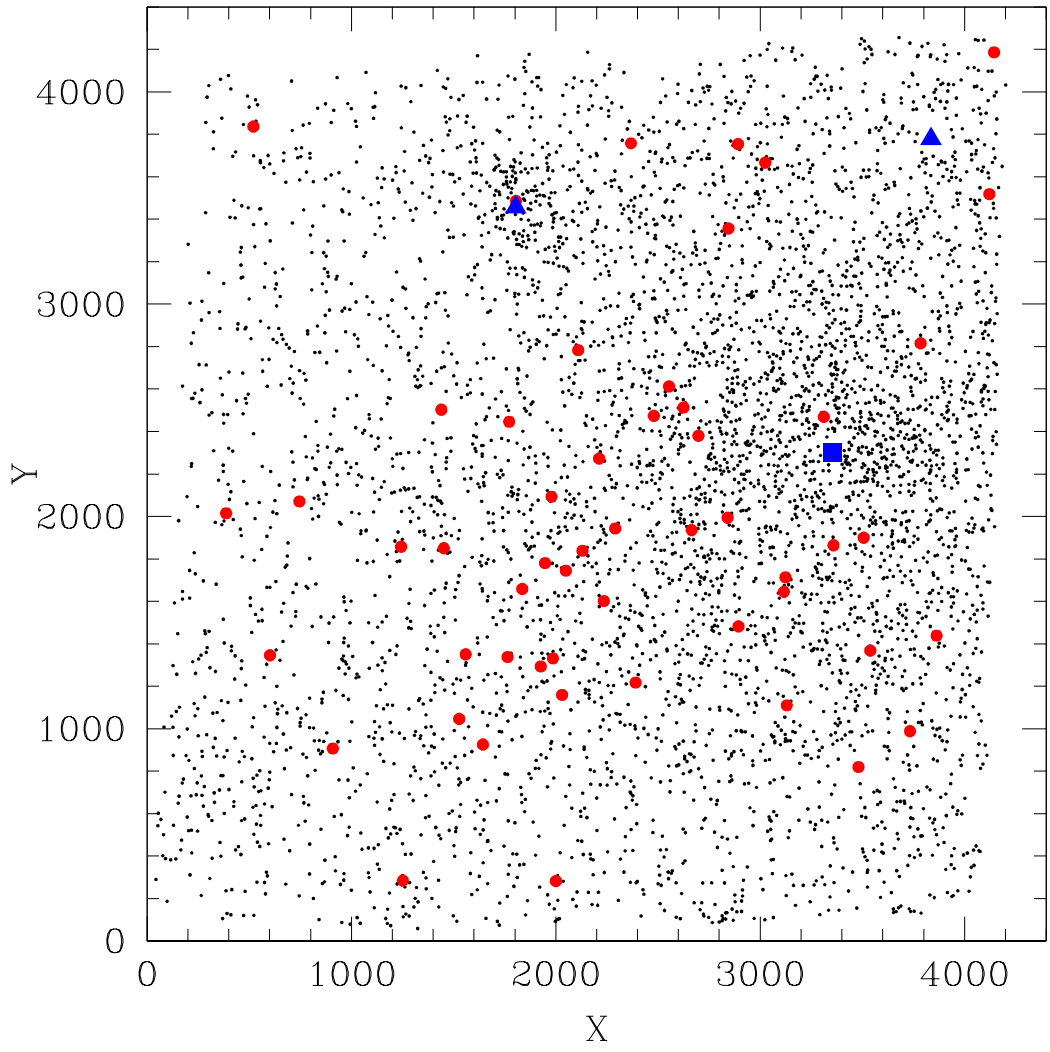

Figure 2.9 Spatial distribution of globular clusters (black dots) and UCD/ESC candidates (red circles) around NGC 4874 (solid square). An overdensity of globular clusters is clearly visible surrounding NGC 4874. A second overdensity is associated with NGC 4873 (solid triangle, top middle). NGC 4871 (solid triangle, top right) appears to lack a corresponding globular cluster system. UCD/ESC candidates appear to be concentrated in the vicinity of NGC 4874, imaging of the adjacent areas is certainly needed to draw a more definitive conclusion. The units are pixels of the ACS/WFC camera.

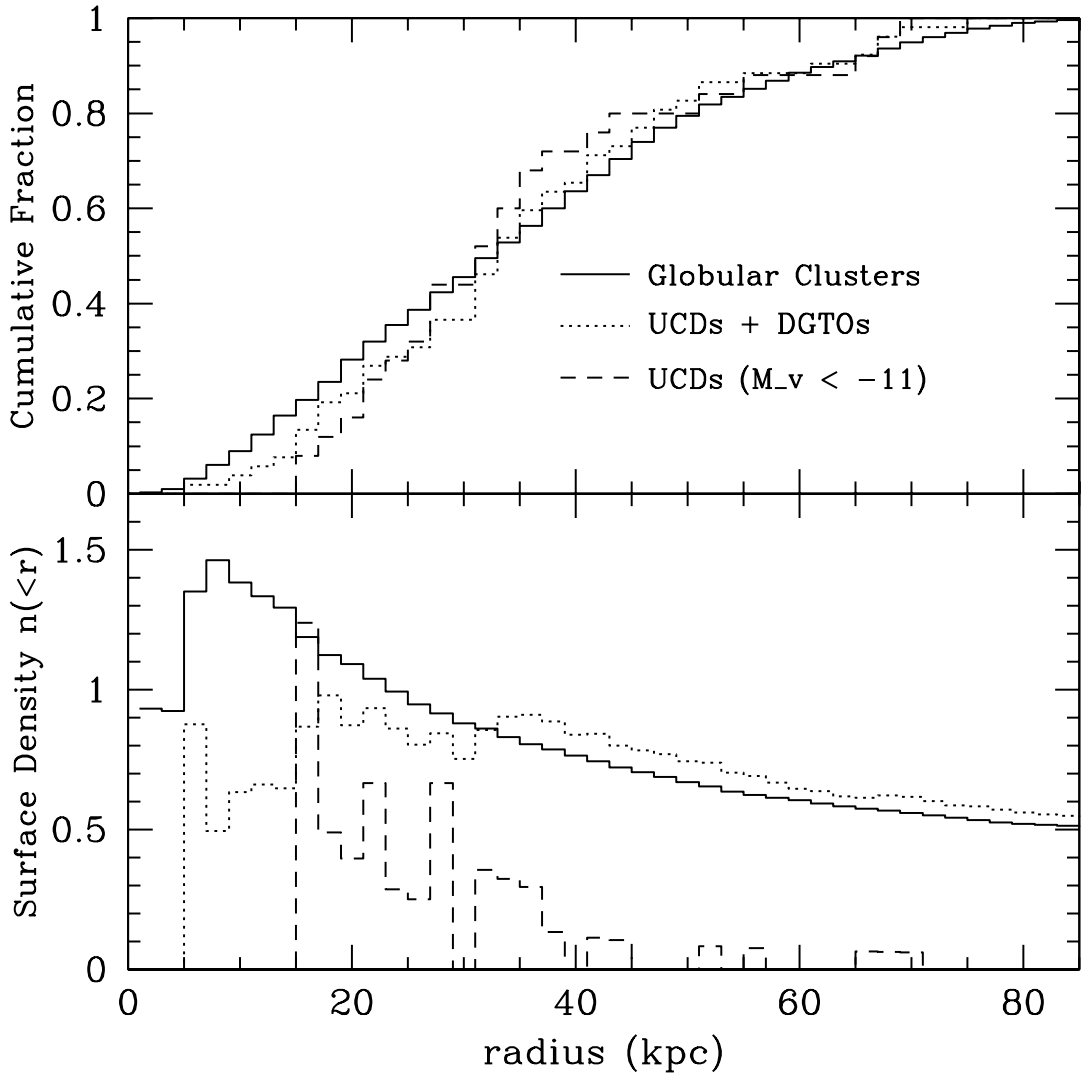

Figure 2.10 Top panel: Cumulative fraction of globular clusters, UCD/ESCs, and UCD candidates as a function of radial distance to NGC 4874. K-S tests on these distributions show that the maximum difference in cumulative fraction between GCs and UCD/ESCs is $D = 0.14$ with $P = 0.678$. Between GCs and UCDs these values are $D = 0.15$ and $P = 0.724$. Bottom panel: mean surface density of GCs, UCD/ ESCs and UCDs. The surface density of UCD/ESC and UCDs have been scaled by an arbitrary factor of 100 and 500 respectively. The surface density of UCDs is noisy due to the low numbers of these objects.

the same distribution. In fact a formal two sample Kolmogorov-Smirnov test yields a maximum difference between the two, azimuthally averaged, cumulative distributions of $D = 0.14$ with a corresponding $P = 0.678$. This result is valid if we compare UCDs and GCs, the maximum difference in their cumulative fractions is $D = 0.15$ with $P = 0.724$, see Figure 2.10. In Figure 2.10 we also plot the surface density of compact stellar systems in the vicinity of NGC 4874. There is a deficit of UCD/ESCs in the inner 15 kpc around NGC4874. This deficit of ESCs and UCDs can be explained, at least in part, by tidal interactions with the host galaxy. At small galactocentric distances tidal interactions with the host galaxy destroy or truncate the size of large stellar systems (Hodge 1960, 1962). Similar relations have been found for several extragalactic GCS but using projected galactocentric distances (e.g. Jordán et al. 2005). Tidal effects on compact stellar systems are carefully studied in Chapter 5 of this thesis.

2.7 Final Remarks

We do not observe any stark discontinuity between the characteristics of globular clusters, Extended Star Clusters and Ultra-Compact Dwarfs in the core of the Coma Cluster. On the contrary, bright globular clusters, ESCs, and UCDs have similar luminosity, color, and effective radius. This is suggestive of a continuous distribution of stellar systems gradually increasing in size and luminosity (mass) from globular clusters to UCDs.

2.8 Spectroscopic Follow-up

A spectroscopic survey of UCDs in the core of the Coma cluster was carried out by Chiboucas et al. (2011). This survey used the Keck telescope Low Resolution Imaging Spectrometer to acquire data of UCD candidates detected in several images of the core of Coma taken with the Advanced Camera for Surveys.

Chiboucas et al. (2011) took spectra of UCDs present in 19 ACS pointings of the core of Coma. These 19 pointings were taken as part of the HST/ACS Coma Cluster Survey (Carter et al. 2008) and include the field of NGC 4874 studied in previous sections. Chiboucas et al. (2011) confirmed a total of 27 Ultra-Compact Dwarfs in Coma, that is, in the 19 ACS pointings mentioned above. By estimating the Lick indices strengths of the absorption lines of UCDs, Chiboucas et al. (2011) found that UCDs in Coma have metallicities of -1.3 $\lesssim [Fe/H] \lesssim -0.6$. Other physical characteristics such as sizes, ages, and colors of the UCDs spectroscopically confirmed by Chiboucas et al. (2011) are also in the range of previously discovered UCDs in other galaxy clusters.

Five of the UCDs reported in this chapter were part of this Keck survey and all of them received spectroscopic confirmation. The UCDs that were confirmed with Keck are naturally among the brightest candidates ($M_I > -13.5$) reported in this chapter owing to the onerous task of acquiring spectra of very faint candidates. The confirmation of a handful of candidates gives assurance about the method used in this chapter to discover new UCDs in Coma. As we will show later in Chapter 4, spectroscopic follow up is a crucial step to determine the true nature of UCD candidates.

3

Ultra-Compact Dwarfs in the Fossil Group NGC 1132

3.1 Fossil Groups

The search for UCDs has been focused in galaxy clusters and observations seeking to discover UCDs in other environments are critically needed to understand their formation process and to determine how common these low-mass stellar systems truly are. Only recent accounts of UCDs outside galaxy clusters with spectroscopic confirmation exist in the literature. Evstigneeva et al. (2007) search for UCDs in six galaxy groups using ground based data and find only one definite candidate in the Dorado group. Romanowsky et al. (2009) describe UCDs in the galaxy group of NGC 1407 while Hau et al. (2009) find a UCD located in the vicinity of the Sombrero Galaxy, a low density environment. Da Rocha et al. (2011) give a detailed account of the UCDs present in two Hickson compact groups. Recently, and after discovering UCDs in field (NGC 4546) and group (NGC 3923) environments, Norris & Kannappan (2011) claim the ubiquity of UCDs in galaxies with populous globular cluster systems.

A search for UCDs is undertaken in the isolated giant elliptical NGC 1132 shown in Figure 3.1. This galaxy is likely the remnant of a merged galaxy group, or fossil group. Fossil groups have a defining characteristic gap of two magnitudes between the brightest galaxy and the second brightest galaxy. This dominant galaxy is believed to be the end product of the merger of a galaxy group into a single entity (Ponman et al. 1994). Fossil groups have X-ray luminosities comparable to galaxy groups but a characteristic absence of $L^{\star}$ galaxies (Jones et al. 2003). The temperature, metallicity, and luminosity of the X-ray halo surrounding NGC 1132 are similar to those of galaxy groups (Mulchaey & Zabludoff 1999). Analysis of the Millenium Simulation (Springel et al. 2005) shows that

fossil groups assembled their dark matter halos early, accumulating 80% of the present day mass 4 Gyr ago (Dariush et al. 2007). The absence of parent galaxies and thus lack of substructure in fossil groups has been debated as a possible challenge to the ΛCDM paradigm, similar to the missing galaxy problem of the Local Group (Sales et al. 2007 and references therein).

Fossil groups are dynamically evolved environments and due to their early assembly and their fast evolution the dominant galaxy has had time to accrete the most massive surrounding galaxies through dynamical friction (Mulchaey & Zabludoff 1999). Dwarf galaxies are exempt from the consequences of dynamical friction given that this effect is proportional to the mass of the satellite galaxy. Also, given that ram pressure stripping is milder in a fossil group than in the core of a galaxy cluster, UCDs formed by downsizing dwarf galaxies (Bekki et al. 2003) are expected to survive up to the present day in fossil groups.

This work uses the same method employed by Madrid et al. (2010; Chapter 2, hereafter Paper I) to determine the presence of UCDs in the Coma Cluster. The brightest UCD candidates reported in Paper I have been spectroscopically confirmed by Chiboucas et al. (2010) using the Keck telescope. The fainter end of the luminosity distribution of UCD candidates presented in Paper I lacks spectroscopy confirmation simply due to the onerous challenge of obtaining their spectra at the Coma distance.

Collobert et al. (2006) give a redshift of $z = 0.023$ for NGC 1132, and distance modulus of (m-M)=34.86 mag equivalent to a luminosity distance of 99.5 Mpc using H_0=71 km.s^{-1}Mpc^{-1}, $\Omega_M = 0.27$, and $\Omega_\Lambda = 0.73$ (Wright 2006).

3.2 Data and Reductions

The observations of NGC 1132 are carried out with the Advanced Camera for Surveys Wide Field Channel (ACS/WFC) on 2006 August 22. The data is acquired in two bands: $F475W$, similar to Sloan g, and $F850LP$, Sloan z (Mack et al. 2003). Four exposures are obtained in each band for a total exposure time of 4446 s in $F475W$ and 6885 s in $F850LP$. The pixel scale of the ACS/WFC is 0.05 arcseconds/pixel (23pc/pixel) and the physical scale of the field of view is $\sim 93 \times 93$ kpc at the distance of NGC 1132. The same physical scale is covered in the study of Paper I.

Eight flatfielded science images (FLT.FITS) are retrieved from the public archive hosted at the Space Telescope Science Institute. These files are pre-processed through the standard pipeline that corrects bias, dark current, and flatfield (Sirianni et al. 2005). The

PYRAF task MULTIDRIZZLE is used to combine the different exposures within the same filter, remove cosmic rays, and perform distortion correction.

Detection of sources is carried out with SExtractor (Bertin & Arnouts 1996) using a detection threshold of 3σ above the background. Source Extractor is run on both images: $F475W$ and $F850LP$, both images were registered. Sources must be present in both bands in order to be included in the master catalogue. A careful round of visual inspection allows for the discarding of contaminants such as background galaxies. As recently shown by the Galaxy Zoo project the human eye remains a powerful tool to discriminate between different types of galaxy morphology (Lintott et al. 2011).

As in Paper I the empirical point spread function is created by running the PYRAF tasks PSTSELECT, PSF, and SEEPSF. These tasks respectively select bright unsaturated stars from the image, build the PSF by fitting an analytical model (Moffat function), and subsample the PSF as required by the software used to determine the structural parameters.

3.3 Analysis

3.3.1 Structural Parameters

Structural parameters are determined using ISHAPE (Larsen 1999) following the same procedure discussed in Chapter 2. A King profile (King 1962, 1966) with a concentration parameter, or tidal to core radius, of c=30 is the most suitable analytical model for fitting the surface brightness profile of globular clusters and UCDs (as discussed in the previous chapter). The structural parameters of 1649 point-like sources are derived in both bands. The values of structural parameters quoted hereafter are those corresponding to the $F850LP$ band given its longer exposure time. This filter is also a better tracer than blue filters of the mass of globular clusters and UCDs. F814W (I) has been used as mass tracer by various studies, e.g. Harris et al. (2006).

3.3.2 Photometry

Photometry is performed using an aperture of 4 pixels in radius with the task PHOT within the DAOPHOT package of PYRAF. Aperture correction is applied using the formulas of Sirianni et al. (2005). Photometric measurements are obtained for all 1649 stellar objects identified as globular clusters and UCD candidates in the ACS images of NGC 1132.

Foreground extinction for NGC 1132 is $E(B-V) = 0.063$ mag (from the NASA Extragalactic Database – NED) and the specific extinction corrections applied to each

Figure 3.1 Color image of NGC 1132 created by the Hubble Heritage Team. This image was created with the same data used for the analysis presented in this chapter. No claim of copyright is made by the creators of this image.

HST filter are obtained following the prescriptions of Sirianni et al. (2005) which give $A_{F475W} = 0.229$ mag and $A_{F850LP} = 0.094$ mag. Up-to-date photometric zeropoints for ACS/WFC are obtained from the STScI website: $F475W = 26.163$ mag and $F850LP = 24.323$ mag. These zeropoints yield magnitudes in the Vega magnitude system.

3.3.3 Selection Criteria

As discussed in Chapter 2, UCDs are selected based on their color, magnitude and structural parameters. A metallicity break found by Mieske et al. (2006) at the onset of the luminosity-size relation sets at $M_V = -11$ mag the luminosity cutoff to distinguish between simply bright globular clusters and UCDs. At the distance of NGC 1132 this luminosity requirement translates to $m_{F850LP} < 22.3$ mag– this value is obtained using CALCPHOT within the SYNPHOT package of STSDAS (Laidler et al. 2005). In color, UCD candidates must be in the same range defined by the globular cluster system. This is shown in the next section to be $1 < (F475W - F850LP) < 2.5$ mag.

In size, UCDs are conventionally, but arbitrarily, defined as stellar systems having an effective radius between 10 and 100 parsecs (as already discussed in Chapter 2). UCDs must be consistently resolved in both bands: at the distance of 100 Mpc this condition is satisfied for sources with $r_h > 8$pc with the deep images analyzed in this work.

In photometric studies, and as a safeguard against contamination by background galaxies, the ellipticity of UCDs is expected to be between $\epsilon = 0$ and $\epsilon = 0.5$ (Blakeslee & Barber de Graff 2008; Paper I). All UCD candidates fall within that range of ellipticity. Additionally, a signal-to-noise ratio of $S/N > 50$ is a requirement for obtaining a reliable estimate of structural parameters with ISHAPE (Harris 2009).

3.4 Results

The Color-Magnitude Diagram (CMD) of the globular cluster system associated with NGC 1132 is used to define the parameter space where UCDs are expected to be present, a detailed analysis of this CMD is not the aim of this work.[1] For most globular clusters (99% of them) their colors are in the range $1 < (F475W - F850LP) < 2.5$ mag and their magnitudes between $21 < F850LP < 26$ mag as shown in Figure 3.2. This broad color range translates into a metallicity range of $-2.61 < [Fe/H] < -0.10$ dex given by the color-metallicity transformation of Peng et al. (2006). The deduced metallicity range is in

[1] We were informed by John Blakeslee that Michael West intended to publish a complete analysis of this CMD. Their paper was indeed published in 2012 by Alamo-Martínez, West, Blakeslee et al. When possible, we try to avoid unnecessary duplications.

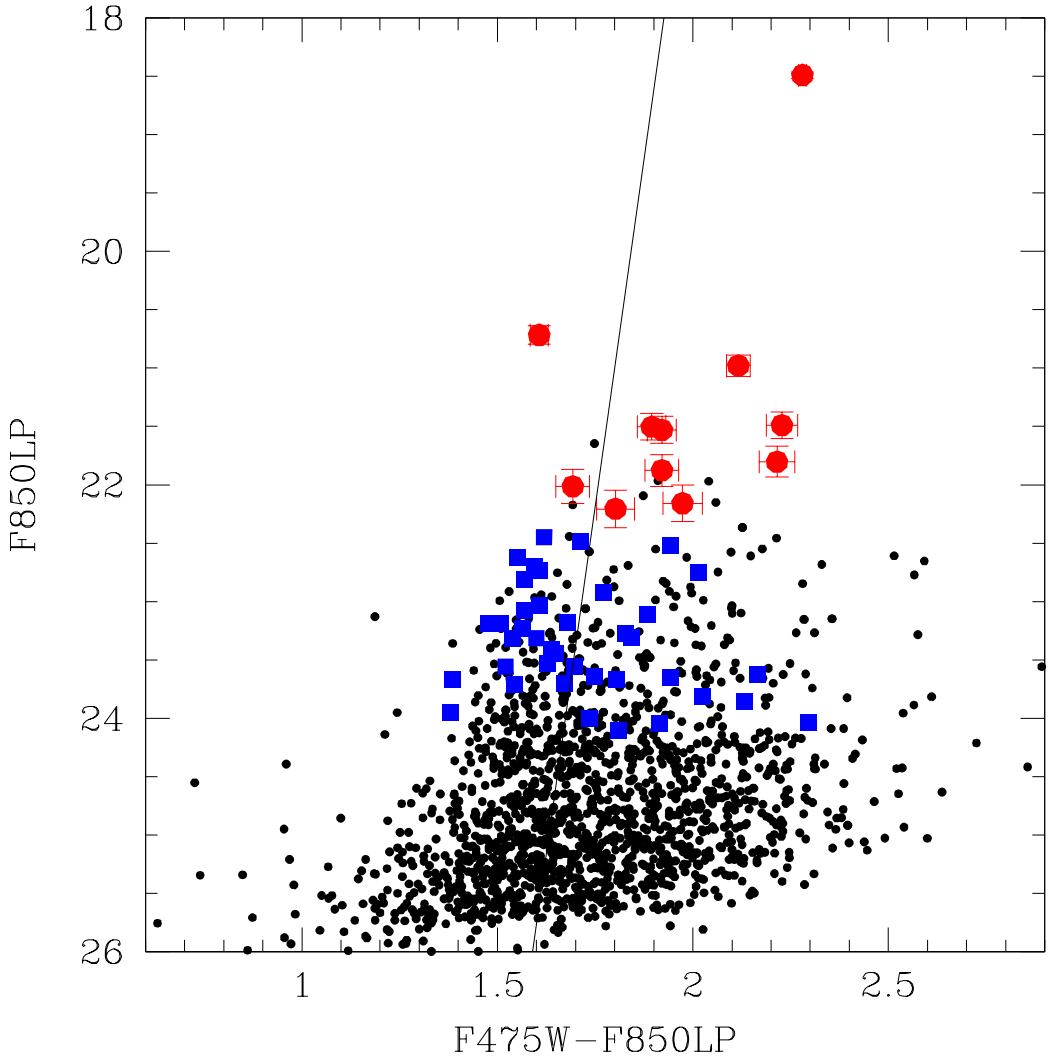

Figure 3.2 Color-Magnitude Diagram of the globular cluster system associated with the isolated elliptical NGC 1132. Unresolved globular clusters are plotted as black dots. UCD candidates are represented by red circles and extended clusters are plotted as blue squares. The line shows the Mass Metallicity Relation with a slope of $\gamma_z = 0.042$, see Peng et al. (2009) for a discussion.

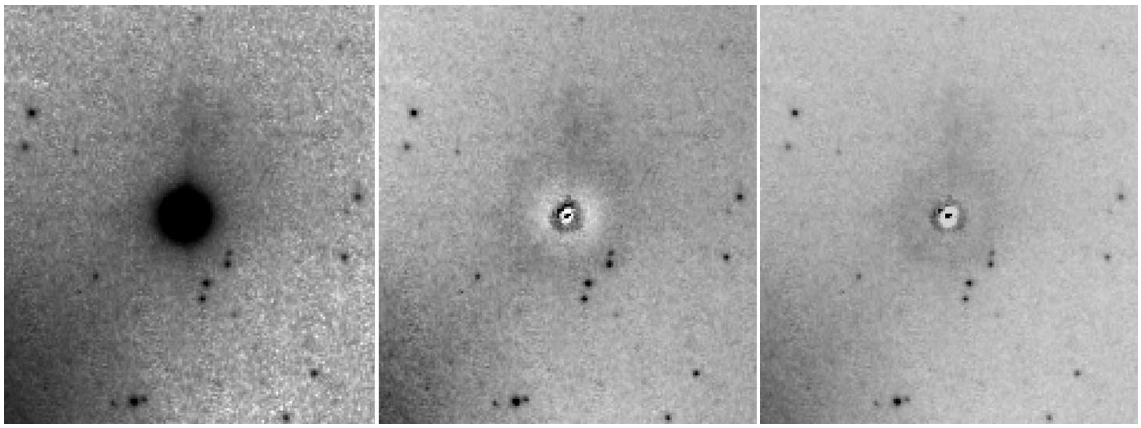

Figure 3.3 M32 counterpart in the Fossil Group NGC 1132. From left to right: original $F850LP$ image; residual of best fit using GALFIT and a Sérsic model with n=2.4; residual of best fit using ISHAPE and a King model with $c = 30$.

agreement with previous metallicity estimates of UCDs (Mieske et al. 2004; Evstigneeva et al. 2007).

The vast majority of the 1649 globular clusters and UCD candidates identified in the ACS images remain unresolved or their S/N is too low to obtain a truly reliable estimate of their structural parameters. However, 11 sources satisfy the color, magnitude, size, and S/N criteria outlined above to be classified as UCD candidates. The effective radii of these 11 UCD candidates range from 77.1 pc, for the largest and brightest candidate, to 8.5 pc. The median effective radius for UCDs is $r_h = 13.0$ pc with a standard deviation of $\sigma = 19.8$ pc. Excluding the brightest candidate brings these numbers to $r_h = 11.4$ pc and $\sigma = 5.1$ pc. All 11 UCD candidates have a $S/N > 90$ and are plotted as red dots in the color-magnitude diagram of Figure 3.2. In color and magnitude most UCDs overlap with the brightest globular clusters, the very same is the case for UCDs in the core of the Coma cluster, i.e. they share the same parameter space of the brightest globular clusters associated with NGC 4874 (Paper I).

3.4.1 A M32 Equivalent

The brightest UCD candidate is a M32-like object located, in projection, ∼6.6 kpc away from the center of the galaxy. Its effective radius is $r_h = 77.1$ pc, its magnitude $m_{F850LP} = 18.49$ mag, or two magnitudes brighter than the second brightest UCD candidate, and its color is particularly red: $(F475W - F850LP) = 2.28$ mag. In the framework of a dual formation mechanism for UCDs proposed by Da Rocha et al. (2011) and Norris &

Kannappan (2011), this candidate is the remaining nucleus of a stripped companion of NGC 1132 owing to the clear gap of two magnitudes between the brightest globular clusters and this UCD. This object is similar to SDSS J124155.3+114003.7, the UCD reported by Chilingarian & Mamon (2008) at a distance of 9 kpc from M59.

As stated by Norris & Kannappan (2011) no globular cluster system has a luminosity function continuously extending up to such high luminosity. As shown in Paper I, not even the extremely rich globular cluster system of NGC 4874 in the core of the Coma cluster has members with magnitudes similar to the brightest UCD candidate. This object was catalogued by the Two Micron All Sky Survey as 2MASS-02525121-0116193, and its K band magnitude is $M_K = -13.505$ mag (Skrutskie et al. 2006).

A size estimate for the M32 counterpart was also carried out with GALFIT (Peng et al. 2002) using a Sérsic model with an initial Sérsic index of $n = 2$ (Sérsic 1968). Using GALFIT, the best fit for this object has a reduced χ^2=1.008 and yields $n = 2.4$, and $r_h = 89.2$ pc. The original image of the brightest UCD and the residual after model subtraction with both GALFIT and ISHAPE is given in Figure 3.3. The best fit of two different analytical models and different software leaves a small residual in the core. Similar residuals are found by Price et al. (2009) studying several compact elliptical galaxies in the core of the Coma Cluster. The brightest UCD candidate is comparable to, but slightly smaller than, the compact elliptical galaxies studied by Price et al. (2009) which have effective radii of $r_h \sim 200$ pc. This object also has comparable brightness to the Price compact ellipticals which have magnitudes ranging from $M_B = -16.66$ mag to $M_B = -13.67$ mag. Photometric and structural parameters of the eleven UCD candidates are presented in Table 3.1.

3.4.2 Extended Star Clusters

An additional 39 sources are positively resolved in both bands and have effective radii between 8.2 pc and 59.7 pc, with a median $r_h = 11.6$ pc. While these sources have the size characteristic of UCDs their magnitudes fall short of the minimum threshold for the selection criteria. These extended stellar systems have received several denominations. Here we refer to them as extended star clusters. Extended star clusters are plotted as blue squares on the CMD of Figure 3.2. Even if these extended star clusters are not as bright as UCDs, in luminosity some of these objects are comparable to ω Centauri ($M_I = -11.3$ mag).

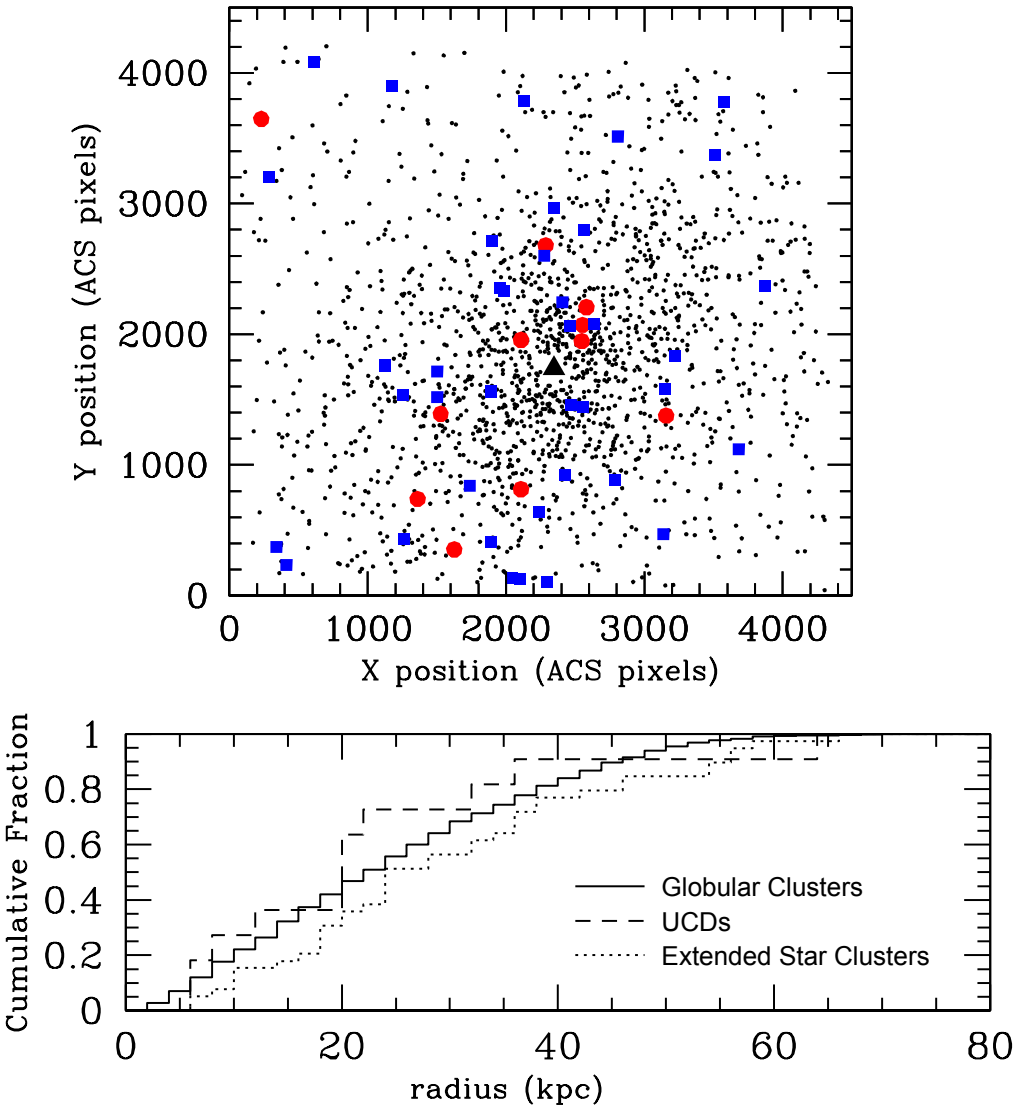

Figure 3.4 Spatial distribution of compact stellar systems in the Fossil Group NGC 1132. *Top panel*: positions of all globular clusters as black dots, extended star clusters as blue squares and UCDs as red circles. *Bottom panel*: Cumulative fraction for all the stellar systems listed above. The maximum difference between the cumulative fractions is greater than in Coma (Chapter 2). Both panels show that globular clusters, extended star clusters, and UCDs congregate around the central galaxy designated by a black triangle ($x = 2347, y = 1740$) in the center of the top panel. The brightest UCD is located 6.6 kpc from the center of the galaxy: $x = 2547, y = 1946$.

3.5 Spatial Distribution

The position of globular clusters, extended star clusters, and UCDs on the ACS frame are plotted in the top panel of Figure 3.4. All these low-mass stellar systems congregate towards the central elliptical arguing against background contamination (this is also shown in the bottom panel). Five UCDs and seven extended star clusters are found within the inner 12 kpc (in projection) to the center of the galaxy.

The maximum difference between the cumulative distributions of UCDs and ESCs is $D = 0.20$ with a corresponding probability $P = 0.241$. P is the probability of the two cumulative frequency distributions of two identical populations to have the observed separation D. As mentioned in the caption of Figure 3.4 the cumulative fraction maximum difference (D value or supremum) between UCDs and ESCs is larger in the the Fossil group than in the Coma cluster. Given the small number of objects (11 UCDs) a more elaborate interpretation is difficult to establish at this point.

In Paper I no UCDs were found within the inner 15 kpc of the center of NGC 4874. As noted in the introduction a milder tidal field and ram pressure stripping within a fossil group can allow UCDs and extended star clusters to survive up to the present day at small galactocentric distances – to be discussed later in Chapter 5.

3.6 Magnitude-Size Relation, Mass-Metallicity Relation

One of the defining characteristics of UCDs is their magnitude-size relation. UCDs are the smallest stellar systems that show a correlation between luminosity (or mass) and size (Hasegan et al. 2005). With masses of $\sim 2 \times 10^6 M_\odot$ these objects are indeed at the onset of this relation. We can see a clear hint of the magnitude-size relation for the 11 UCD candidates in Figure 3.5. Magnitude and r_h for the 11 UCDs in Figure 3.5 have a Spearman rank correlation coefficient of $\rho = 0.7$. The correlation is not perfect (i.e. $\rho = 1$) due to the scatter characteristic of such plots. No magnitude-size correlation is found for extended star clusters which gives $\rho = 0.15$ (see Figure 3.5). The effective radius of globular clusters with masses below $\sim 2 \times 10^6 M_\odot$ do not show any correlation with luminosity either, with a coefficient of $\rho = 0.1$ derived by McLaughlin (2000), that is, almost completely uncorrelated (i.e. $\rho = 0$).

A second correlation for stellar systems with masses of $\sim 10^6 M_\odot$ and above is the mass-metallicity relation (Harris et al. 2006; Strader et al. 2006). UCDs also obey this relation. The mass-metallicity relation (MMR) is evident in two simple ways in the CMD of Figure 3.2. At the distance of NGC 1132 ($\sim$ 100 Mpc) the paradigmatic bimodality

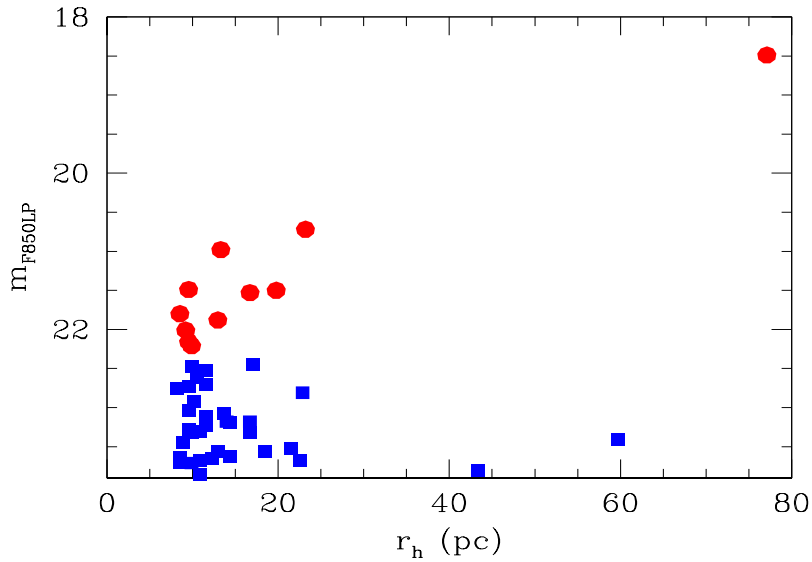

Figure 3.5 Magnitude vs. size of the 11 UCD (red circles) and 39 extended star cluster (blue squares) candidates associated with NGC 1132. UCDs trace the onset of a correlation between size and luminosity absent for extended star clusters and globular clusters.

of the GCS is blurred, however if we consider the measurements presented by Da Rocha et al. (2011) for GCSs of compact groups at lower redshift, the color of the metal-poor subpopulation of globular clusters is $(F475W - F850LP) \sim 1.6$ mag. In the CMD of Figure 3.2 blue globular clusters do not extend to luminosities higher than $F850LP \sim 22.5$ mag. With only one exception, no clusters or extended objects are found to have the colors of blue globular clusters and luminosities higher than $F850LP \sim 22.5$ mag. The second brightest UCD, located 20.6 kpc away from the galaxy center, is exceptionally blue $(F475W - F850LP) = 1.61$ mag and stands out of the MMR.

A second manifestation of the MMR quantified in a simple way is the median color of UCDs and extended star clusters. Self-enrichment models (Bailin & Harris 2009) predict that more massive (and bigger) objects migrate in color towards the red. UCDs that are more massive than extended globular clusters have indeed redder colors on average. The median color for UCDs is $(F475W - F850LP) = 1.92$ mag with $\sigma = 0.22$ while the median color for extended globular clusters is $(F475W - F850LP) = 1.67$ mag with $\sigma = 0.21$. The brightest UCD candidate is also the reddest with a color of $(F475W - F850LP) = 2.28$ mag – this is in agreement with the findings of Norris & Kannappan (2011). In contrast, the largest extended globular cluster with $r_h = 59.7$ pc has a blue color with $(F475W - F850LP) = 1.64$ mag. UCDs extend the MMR to brighter magnitudes than the end of the globular cluster luminosity function.

3.7 Discussion

Two highly evolved environments with fundamentally different densities are probed in Chapter 2 and in this chapter: the core of the Coma Cluster, the richest galaxy cluster of the nearby universe, and an isolated elliptical galaxy in a fossil group. Both systems exhibit similar characteristics of their UCD population with the exception that UCDs are present at small galactocentric distance (projected) in the fossil group and not in the galaxy cluster.

The presence of UCDs at the bright tip of the globular cluster systems of elliptical galaxies appears independent of environment. Given also the evidence provided by the works cited in Section 3.1 on the presence of UCDs outside galaxy clusters it is natural to infer that UCDs are commonly present in all environments. The results of this work support the thesis put forward by Norris & Kannappan (2011) on the ubiquity of UCDs in galaxies with populous globular cluster systems irrespective of environment.

Only the superior resolution of the Hubble Space Telescope allows for the determination

of the structural parameters of UCDs in the local Universe. Evstigneeva et al. (2007) searched for UCDs in five galaxy groups to no avail using ground based data. The groups studied by Evstigneeva et al. (2007) have both spirals and ellipticals as their central galaxy. These are not fossil groups thus a lesser number of mergers and interactions should have occurred. The higher number of galaxies that merge to form fossil groups, including dwarf galaxies, might be the precursors of UCDs though galaxy threshing (Bekki et al. 2003). In the case of NGC 1132 only UCD1 is an obvious candidate to be a dwarf galaxy remnant.

The fact that UCDs escaped detection for almost a decade while HST was operational is not a coincidence. HST can resolve UCDs only at relatively low redshift (D $\sim$ tens to hundreds of Mpc) however at these distances first and second generation instruments onboard HST (e.g. WFPC2) have small field of views that only cover physical scales of $\sim 10 \times 10$ kpc. UCDs are difficult to find within the innermost 10 kpc of the host galaxy (Paper I; Bekki et al. 2003; Da Rocha et al. 2011) not only owing to the crowding produced by starlight but also resulting from the destructive effects of the tidal field of the host galaxy (Bekki et al. 2003). An artificial maximum luminosity cutoff usually used in globular cluster studies has also certainly contributed to under-reporting of UCDs in the past (Norris & Kannappan 2011).

Spectroscopic confirmation of the brightest UCD candidates presented in this chapter is given in Chapter 4.

3.8 Discovery of New UCDs and Extended Star Clusters

Using the recent compilation of Brüns & Kroupa (2012) we can evaluate the contribution of this thesis to the discovery of new UCDs and extended star clusters. Brüns & Kroupa (2012) list 813 "extended objects" and include 75 objects presented in the previous two chapters of this thesis, that is 9% of their sample. A total of 102 new UCDs and ESCs were found during this thesis. Figure 3.6 gives a visual representation of the new compilation of Brüns & Kroupa (2012) – objects contributed by this thesis are plotted in red while objects found by other workers are plotted in black.

Table 3.1: **Structural and photometric parameters of UCD Candidates in NGC 1332.** Effective radius in pc measured in the F850LP band; ellipticity; signal-to-noise ratio; F850LP magnitude; F475W-F850LP color.

r_h	ϵ	S/N	m_{F850LP}	Color
(1)	(2)	(3)	(4)	(5)
77.1	0.09	1168	18.49	2.28
23.2	0.11	323	20.72	1.61
13.3	0.22	287	20.98	2.12
9.6	0.16	164	21.49	2.23
19.8	0.37	213	21.50	1.89
16.7	0.05	190	21.53	1.92
8.5	0.25	166	21.80	2.22
13.0	0.10	153	21.88	1.92
9.2	0.08	133	22.01	1.69
9.6	0.12	89	22.16	1.97
9.9	0.33	95	22.21	1.80

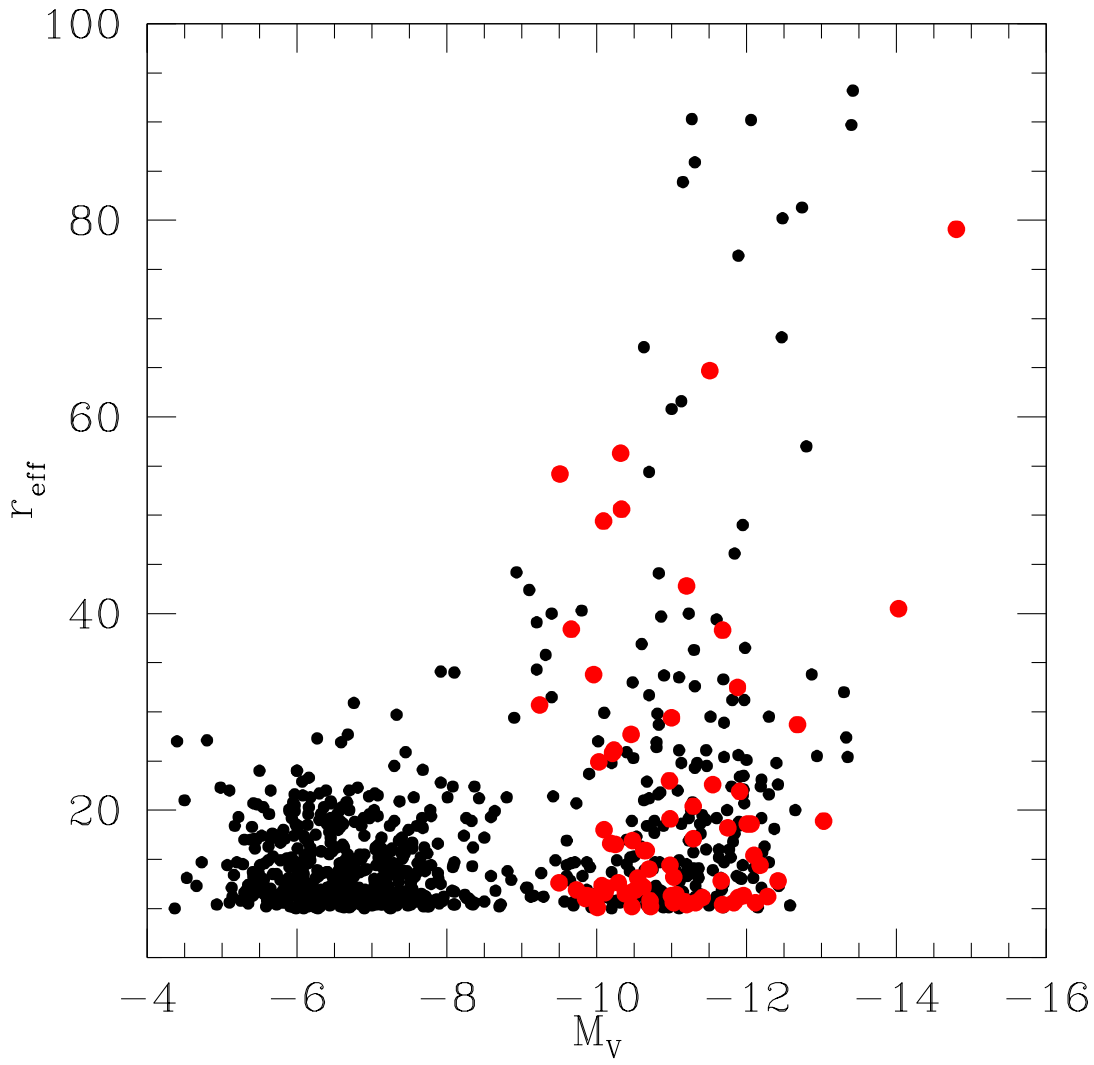

Figure 3.6 Effective radii vs. absolute V-band magnitude to demonstrate the contribution of this thesis to the discovery of new UCDs and extended star clusters. Data taken from the recent compilation of UCDs and extended star clusters by Brüns & Kroupa (2012). Objects discovered during this thesis are plotted in red, objects found by other workers in black.

4

Gemini Spectroscopy of Ultra-Compact Dwarfs in the Fossil Group NGC 1132

4.1 Motivation

Through the analysis of Advanced Camera for Surveys imaging, Madrid (2011; Paper II) found 11 UCDs and 39 extended star cluster candidates associated with the fossil group NGC 1132 (Chapter 3). These objects were identified through the analysis of their colors, luminosity, and structural parameters. In this chapter we present follow up Gemini spectroscopy of the brightest UCDs presented in the previous chapter.

Nine out of eleven UCD candidates found by Madrid (2011) share the same parameter space as the brightest globular clusters in the color magnitude diagram of the NGC 1132 globular cluster system. One UCD candidate, that will be designated as UCD1, is almost four magnitudes brighter than the brightest globular cluster associated with NGC 1132. UCD1 is 6.6 kpc from the center of NGC 1132, has a half-light radius of 77.1 pc and a magnitude of $F850LP = 18.49$ mag. A second UCD candidate, for which a spectrum was also obtained, had particularly blue colors compared to the the most luminous globular clusters.

The characteristics of UCD1 make it an interesting object since it is the link between the most massive UCDs found so far and the lowest mass M32-like galaxies. UCD1 is the brightest object in a recent compilation of 813 UCDs and extended objects (Brüns & Kroupa 2012). Indeed, high surface brightness compact elliptical galaxies, or M32-like stellar systems are rare. Chilingarian & Mamon (2008) list only six confirmed stellar systems similar to M32.

As pointed out recently by Brüns & Kroupa (2012) only one fifth of all published Ultra-Compact Dwarfs have been so far spectroscopically confirmed. In this chapter we

present the results of an observing campaign with Gemini North to obtain spectroscopic follow-up of UCD candidates in the fossil group NGC 1132 presented by Madrid (2011).

The surface brightness profile and the globular cluster system of the fossil group NGC 1132 were studied in detail by Alamo-Martínez et al. (2012). These authors find that both surface brightness and specific frequency of globular clusters ($S_N = 3.1 \pm 0.3$) in NGC 1132 are similar to those of normal elliptical galaxies.

4.2 Gemini North Observations

Spectra for seven UCD candidates, and the brightest globular cluster in the fossil group NGC 1132 were obtained with the Gemini North telescope using the Gemini Multi Object Spectrograph (GMOS). These observations were acquired under program GN-2012B-Q-10. UCD candidates were determined through the analysis of HST imaging, as discussed in previous chapters and the previous section. A multislit mask was created using a pre-image provided by Gemini, see Figure 4.1. Given that the Advanced Camera for Surveys onboard HST has a field of view of 202 × 202 arcseconds all targets are located within this small area centered on the host galaxy. The central concentration limited the total number of targets that fit on the GMOS slit mask.

The spectroscopic data were acquired in queue mode on 20 September 2012 using a multislit mask. Individual slits had a width of one arcsecond. The grating in use was the B600+_G5323 that has a ruling density of 600 lines/mm. Three exposures of 1800 s each were obtained with the central wavelengths of 497, and 502 nm. Two additional exposures of 1800 s each were obtained with a central wavelength of 507 nm. Science targets have thus a total exposure time of ∼4 hours. Flatfields, spectra of the standard star $BD + 284211$, and the copper-argon $CuAr$ lamp were also acquired to perform flux calibration. A binning of 2×2 was used, yielding a scale of 0.1456 arcseconds per pixel and a theoretical dispersion of ~ 0.9 Å per pixel. Our targets transit $\sim 30°$ from the zenith and if the position angle is set to 90° the displacement due to atmospheric refraction is small in our configuration. Slit losses resulting from atmospheric refraction can be neglected.

4.3 Data Reduction and Analysis

All science and calibration files were retrieved from the Gemini Science Archive hosted by the Canadian Astronomy Data Center. The data reduction described below was carried out with the Gemini IRAF package. Flatfields were derived with the task GSFLAT and the flatfield exposures. Spectra were reduced using GSREDUCE. This task does a standard data

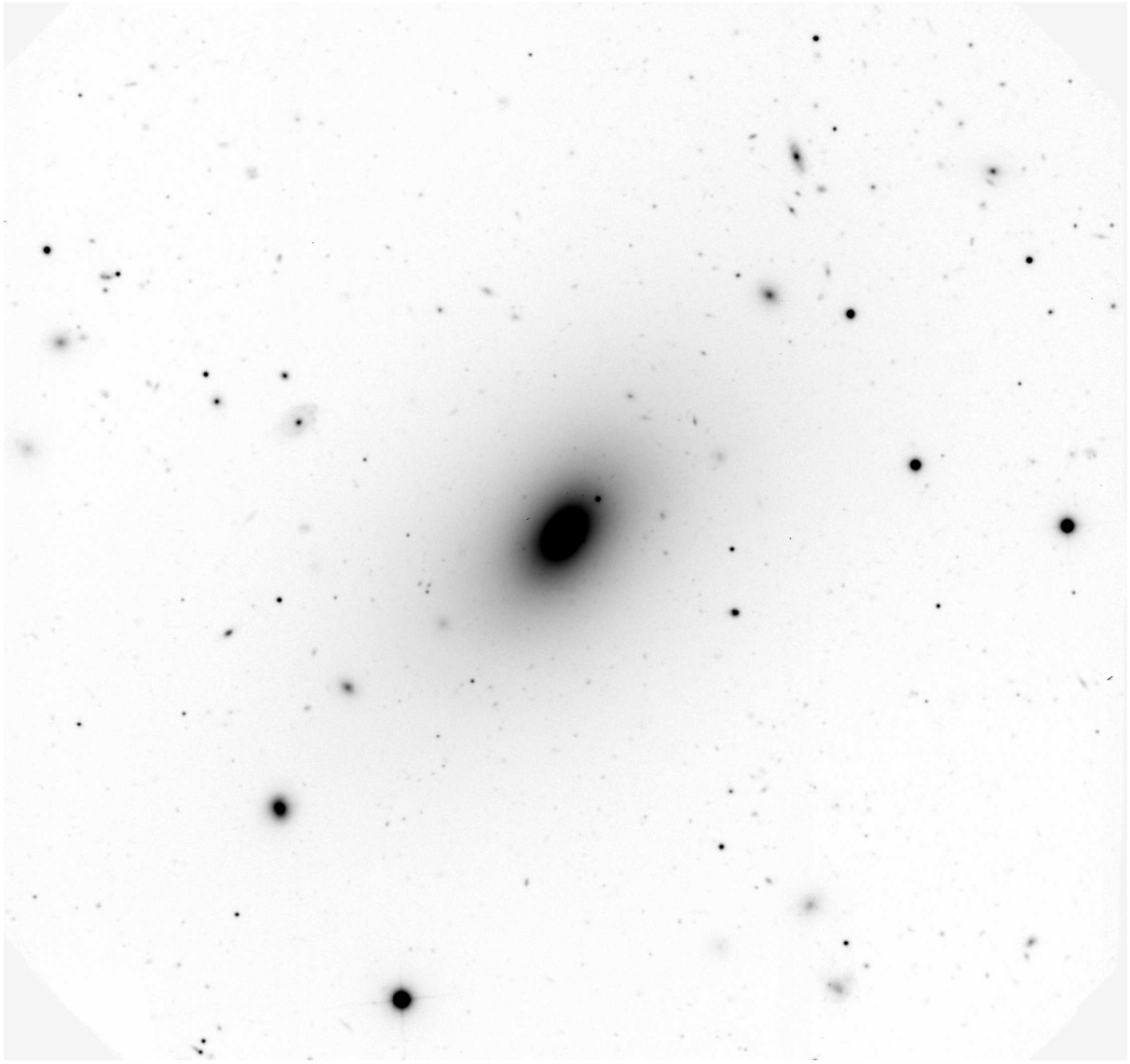

Figure 4.1 Gemini pre-image of the fossil group NGC 1132 taken with the $g-G0301$ filter. This image was used to build the multislit mask. The field of view is $\sim 150 \times 150$ kpc. North is up and east is left.

reduction, that is, performs bias, overscan, and cosmic ray removal as well as applying the flatfield derived with GSFLAT. GMOS-North detectors are read with six amplifiers and generates files with six extensions. The task GMOSAIC was used to generate data files with a single extension. The sky level was removed interactively using the task GSKYSUB and the spectra were extracted using GSEXTRACT. The spectra taken at the three different wavelengths mentioned above were then combined using SCOMBINE.

Flux calibration was performed using the spectra of the standard star $BD + 284211$, acquired with an identical instrument configuration. Spectra of $CuAr$ lamps were obtained immediately after the science targets were observed and were used to achieve wavelength calibration using the task GSWAVELENGTH. We use GSTRANSFORM to rectify, interpolate, and calibrate the spectra using the wavelength solution found by GSWAVELENGTH. The sensitivity function of the instrument was derived using GSSTANDARD and the reference file for $BD+284211$ provided by Gemini observatory. Science spectra were flux calibrated with GSCALIBRATE which uses the sensitivity function derived by GSSTANDARD.

4.4 Results

Figure 4.2 presents the calibrated spectra of six UCDs, the brightest globular cluster of the NGC 1132 globular cluster system, and a background galaxy thought to be a UCD with particularly blue colors. These objects are all brighter than $M_{F850LP} \sim 23.5$ mag as shown in Figure 4.3. Various absorption lines are identifiable in the spectra of UCDs, particularly in the spectrum of UCD1 which has a higher signal to noise ratio. The two most prominent absorption features in the spectrum of UCD1 are the magnesium and sodium doublets with restframe wavelengths of 5169, 5175 Å and 5890, 5896 Å respectively. These two doublets are also evident in the UCD spectra published by Francis et al. (2012). Other lines present in the spectrum of UCD1 are Ca and Fe (5269 Å), Fe (5331 Å; 4384), HeII (5411 Å), Hβ (4861 Å), and CaI (4227 Å). We should add the caveat that HeII (5411 Å) is not present in spectra of F or G-type stars (Da Costa, private communication 2013). The presence of this line might suggest that UCDs have a more complex stellar composition than a simple superposition of F and G stars.

4.4.1 Redshift Determination

The redshift of the targets is derived using the IRAF task FXCOR that computes radial velocities by deriving the Fourier cross-correlation between two spectra. As a reference spectrum we use data of the Galactic globular cluster BH 176 taken in the same GMOS

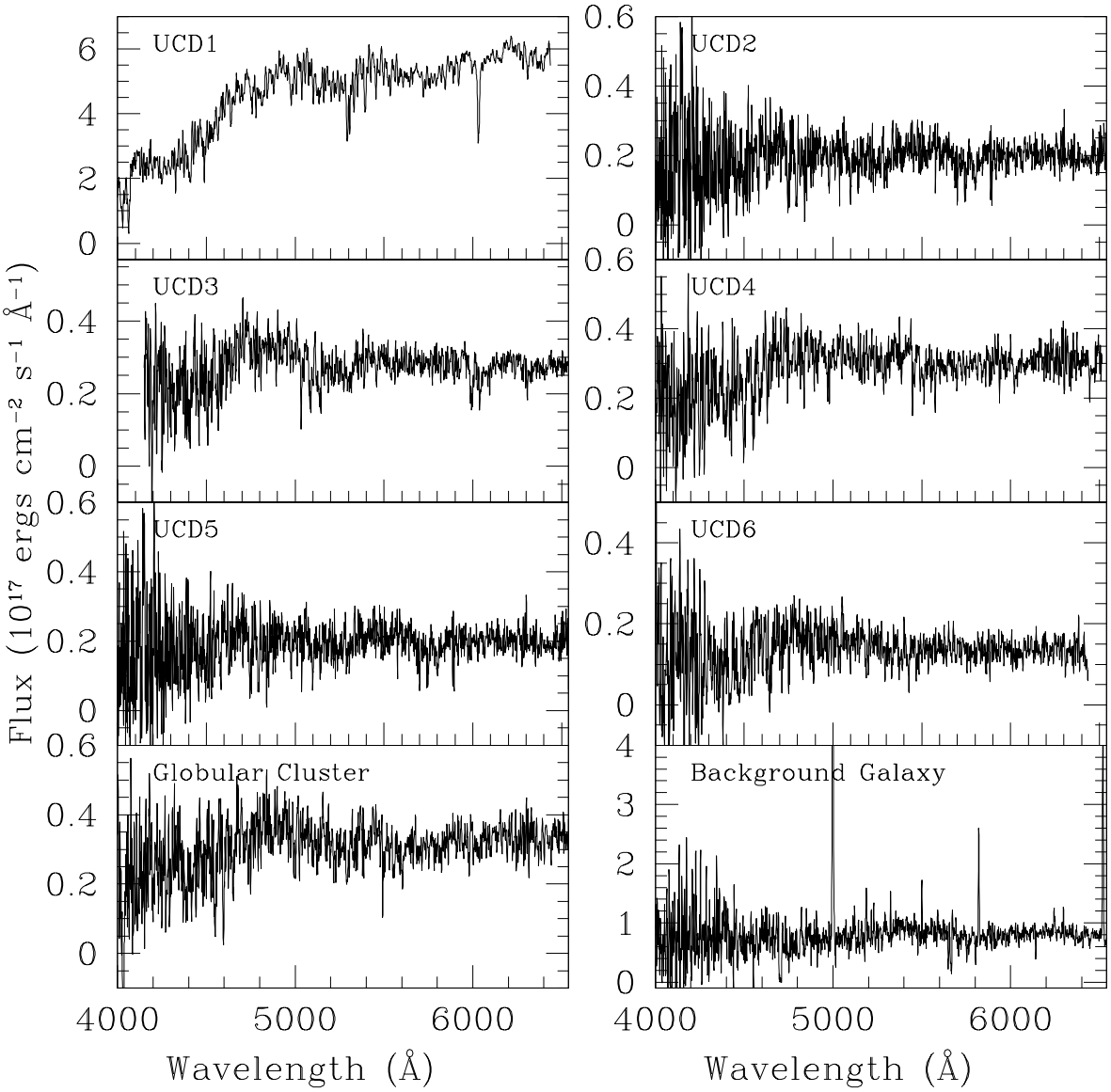

Figure 4.2 Calibrated Gemini/GMOS spectra of six confirmed UCDs, one globular cluster and a background galaxy in the NGC 1132 field. The most prominent lines of these spectra, particularly UCD1, are the magnesium and sodium doublets with restframe wavelengths of 5169, 5175 Å and 5890, 5896 Å respectively. Note that these spectra are not corrected for radial velocities.

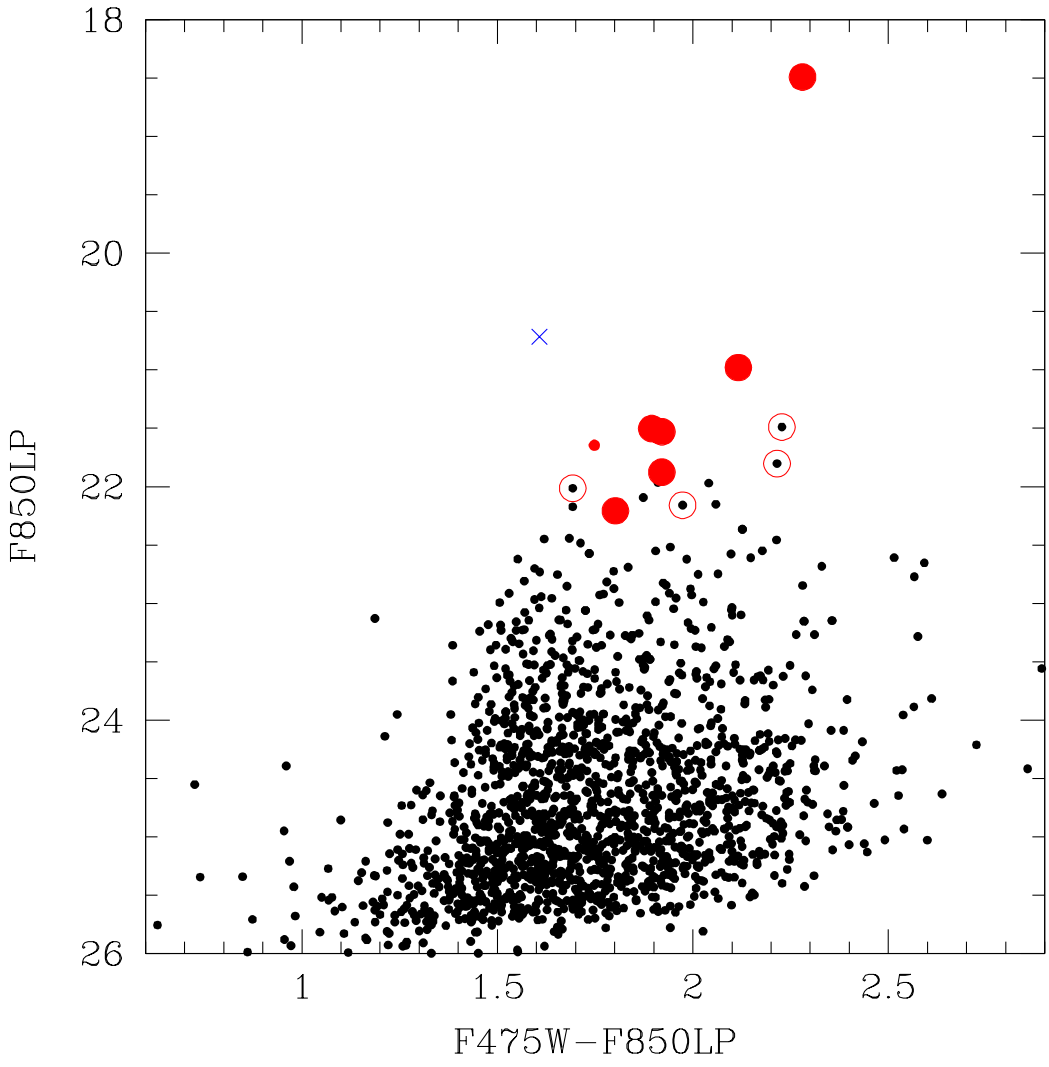

Figure 4.3 Color-Magnitude Diagram of the globular cluster system of NGC 1132 (black dots). UCD candidates are highlighted by open red circles. UCDs with membership to NGC 1132 confirmed with the Gemini data presented in this chapter are displayed as solid red circles. The small red point is GC1. The blue cross represents a background galaxy that masqueraded as an UCD candidate with blue colors in the HST images. A detailed analysis of the globular cluster system of NGC 1132 is given by Alamo-Martínez et al. (2012).

configuration during a previous Gemini run (Davoust et al. 2011). To carry out the cross-correlation we use the portions of the spectra with high signal-to-noise ratios, that region is generally above 4500 Å. The errors on the redshift are also derived using FXCOR.

For UCD1 the task FXCOR returns a radial velocity of 7158 ±32 km/s. The host galaxy NGC 1132 has a published radial velocity of 6935±11 km/s (Collobert et al. 2006). With these results we confirm that UCD1 is located within the fossil group NGC 1132 at a redshift of $z \sim 0.023$. This redshift measurement validates the photometric and structural parameters derived by Madrid (2011) for UCD1.

4.4.2 Age and Metallicity of UCD1, a M32-like Object

A caveat for this section is relevant: an accurate age and metallicity determination of the old stellar systems studied here is difficult. In a similar spectroscopic study of UCDs, Francis et al. (2012) derived the ages of 21 Ultra-Compact Dwarfs using both Lick indices and spectral fitting of Simple Stellar Populations and the results of these two techniques do not correlate with one another. The metallicities of these 21 UCDs, also derived by Francis et al. (2012), have better uncertainties and show a correlation between the two methods with an offset of 0.2 dex.

The stellar populations synthesis code STARLIGHT (Cid Fernandes et al. 2005) was used with the aim of deriving the metallicity of UCD1. STARLIGHT compared the Gemini spectrum of UCD1 with a database of 150 spectral templates and found that the best fit is provided by a combination of two stellar populations: one representing 30% of the flux and having solar metallicity (Z=0.02) and a second population accounting for 70% of the flux and having supersolar metallicity ($Z = 0.05$). This spectral fitting also yields an age of 13 Gyr for UCD1.

For spectra with sufficient signal-to-noise, Lick indices (Worthey et al. 1994) can be derived. The code GONZO (Puzia et al. 2002) was used to derive Lick indices for UCD1 which is the only UCD with enough signal to generate significant results. The Gemini spectrum is degraded to the Lick resolution by GONZO. We also apply the zero points of the calibration given by Loubser et al. (2009). The values for the Lick indices and their associated Poisson errors are given in Table 4.1, this allows comparison with existent and future studies. By comparing the indices $<$ Fe $>$ and Mgb to the single stellar population models of Thomas et al. (2003) we can derive an α-element abundance for UCD1 of [α/Fe]=+0.3 dex. Indices Hβ=1.96 Å and Fe 5270 = 3.57 Å of UCD1 are very similar to the values derived by Chiboucas et al. (2011) for UCD 121666 in the Coma cluster. UCD 121666 has an Hβ=1.84 Å and Fe 5270 = 3.48 Å.

The Lick indices we obtained were given as input to the publicly available code EZ Ages (Graves & Schiavon 2008). This code determines ages and abundances of unresolved stellar populations using their Lick indices. We chose an alpha-enhanced isochrone fitting and found an age of 7.5 Gyr and an iron abundance of [Fe/H]= -0.17 dex. Note that the iron abundance of M32 is [Fe/H]= -0.2 dex (Monachesi et al. 2011). The chemical abundances of Grevesse & Sauval (1998) yield a metallicity of $Z = 0.015$. The metallicity derived for UCD1 is high among UCDs but not unprecedented (Chiboucas et al. 2011; Francis et al. 2012). Indeed, the iron abundances of UCDs published by Chiboucas et al. (2011) range from 0.17 to -0.62 dex.

Table 4.1: **Lick Indices for UCD1 (Å)**

$H\beta$	$H\delta$A	$H\gamma$A	Mgb	Fe 5270	Fe 5335	< Fe >	[MgFe]
1.96 ±0.02	-1.92 ±0.15	-7.69 ±0.15	5.03 ±0.02	3.57 ±0.02	1.86 ±0.01	2.7 ±0.02	3.1 ±0.03

4.4.3 Internal Velocity Dispersion

The main objective of this work is to obtain redshifts for the UCD candidates. Determining their internal velocity dispersion, roughly of a few tens of kilometers per seconds is beyond the resolution of these Gemini/GMOS observations. The empirical spectral resolution of our observations has a FWHM$\sim$ 200 km/s at 5000Å, that is about ten times the value of published internal velocity dispersion of UCDs (e.g. σ_v = 20.0 km/s: Hasegan et al. 2005). Chiboucas et al. (2011) study the UCDs of the Coma Cluster, exactly at the same distance of 100 Mpc as NGC 1132, with the Keck telescope and also refrain from deriving internal velocity dispersions owing to the low resolution of their spectra.

4.4.4 UCD Population in the Fossil Group NGC 1132

The redshifts derived with these new Gemini spectra confirm six UCD candidates as true members of the fossil group NGC 1132. The redshifts, photometric, and structural parameters of these UCDs are listed in Table 4.2. UCD2 through UCD6 are the extension to higher luminosities and redders colors of the brightest globular clusters of NGC 1132. The sizes of UCD2 through UCD6 range between 9.9 to 19.8 pc and all globular clusters have a size smaller than $\sim$8 pc. The Color-Magnitude Diagram (CMD) of the NGC 1132 globular cluster system is plotted in Figure 4.3. This CMD also contains the colors and magnitudes of UCD candidates and objects with spectroscopic data.

These six UCDs have an average radial velocity of $< v_r >= 6966 \pm 85$ km/s. The velocity dispersion of this family of UCDs is $\sigma = 169 \pm 18$ km/s which is in the range of poor galaxy groups, as discussed below. The velocity dispersion was derived, through bootstrapping, using the prescriptions of Strader et al. (2011; their Equation 4). UCDs can be used in the same manner as globular clusters and planetary nebulae have been used to trace the dynamics of nearby galaxies (e.g. Coccato et al. 2009).

Table 4.2: **Radial Velocities, Photometric and Structural Parameters.** Column 1: Identifier; Column 2: Right Ascension (J2000.0); Column 3: Declination (J2000.0); Column 4: radial velocity; Column 5: apparent magnitude in the HST filter F850LP (similar to Sloan z); Column 6: absolute magnitude; Column 7: color (F474W-F850LP); Column 8: effective radius in parsecs. The size of GC1 is below the resolution limit of HST, in this case ∼8 pc in radius; Column 9: projected distance to the center of NGC 1132 in kpc.

ID	RA	Dec	Radial Velocity	m_{F850LP}	M_{F850LP}	Color	r_h (pc)	R_{GC} (kpc)
(1)	(2)	(3)	(4)	(5)	(6)	(7)	(8)	(9)
UCD1	2h52m51s	$-1°16'19''$	7158 ± 32	18.5	-16.4	2.28	77.1	6.6
UCD2	2h52m54s	$-1°17'39''$	6834 ± 84	21.0	-13.9	2.12	13 .3	36.0
UCD3	2h52m59s	$-1°14'54''$	7082 ± 69	21.5	-13.4	1.89	19.8	65.5
UCD4	2h52m52s	$-1°15'43''$	6627 ± 60	21.5	-13.3	1.92	16.7	21.7
UCD5	2h52m55s	$-1°17'19''$	6949 ± 120	21.9	-13.0	1.92	13.0	32.3
UCD6	2h52m51s	$-1°16'06''$	7147 ± 140	22.2	-12.7	1.80	9.9	12.0
GC1	2h52m53s	$-1°16'34''$	6948 ± 99	21.7	-13.2	1.75	–	5.6

4.4.5 A Blue UCD Candidate

In Madrid (2011) a particularly "blue" Ultra-Compact Dwarf candidate was reported. This UCD candidate satisfied all selection criteria based on size, ellipticity, magnitude and color. This candidate was the bluest UCD candidate and seemingly did not follow the mass-metallicity relation of massive globular clusters (M> $10^6 M_\odot$: Bailin & Harris 2009). A Gemini-GMOS spectrum of this object reveals that it is actually a background star-forming galaxy, with strong emission lines. The redshift of this "blue" UCD candidate is $z = 0.3410$ and the most prominent emission lines detected on this spectrum are [OII], and [OIII]. This object is represented by a cross on the CMD of Figure 4.3. Madrid (2011) showed that UCDs have, on average, redder colors than extended globular clusters.

4.4.6 Spatial Distribution of UCDs

The spatial distribution of globular clusters, UCD candidates, and UCDs with spectroscopic confirmation is presented in Figure 4.4. Both globular clusters and UCDs appear

to follow a similar spatial distribution. Globular clusters aggregate towards the center of the host galaxy as is expected for these satellite systems. There is no other particular clustering or alignement of UCDs in the ACS field. The projected galactocentric distances of UCDs are given in Table 4.2. At 6.6 kpc UCD1 is the closest UCD to the center of NGC 1132.

4.5 Discussion

4.5.1 Properties of the Fossil Group NGC 1132

Mulchaey & Zabludoff (1999) call for the use of dwarf galaxies as test particles for the study of the dynamics and dark matter halo of NGC 1132. UCDs can fullfil this role. In galaxy groups $M^\star$ galaxies are expected to merge in a fraction of a Hubble time while on the other hand dwarf galaxies have dynamical friction timescales greater than a Hubble time (Mulchaey & Zabludoff 1999). Albeit based on a small sample, the velocity dispersion of the UCD population can be used in existing scaling relations for the X-ray luminosity and group richness.

Several studies have derived a relation between X-ray luminosity (L_X) and velocity dispersion (σ_v) of galaxy clusters (Ortiz-Gil et al. 2004 and references therein), and galaxy groups (Xue & Wu 2000). Whether fossil galaxy groups follow the same scaling relations of galaxy clusters or have a shallower $L_X \propto \sigma_v$ relation is still a matter of debate (Khosroshahi et al. 2007).

A relation between X-ray luminosity (L_X) and velocity dispersion σ_v for galaxy groups is $L_X = 10^{-2.95\pm0.30}\sigma_v^{1.00\pm0.12}$ in units of 10^{42} erg/s (Xue & Wu 2000). If we insert the value for the velocity dispersion of UCDs $\sigma_v = 169$ km/s in the above formula the X-ray luminosity is $L_X = 0.2 \times 10^{42}$. This value is more than a factor of ten lower than the value reported by Mulchaey & Zabludoff (1999) of $\sim 2.5 \times 10^{42} h_{100}^{-2}$ erg/s. A better match to the observation is given by the relation between L_X and σ for galaxy clusters derived by Ortiz-Gil et al. (2004). These authors give the following relation for what they call a volume limited sample: $L_X = 10^{35.16\pm0.09}\sigma^{3.2\pm0.3}$. This formula yields $L_X = 1.9 \times 10^{42}$ erg/s, which is a better approximation to the observed value. In a recent work, Connelly et al. (2012) make a detailed analysis of a sample of galaxy groups and give $L_X - \sigma$ relations that depend on different factors, for instance, number of group members and radial cuts applied. One of the Connelly et al. (2012) relations yields an X-ray luminosity of $L_X \sim 3 \times 10^{43}$ erg/s. There is a discrepancy between the different $L_X - \sigma$ relations published in previous studies.

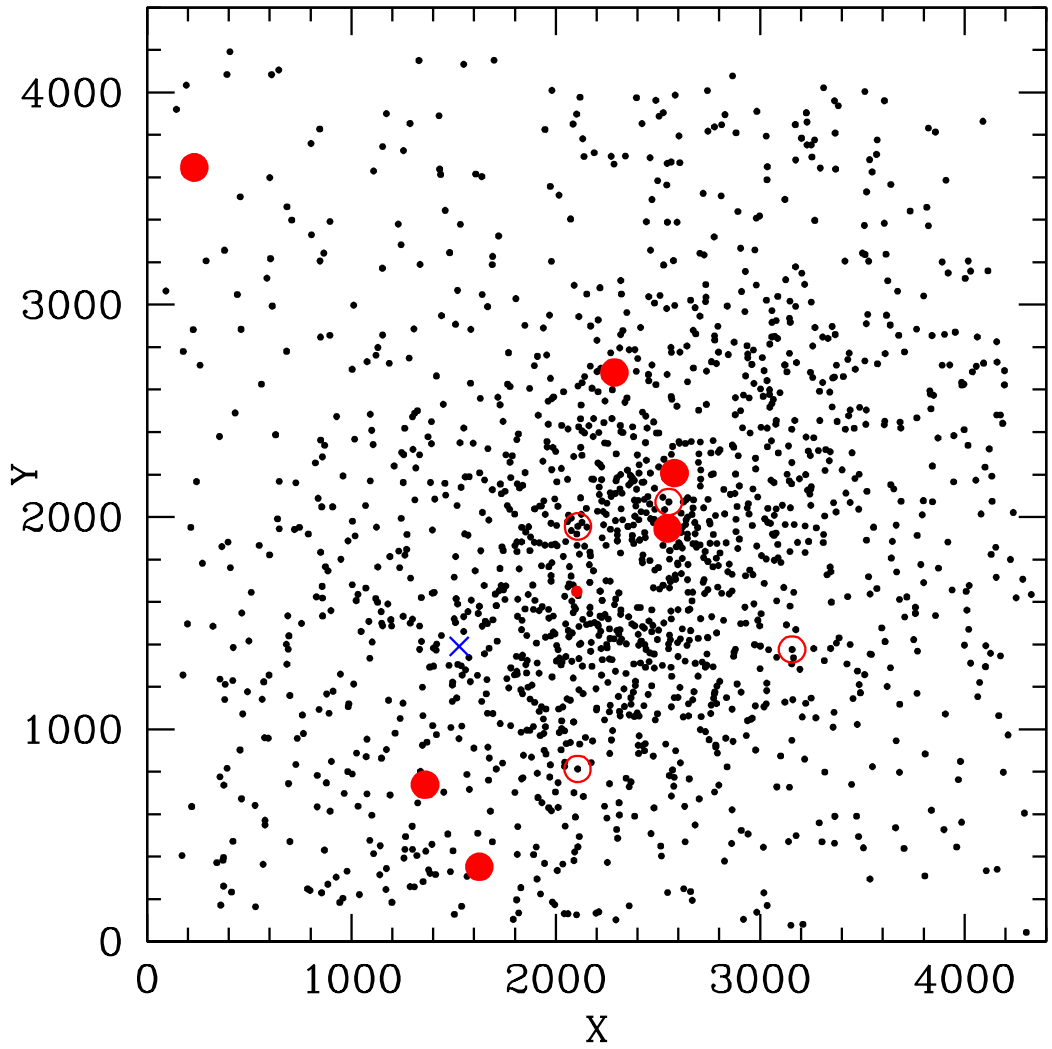

Figure 4.4 Spatial distribution of globular clusters (black dots), UCD candidates (open red circles), and UCDs with spectroscopic confirmation (solid red circles). The small red dot is GC1. The background galaxy with photometric properties indistinguishable from UCD candidates is represented by a blue cross. This figure represents the field of view of the Advanced Camera for Surveys that, at the distance of NGC 1132, corresponds to $\sim 100 \times 100$ kpc.

Pisani et al. (2003) derived a correlation between group richness, or the number of group members (N), and velocity dispersion: $\log N = 127 \log \sigma_v - 1.47$. If the velocity dispersion of UCDs are indicative of the primordial velocity dispersion of NGC 1132, according to the Pisani et al. (2003) formula the UCD population has the velocity dispersion corresponding to a poor group with N=22 members.

Mendes de Oliveira & Carrrasco (2007) report the velocity dispersion of, among other objects, two Hickson Compact Groups (HCGs) at low redshift: HCG 31 has a velocity dispersion of σ_v=60 kms/s and HCG 79 has a velocity dispersion of σ_v=138 km/s. At σ_v=169 km/s the velocity dispersion of NGC 1132 is higher than these two low redshift compact groups but lower than the average σ_v=300 km/s found for a collection of 20 groups by Mahdavi et al. (1999).

4.5.2 UCDs in Different Environments

Analysis of high resolution HST data is a very efficient method to discover new Ultra-Compact Dwarfs in very diverse environments. The combined study of luminosity, colors, and structural parameters, possible with high resolution imaging data, yields UCD candidates with very high spectroscopic confirmation rates as shown in this work and in the study of the Coma cluster (Chapter 3; Madrid et al. 2010; Chiboucas et al. 2011) among others. Searching for UCDs with seeing-limited data is a more arduous and unfruitful task (e.g. Evstigneeva et al. 2007). One drawback of HST detectors is their small field of view that only covers the innermost regions of host galaxies where the strongest tidal effects take place. This work along with the publications cited in Section 4.1 show that UCDs can be formed in environments with different evolutionary histories.

A historical scarcity of compact stellar systems with characteristic scale sizes between 30 and 100 parsecs created an unmistakable gap in size-magnitude relations between dwarf ellipticals, compact ellipticals and globular clusters. As mentioned earlier, Gilmore et al. (2007) have interpreted the gap in the parameter space defined by compact stellar systems as a sign of two distinct families of objects, reflecting the intrinsic properties of dark matter. Globular clusters would belong to a family of dark matter-free stellar systems while dwarf spheroidals and compact ellipticals form the branch where dark matter is present or even dominant. Gilmore et al. (2007) postulate that dark matter halos have cored mass distributions with characteristic scale sizes of more than 100 pc. UCD1, however, with an effective radius of 77.1 pc is precisely in this gap of compact stellar systems. The brightest UCDs are the ideal candidates to bridge the gap between compact ellipticals and globular clusters. Part of the gap is due to artificial selection effects introduced to

eliminate contaminants in photometric studies. For instance, in the ACS Virgo Cluster Survey an upper limit of 10 parsecs was imposed on globular cluster candidates. Recent reanalysis of data lifting the 10 parcsecs upper limit on size for compact stellar systems have uncovered new systems previously ignored (e.g. Brodie et al. 2011 for the case of M87 companions).

UCDs are believed to be the bright and massive tail of the globular cluster luminosity function (Drinkwater et al. 2000) or the nuclei of stripped dwarf galaxies (Bekki et al. 2003). A combination of both formation mechanisms has also been proposed (Da Rocha et al. 2011). The large magnitude gap between UCD1 and the brightest globular clusters of NGC 1132 suggests that UCD1 is the leftover core of a spiral galaxy (Bekki et al. 2001). The other UCDs can be stripped dE nuclei or massive globular clusters. The analysis of a large sample of spectroscopic properties of UCDs would prove a link between their stellar populations and those of dwarf galaxies and/or globular clusters.

5

The Size Scale of Star Clusters

5.1 Numerical Simulations with NBODY6

Numerical simulations use theoretical models to reproduce a particular system of interest. Computer models with complex codes are generally aimed at simulating a stage of a system that it is not readily observable or costly to reproduce. In finance, for instance, computer models based on present and past data strive to simulate future share prices. Likewise, in aeronautics, computer simulations are used to test prototypes of airplanes. For the Boeing 767 the manufacturer tested 77 wing prototypes in a wind tunnel while for the Boeing 787 the company tested only 11. The remaining testing of prototypes was carried out using computer simulations in supercomputers (Lamb 2012).

In a similar way, the intention when running numerical simulations of stellar systems is to reproduce evolutionary stages not accessible with direct observations. Numerical simulations are a window to the past and future of stellar systems but also a tool to explore sections of the parameter space where observations, for one reason or another, do not reach. In particular, we can explore different evolution scenarios that reach the current state of star clusters.

Numerical simulations provide unique information on the past evolution of compact stellar systems. In fact, the properties of such systems obtained with present day observations are set during an entire Hubble time of evolution. Numerical simulations can give a detailed picture of many different physical parameters at different steps of their time evolution. For instance, a globular cluster with a present mass of $10^4 M_\odot$ most likely had an initial mass of $10^6 M_\odot$ or higher (Böker 2008). When carrying out numerical simulations of globular clusters, mass-loss rates over a Hubble time are readily obtained. Numerical simulations allow us to test how different physical processes work together or against each other to shape the size and mass distribution of compact stellar systems that we

see today. Necessarily the focus is on models of star clusters and extended star clusters, owing to the computational constraints with the direct N-body method as described in the Introduction. However, scaling of results to higher-mass collisional systems is also possible.

5.2 NBODY6

Numerical simulations carried out for this thesis were executed with `NBODY6`. `NBODY6` is one of the most recent versions of a N-body code that begun as `NBODY1` in the early 60's (Aarseth 1999). The different versions of `NBODY` have been developed over more than half a century, continuously improving with contributions by a large number of scientists but always chaired by Sverre J. Aarseth at Cambridge University. This extensive development has lead to a detailed and robust code that accurately describes the evolution of star clusters. A brief and simple presentation of selected key improvements of the code during the last 50 years is given below. A detailed account of the development of `NBODY6` has been presented in two books *Gravitational N-Body Simulations* (Aarseth 2003) and *The Cambridge N-Body Lectures* (Aarseth et al. 2008).

5.2.1 Hermite Integration Scheme

The most basic aim of an N-body code that simulates a star cluster is to predict the trajectories of its different stars, given some initial conditions. The earliest N-body codes only considered the effect of the gravitational force between stars. The equations of motion for a system composed of two bodies with masses m_1 and m_2 and subject to the gravitational force, as below,

$$F = G\frac{m_1 \times m_2}{r^2} \tag{5.1}$$

have an analytical solution. There is, however, no analytical solution for systems composed of three bodies or more that are subject to the gravitational force. The use of numerical solutions is thus needed in order to solve the equations of motion of systems with more than three bodies such as star clusters.

The Hermite integration scheme takes advantage of the fact that the expression of the force and its first derivative are straightforward and fast to compute. Both the force and its first derivative can be expanded as Taylor series to yield:

$$\mathbf{F} = \mathbf{F_0} + \mathbf{F}_0^{(1)}t + \frac{1}{2}\mathbf{F}_0^{(2)}t^2 + \frac{1}{6}\mathbf{F}_0^{(3)}t^3 \tag{5.2}$$

and

$$\mathbf{F}^{(1)} = \mathbf{F}_0^{(1)} + \mathbf{F}_0^{(2)} t + \frac{1}{2}\mathbf{F}_0^{(3)} t^2 \,. \tag{5.3}$$

The second and third derivatives correctors, $\mathbf{F}_0^{(2)}$ and $\mathbf{F}_0^{(3)}$, can be obtained as a function of $\mathbf{F}$, $\mathbf{F}^1$, $\mathbf{F}_0$, and $\mathbf{F}_0^{(1)}$. At each time step the code calculates the coordinates and velocities of all particles to first order and then applies a corrector based on the expression of $\mathbf{F}_0^{(2)}$ and $\mathbf{F}_0^{(3)}$. The Hermite integration scheme is similar in nature to the Runge-Kutta, or leap-frog methods.

5.2.2 Ahmad-Cohen Scheme

With the aim of speeding up the computation of the gravitational force between the large number of stars that constitutes a star cluster, the Ahmad-Cohen neighbor scheme splits the gravitational force of each particle into two components based on distance. One component relates to the gravitational force of nearby particles and a second component relates to more distance stars. This is traditionally written as

$$\mathbf{F} = \mathbf{F}_I + \mathbf{F}_R \tag{5.4}$$

where $\mathbf{F}_I$ is the *irregular* force pertaining to the closest neighbors and $\mathbf{F}_R$ is the *regular* force of more distant particles. Obviously, the dominant component of the force is the *irregular* part. By separating the force in two components `NBODY6` updates its dominant component more often that the secondary one thus saving computational time (Aarseth 2003). The input file for `NBODY6`, presented in Appendix A, sets the number of close neighbors through the variable `NNBMAX`. The numerical value for the simulations presented in this work is `NNBMAX= 400`.

5.2.3 The "Fatal Attraction" of Gravitation

An important development of the `NBODY6` code has been the treatment of close encounters without involving any softening. The gravitational attraction between two bodies tend towards a singularity when these two bodies come too close together:

$$\frac{1}{r^2 \to 0} \to \infty. \tag{5.5}$$

Historically, this singularity was treated with softening, that is, an extra term ϵ in the equation of the gravitational potential that allows an exemption from the singularity when $r \to 0$:

$$\Phi = -\frac{1}{r+\epsilon}. \tag{5.6}$$

A more sophisticated workaround of this singularity is a change of basis for coordinates and time. Consider a particle in a two dimensional complex plane that has coordinates ($\mathbf{x} = x_1, ix_2$). Assuming that this vector $\mathbf{x}$ can be represented by the square of another complex vector, that is $\mathbf{x}= \mathbf{u}^2 = (u_1, iu_2)$ the following change of basis can be made

$$\begin{pmatrix} x_1 \\ x_2 \end{pmatrix} = \begin{pmatrix} u_1 & -u_2 \\ u_2 & u_1 \end{pmatrix} \begin{pmatrix} u_1 \\ u_2 \end{pmatrix} \tag{5.7}$$

and the components of $\mathbf{x}$ can be written as $x_1 = u_1^2 - u_2^2$ and $x_2 = 2u_1 \times u_2$. The change of basis above is known as the Levi-Civita transformation (Levi-Civita 1920). Once the change of basis is made the Hamiltonian is solved in the new basis and the the results are back-transformed to the original coordinates. The Levi-Civita matrix above is for a particle in a two dimensional plane. In `NBODY6` star-particles evolve in a three dimensional space. Coordinates are thus transformed with a Kustaanheimo-Stiefel matrix that generalizes the properties of the Levi-Civita transformation to 3D (Kustaanheimo & Stiefel 1965). As a result of this change of basis close encounters beween stars can evolve smoothly and singularity free.

5.2.4 Stellar Evolution

`NBODY6` also incorporates a detailed prescription of stellar evolution (Hurley, Pols & Tout 2000) . This contribution gives the code a greater relevance in astrophysics since stellar evolution has such an important role in the dynamical evolution of a star cluster. Approximating stars as point masses over a Hubble time is an oversimplification. In `NBODY6` stars have appropriate dimensions that take into account the evolutionary stage of their atmosphere. The evolution of stellar mass as a function of time is also computed. This is of particular relevance for the dynamics of star clusters given that mass loss owing to stellar evolution affects the gravitational potential well of the entire cluster.

The stellar evolution of Hurley et al. (2000) is based on the detailed stellar models of Pols et al. (1998) which include the possibility to allow moderate convective overshooting. Ideally the N-body approach would have the flexibility to use alternative and more up-to-date stellar models. The inclusion of new stellar evolution has been attempted (Church et al. 2009) but the results of Hurley et al. (2000) remain valid. We do not expect mass loss rates of AGB or RGB stars to be dramatically different from those we know today. Thus

the results obtained with the prescriptions of Hurley et al. (2000) remain accurate.

Instead of running a parallel stellar evolution code, NBODY6 obtains the properties of each star (i.e. evolutionary stage, mass) from a set of analytical functions fully incorporated within the code. This set-up is a major advantage for both computing time and the robustness of the code. The stellar evolution sections of the code yield stellar luminosities that can be readily used for direct comparison with observations (Hurley et al. 2005).

An important component of stellar evolution is a detailed and realistic treatment of stellar binaries. In NBODY6, as in reality, the two components of a binary system have joint dynamical evolution. Orbits of binary stars are subject to tidal interactions that tends to make eccentric orbits become circular. Binary stars also can have mass transfers from one star to their companion or even evolve in what is known as a common envelope, that is when an expanded atmosphere from one star expands beyond the orbit of the other binary member. The binary treatment used in NBODY6 has been published by Hurley, Tout, and Pols (2002). This code also includes a detailed handling of the formation of three and four body systems (Tout 2008; Hurley 2008; Mardling 2008; Mikkola 2008).

5.3 The Size Scale of Star Clusters

Why is the size distribution of star clusters narrowly centered around three parsecs? Why do only a few clusters become extended with effective radii of ten parsecs or more? In this work, advanced N-body models are carried out with the aim of determining the most important physical mechanisms that mold the characteristic radii of star clusters. The impact of the host galaxy tidal field on the size of orbiting star clusters is probed in detail by evolving several models at different galactocentric distances (R_{GC}).

The empirical qualitative dependence between size and galactocentric distance of star clusters has been clearly established in several observational studies beginning with the work of Hodge (1960, 1962). The N-body models that have been performed allow us to quantify the influence of the tidal field, generated by a Milky-Way or M31-type galaxy, on satellite star clusters. We thus determine a new relation between the scale sizes of star clusters and galactocentric distance. This relation is a proxy for the host galaxy gravitational potential.

All N-body simulations are performed using the NBODY6 code presented above (Aarseth 1999; Aarseth 2003). As mentioned above, this code performs a direct integration of the equations of motion for all N stars and binaries in a star cluster and includes a comprehensive treatment of stellar evolution (Hurley et al. 2000, 2005). The version of

NBODY6 that is used in this work was modified to run on a GPU (Nitadori & Aarseth 2012). During the last decade the clock rates of Central Processing Units (CPUs) have been practically stagnant while GPUs provide a proven alternative for high-performance computing (Barsdell et al. 2010), and particularly for N-body codes (Hamada et al. 2009). The models are run at the Center for Astrophysics and Supercomputing of Swinburne University. The GPUs in use are NVIDIA Tesla S1070 cards. Earlier versions of this code (i.e. NBODY4) were run on special-purpose GRAPE hardware (Makino et al. 2003) but the performance of the GPU version of this code is comparable or superior to previous efforts to improve computing time. The calculations are carried out in N-body units, i.e. $G = 1$ and $-4E_0 = 1$, where E_0 is the initial energy (Heggie & Mathieu 1986). The results are scaled back to physical units once the computation of the models is complete.

5.3.1 Numerical Simulations Set Up

The initial set up for the simulations carried out here is similar to the work of Hurley & Mackey (2010). All simulations have an initial number of particles of $N = 10^5$. Of these, 5% are primordial binary systems, that is, 95 000 single stars and 5 000 binary systems. The most massive star has a mass of $M_{max} = 50M_{\odot}$ while the minimum mass for a star is $M_{min} = 0.1M_{\odot}$. The initial mass distribution for all stars follows the stellar Initial Mass Function (IMF) of Kroupa et al. (2001). The models start off with a total initial mass of $M_{tot} \approx 6.3 \times 10^4 M_{\odot}$. The $N = 10^5$ stellar systems have the initial spatial distribution of a Plummer sphere (Plummer 1911) and an initial velocity distribution that assumes virial equilibrium.

It is noted that the Plummer sphere initial distribution can be rapidly erased through the dynamical evolution of the cluster and that the light profiles of young clusters can be fitted by a variety of methods (e.g. King 1966). Star clusters also tend to reach virial equilibrium from different precursor virial ratios (Hurley & Bekki 2008). The modeled clusters stars have a metallicity of $Z = 0.001$ or $[Fe/H] \approx -1.3$.

These simulations start after the clusters will have undergone expansion as the result of the removal of residual gas left over from star formation. Thus, at $t = 0$ all stars are assumed to have formed and be on the zero age main sequence, with no gas present. The initial three-dimensional half-mass radius is 6.2 pc.

The initial set up for each simulation is exactly the same with the exception of the initial galactocentric distance. Individual simulations of star clusters evolving on circular orbits at different galactocentric distances were obtained, i.e. R_{GC} = 4, 6, 8, 8.5, 10, 20, 50 and 100 kpc. The initial plane of motion of the star clusters is 22.5 degrees from the

plane defined by the disk. The motivation for an inclination of (90/4)=22.5 degrees is to have an orbit that is non planar but not perpendicular to the disk either. The maximum height has the same order of magnitude as the height of the thick disk.

5.3.2 Galactic Tidal Field Model

Earlier models from N-body simulations have made the simplifying assumption that the gravitational potential of the host galaxy can be represented by a central point mass only (e.g. Vesperini & Heggie 1997; Baumgardt 2001; Hurley & Bekki 2008). The version of `NBODY6` used here models the bulge as a point source but also includes a halo and a disk as components of the Milky-Way galaxy and its gravitational potential. This more realistic implementation of the host galaxy potential has been incorporated in recent work (e.g. Küpper et al. 2011).

To model the disk `NBODY6` follows Miyamoto & Nagai (1975) whom combined the potential of a spherical system (Plummer 1911) and the potential of a disk-like mass distribution (Toomre 1963) into a generalized analytical function that elegantly describes the disk of a spiral galaxy:

$$\Phi(r,z) = \frac{GM}{\sqrt{r^2 + [a + \sqrt{(z^2 + b^2)}]^2}}. \tag{5.8}$$

Here a is the disk scale length, b is the disk scale height, G is the gravitational constant, and M is the mass of the disk component. The elegance of this formulation resides in the fact that it can model both an infinitely thin disk or a sphere by varying the two scale factors a and b. The values used here are $a = 4$ kpc for the disk scale length, and $b = 0.5$ kpc for the vertical length (Read et al. 2006). Formally, the Miyamoto & Nagai disk extends to infinity. However, the strength of the disk potential asymptotes towards zero at large radii: with $a = 4$ kpc and $b = 0.5$ kpc, the density at 40 kpc drops to 0.1% of the central value.

The masses of the bulge and disk are $1.5 \times 10^{10} M_{\odot}$ and $5 \times 10^{10} M_{\odot}$, respectively (Xue et al. 2008). The galactic halo is modeled by a logarithmic potential. When combined together, the potential of the halo, disk, and bulge are constrained to give a rotational velocity of 220 km/s at 8.5 kpc from the galactic center (Aarseth 2003) giving a halo mass of $10^{11} M_{\odot}$. A detailed discussion of the galactic tidal field model is given by Praagman et al. (2010).

A tidal radius for a star cluster in a circular orbit about a point-mass galaxy, initially postulated by von Hoerner (1957), can be approximated by the King (1962) formulation:

$$r_{\rm t} = \left(\frac{M_{\rm C}}{3M_{\rm G}}\right)^{1/3} R_{\rm GC} \tag{5.9}$$

where $M_{\rm C}$ is the mass of the cluster, and $M_{\rm G}$ is the mass of the galaxy. The equivalent expression for a circular orbit in the Milky-Way potential described above is:

$$r_{\rm t} \simeq \left(\frac{GM_{\rm C}}{2\Omega^2}\right)^{1/3} \tag{5.10}$$

where Ω is the angular velocity of the cluster (Küpper et al. 2010a). The tidal radius is where a star will feel an equal gravitational pull towards the cluster and towards the galaxy center in the opposite direction. A detailed study of the tidal radius of a star cluster for different galaxy potentials is given by Renaud et al. (2011).

In the N-body code the gravitational forces owing to *both* the cluster stars and the galaxy potential are taken into account for all stars in the simulation, independently of the definition of the tidal radius. However it is common practice to define an escape radius, beyond which stars are deemed to be no longer significant in terms of the cluster potential and thus have no further input on the cluster evolution. Stars are removed from the simulation when they fulfil two conditions: (i) their distance from the cluster center exceeds the escape radius, and (ii) they have positive energy when the external field contribution is taken into account.

In our simulations we have estimated the escape radius as twice the tidal radius given by Eq. (5.8) with $M_G = 1.65 \times 10^{11} M_\odot$. At all times this gives a value in excess of the tidal radius given by Eq. (5.10). When presenting results, we only consider stars that lie within the tidal radius given by Eq. (5.10).

5.4 Previous Work

A pioneering study of this subject was carried out by Vesperini & Heggie (1997) who investigated the effects of dynamical evolution on the mass function of globular clusters through simulations based on `NBODY4`. This was the most up-to-date version of the code at the time of their work and only included a basic treatment of stellar evolution. Also, the total number of particles that Vesperini & Heggie (1997) were able to simulate was limited to $N = 4\,096$ owing to restrictions imposed by the hardware. Under the conditions used here a simulated cluster with only $N = 4096$ orbiting at R_{GC}= 8 kpc is dissolved in 1.1 Gyr. Despite the computational limitations to which Vesperini & Heggie (1997) were subject, they set an inspiring precedent for this work. Particularly relevant is the trend

of increasing mass-loss with decreasing galactocentric distance, albeit with the galaxy potential modeled as a point-mass.

Baumgardt & Makino (2003) studied the stellar mass function of star clusters using NBODY4 but with more realistic particle numbers, going up to $N = 131\,072$. They determined that stellar evolution accounts for $\sim 1/3$ of the total mass lost by the cluster. The upper mass limit of the stellar initial mass function used by Baumgardt & Makino (2003) was $M_{max} = 15M_{\odot}$, while in the simulations presented here $M_{max} = 50M_{\odot}$. With our set-up, having an upper mass limit of $50M_{\odot}$ implies that 240 stars (2% of the total) will have a mass between 15 and $50M_{\odot}$; their combined total mass is $\sim 10\%$ of the initial mass. Baumgardt & Makino (2003) found that owing to mass segregation low-mass stars are prone to be depleted from the star cluster. This depletion of low mass stars inverts the slope of the IMF. Unlike Baumgardt & Makino (2003) the models presented here include a population of 5000 primordial binary systems. For the original spatial distribution Baumgardt & Makino (2003) used a King profile while here a Plummer sphere is used.

5.5 Total Mass

NBODY6 readily yields fundamental numerical parameters of the simulated star clusters such as the number of stars, number of binaries, total mass, core mass, half-mass radius, relaxation time, and velocity dispersion, to name a few.

Star clusters evolving in a galactic potential lose mass due to stellar evolution, two body relaxation, few-body encounters, and tidal interactions with the host galaxy. In the following sections the two main phases of mass-loss are discussed.

5.5.1 Initial Stellar Evolution

During the first Gyr of evolution star clusters lose large amounts of mass owing to stellar evolution. Massive stars with $M \sim 10M_{\odot}$ and above such as OB stars, luminous blue variables, and Wolf-Rayet stars have large mass-loss rates of the order of $\dot{M} \sim 10^{-5}M_{\odot}$ per year (Vanbeveren et al. 1998; Shara et al. 2009). The mass loss rates of these stars is the dominant factor of their evolution. In fact, mass-loss determines whether a massive star becomes a supernovae or a long duration gamma-ray bust (Vink et al. 2000, Shara et al. 2009). Massive stars are short lived, for instance Wolf-Rayet stars with initial masses greater than $20M_{\odot}$ are expected to survive only 10 Myr (Hurley et al. 2000).

The N-body simulations plotted in Figure 5.1 show that star clusters, independently of galactocentric distance, lose $\sim 1/3$ of their mass during the first Gyr of evolution. This

is in agreement with the findings of Baumgardt & Makino (2003). The stellar evolution of massive stars discussed above is responsible for the mass loss that triggers an expansion of the cluster due to a reduced gravitational pull. The impact of mass loss on the scale size of a star cluster is discussed in the next section.

5.5.2 Two Phases of Mass-loss

The two main regimes of mass loss evident in these simulations are mass loss from stellar evolution and mass loss due to tidal stripping. The former initially increases the cluster size, while the latter decreases the cluster size. Whether or not either of the two mechanisms dominates will determine the size of the star cluster (Gieles et al. 2011).

As mentioned above, stellar evolution mass-loss occurs on a rapid timescale at early times. It subsequently slows owing to the longer evolution timescales of low-mass stars but maintains a steady presence throughout the ongoing life of a cluster. Mass-loss resulting from tidal stripping is linked to the two-body relaxation timescale of the cluster: two-body interactions gradually increase the velocities of the low-mass stars, pushing them to the outer regions where they are lost across the tidal boundary in a process that is often called evaporation (McLaughlin & Fall 2008). For star clusters evolving at small galactocentric distances (e.g. simulations at 4 and 6 kpc) the dominant mechanism of mass loss is tidal stripping. These clusters have relatively short two-body relaxation timescales. In contrast, for clusters evolving at large galactocentric distances (with longer relaxation timescales) the dominant mass loss mechanism is stellar evolution. It is clear from Figure 5.1 that the closer a star cluster orbits to the center of the galaxy, the more accentuated its mass loss is. Figure 5.1 shows how the mass-loss rate evolves towards an asymptotic linear behavior after a Hubble time, in agreement with Baumgardt & Makino (2003). Few-body interactions can also lead to the loss of stars through ejections. This process can cause small-scale fluctuations in cluster size on short timescales.

5.6 Characteristic Radii

Different characteristic radii are commonly used for star clusters. Observers obtain two dimensional half-light radii to high accuracy, but are limited in their choice of characteristic radii. For simulated clusters, different scale size values are readily available such as the half-mass radius, r_{hm}, or core radius. Radii of simulated clusters can be expressed in two or three dimensions, the latter is adopted in this work. Hurley & Mackey (2010) show that the value of the half-*mass* radius derived with `NBODY6` is on average 1.6 times the value of

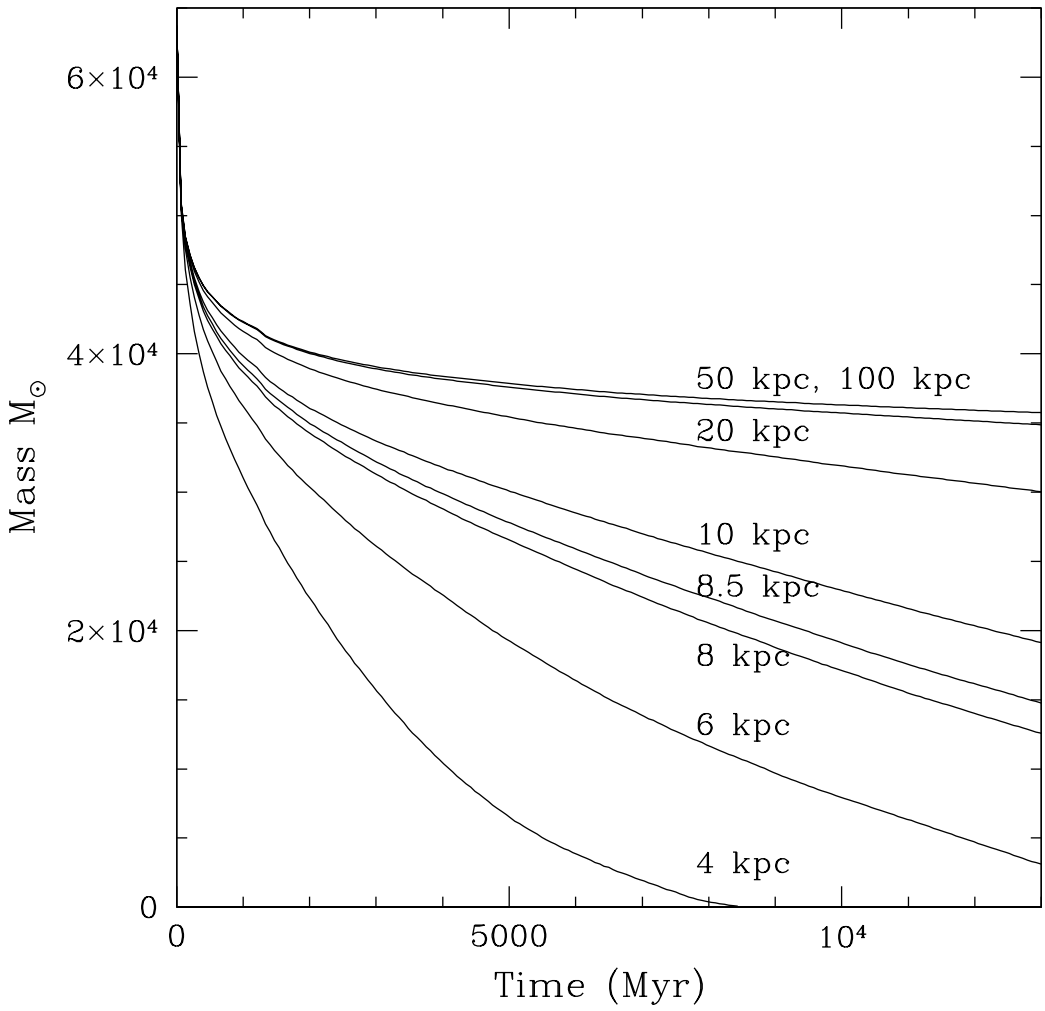

Figure 5.1 Mass loss of simulated star clusters at different galactocentric distances. Note how the simulated star cluster evolving at 4 kpc has lost all of its mass after 8.4 Gyr.

an observed half-*light* radius. Moreover, different characteristic radii describing the core of star clusters are known to evolve in a self-similar fashion (Baumgardt et al. 2004).

The definition of core radius is different in observational and theoretical studies. In observational studies the core radius is generally defined as the radius where the surface brightness falls to half its central value (King 1962). In our simulations, the core radius is a density-weighted average distance of each star to the point of highest stellar density within the cluster (Aarseth 2003). We should note that the core radius is not expected to correlate with the half-mass radius.

5.6.1 Observed and Primordial Half-Mass Radius

The evolution of the half-mass radius of the simulated star clusters with time is plotted in Figure 5.2. Clusters start with an initial half-mass radius of ~ 6.2 pc and undergo an expansion triggered by stellar evolution within the first Gyr as discussed above. An initial half-mass radius of ~ 6.2 pc might seem larger than average but after a Hubble time of evolution King (1962) models fitted to the light profiles of our models yield two dimensional half-light radii that are consistent with observations, i.e. around 3 pc (Sippel et al. 2012).

In their original work, Spitzer & Thuan (1972) found that the effective radius of an isolated star cluster remains constant through several relaxation times. Their important result is confirmed in Figure 5.2 but only for the model evolving at 20 kpc from the galactic center. In this particular model the star cluster experiences only weak tidal interactions with the host galaxy. After the initial phase of rapid expansion driven by stellar evolution, the longer-term steady expansion driven by the internal dynamics is balanced by the presence of the tidal field. Thus, the half-mass radius of this simulated star cluster remains constant over the last eight Gyr of evolution in agreement with Spitzer & Thuan (1972).

More importantly, the effective radii of all star clusters evolving at $R_{GC} < 20$ kpc are significantly affected by tidal interactions that truncate the cluster size during its evolution. The results of Spitzer & Thuan (1972) are often misquoted in observational studies as proof that the effective radius remains constant over many relaxation times and that the r_h measured today is a faithful tracer of the original size of the proto-cluster cloud.

As shown in Figure 5.2, the half-mass radii of simulated clusters evolving at 50 and 100 kpc are always increasing. For these two simulations, in virtual tidal isolation and with long relaxation times, their half-mass radii reach about twice the value of the initial

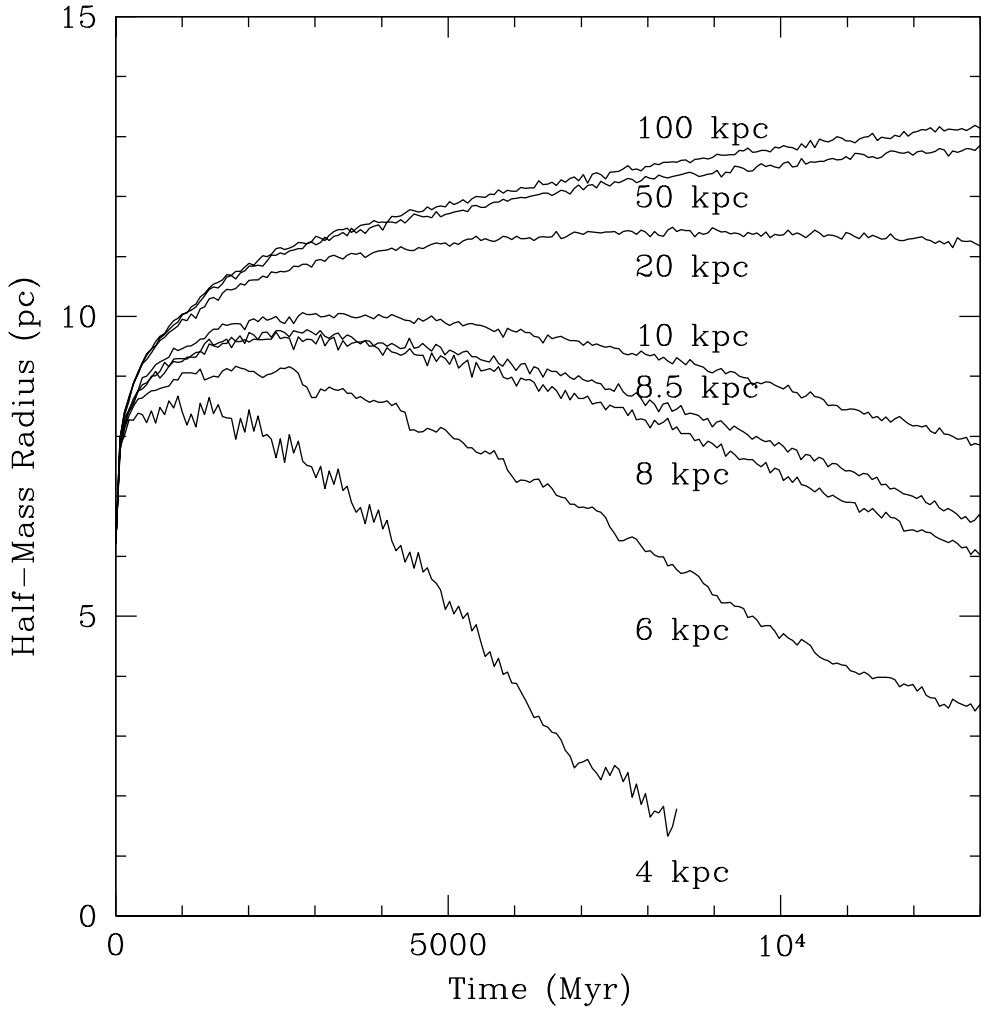

Figure 5.2 Evolution of the 3D half-mass radius of simulated star clusters at different galactocentric distances. A simulated star cluster evolving at 4 kpc from the galactic center dissolves before a Hubble time. Simulated star clusters orbiting the galaxy at less than 20 kpc experience a truncation of their half-mass radius due to tidal interactions. *Note: The wiggles in the results are due to statistical variations, running two simulations and averaging the results would have removed these wiggles. Given the large number of simulations we carry out running duplications would be a very onerous task.*

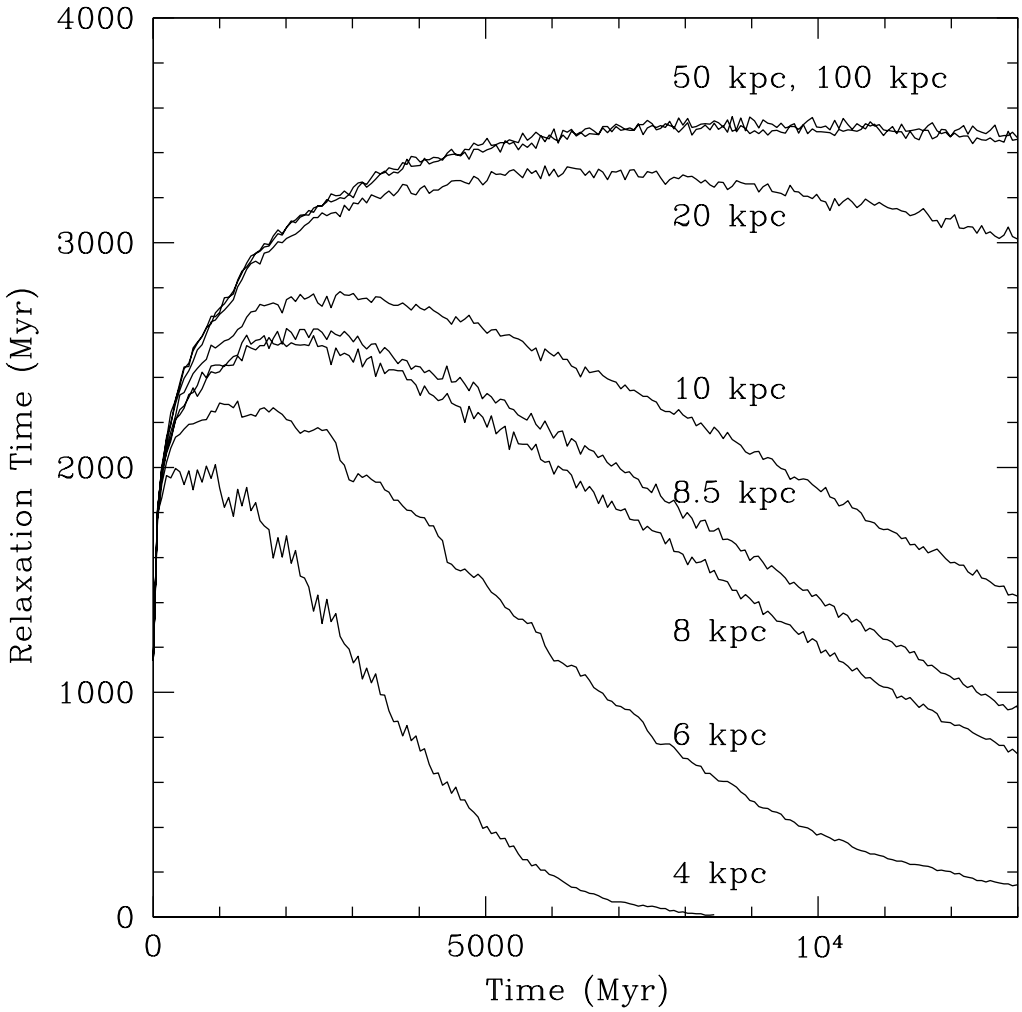

Figure 5.3 Evolution of the half-mass relaxation time vs. time for star clusters at different galactocentric radii. The relaxation time is a dynamical quantity determined by equation 5.11.

half-mass radius, i.e. $r_{hm}/r_{hm0} \approx 2$ after a Hubble time (Gieles et al. 2010).

Most observational studies of extragalactic star clusters aimed at determining their scale sizes are carried out with the *Hubble Space Telescope* due to its unique resolution (e.g. the ACS Virgo Cluster Survey by Jordán et al. 2005). The drawback of space-based detectors is the small field of view that only covers, in general, a physical scale of a few kiloparsecs in radius surrounding the core of the host galaxy. As shown in Figure 5.2 the inner ten kiloparsercs of a galaxy is where the tidal field has the strongest impact on the size of the satellite star cluster, with a dependence on galaxy mass. The effective radius of a star cluster evolving in a realistic galaxy potential loses any memory of its earlier values. As shown in Figure 5.2, only the simulated star cluster evolving at 20 kpc has an effective radius that remains constant through several relaxation times which is a result of its particular circumstances, being in a position within the galaxy where internally driven expansion is balanced by the external truncation of the tidal field. The exact position at which this occurs will be dependent on the strength of the tidal field, and thus the galaxy model, and on the initial mass of the star cluster.

In the simulations presented here a star cluster orbiting the Galactic center at 50 kpc or more is free from disk shocking, given that the disk has an extent of ∼40 kpc. Disk shocking has demonstrated wounding effects on cluster stability (Gnedin & Ostriker 1997; Vesperini & Heggie 1997). In an effort to quantify the effect of disk shocking a full simulation was carried out with a star cluster in an orbit at 10 kpc from the galactic center where the mass of the disk was placed in a central spheroid component instead of a disk. This showed that the presence of a disk will enhance the mass loss of the simulated cluster by $2.4{\times}10^3$ $M_\odot$ (13% of the total mass) over a Hubble time, and will make its half-mass radius smaller by 0.6 pc (10% of its size). Thus at 10 kpc from the galactic center the effect of the disk in a star cluster, while subtle, is clearly measurable. A detailed study of the impact of disk shocking on the evolution of star clusters is presented in the next chapter.

From the output of `NBODY6` we compute the half-mass relaxation time as:

$$t_{rh} = \frac{0.14N}{\ln \Lambda} \sqrt{\frac{r_{hm}^3}{GM}} \tag{5.11}$$

where N is the number of stars, r_{hm} the half-mass radius, and $\Lambda = 0.4N$ the argument of the Coulomb logarithm (Spitzer & Hart 1971; Binney & Tremaine 1987). Note that Giersz & Heggie (1994) found a value of $\Lambda = 0.11N$. The value of 0.4 is obtained by an integration of all impact parameters in two body encounters, whereas the value derived

by Giersz & Heggie (1994) was obtained through a numerical calculation (Aarseth 2003).

The evolution of the relaxation time for each star cluster is homologous to the evolution of the half-mass radius as shown in Figure 5.3. For all clusters it reaches a maximum value at the point when expansion driven by mass loss is equivalent to evaporation in the cluster (Gieles et al. 2011). The simulations carried out here show that this coincides with the half-mass radius reaching its maximum as well. The number of relaxation times reached by each simulation after a Hubble time is given in Table 5.1, for those simulations that survive this long. Accentuated mass loss of the simulated star clusters accelerates their dynamical evolution. For example, the simulated cluster evolving at $R_{GC} = 6$ kpc undergoes 90 relaxation times in 13 Gyr compared to only 3 for the simulated cluster at $R_{GC} = 100$ kpc.

5.6.2 Half-Mass Radius versus Galactocentric Distance at Present Time

Figure 5.4 shows the half-mass radius of simulated star clusters orbiting at different galactocentric distances after 13 Gyr of evolution. The values used to create Figure 5.4 can be found in Table 5.1. After a Hubble time of evolution the half-mass radius defines a relationship with galactocentric distance which takes the mathematical form of a hyperbolic tangent. This relation, plotted in Figure 5.4 as a solid line, is:

$$r_{hm} = r_{hm}^{max} \tanh(\alpha R_{GC}) \tag{5.12}$$

where r_{hm} is the half-mass radius and r_{hm}^{max} is the maximum half-mass radius attained by simulated clusters evolving at 50 and 100 kpc from the galactic center after a Hubble time (all radii in 3D). The maximum half-mass radius defines a plateau in the relationship between half-mass radius and galactocentric distance. Current relations defining the scale sizes of clusters as a function of galactocentric distance such as the empirical power-law $r_h = \sqrt{R_{GC}}$ (van den Bergh et al. 1991) do not include this flattening at large galactocentric distances. Note that the database used by van den Bergh et al. (1991) only included star clusters out to 32.8 kpc from the galactic center.

The parameter α is a positive coefficient that defines the inner slope, i.e. within the inner 20 kpc. In this case its numerical value is 0.06. The parameter α is a proxy of the tidal field of the host galaxy that is in turn due to galaxy mass. Note that the onset of the plateau of Figure 5.4 at $R_{GC} \simeq 40$ kpc coincides with the approximate extent of the disk in our models. While the disk might in theory extend to infinity its density asymptotes to zero at about 40 kpc from the galactic center. Beyond this distance globular clusters while remaining fully bound to the galaxy evolve in virtual isolation and are exempt from

the truncating effects of the host galaxy tidal field. Therefore star clusters at 40 kpc and beyond have their sizes determined primarily by their internal dynamics (Spitzer & Thuan 1972) and also to some extent by their initial size. Hurley & Mackey (2010) showed that for clusters in a weak tidal field, differences in initial size can lead to long-term differences in half-mass radius, although the effect diminishes with age. Initial sizes of clusters are uncertain with some suggestions that the typical size-scale of a protocluster is $\sim 1\,\mathrm{pc}$ (Harris et al. 2010) but the actual size after gas removal (when the N-body simulations start) will depend on the star formation efficiency within the protocluster (Baumgardt & Kroupa 2007; Bastian & Goodwin 2006; Goodwin & Bastian 2006). Thus it should be noted that the initial size of the cluster will have some bearing on the location of the plateau, i.e. $r_{\rm hm}^{\rm max}$.

5.6.3 Scaling of the Simulations

A set of simulations with a different initial mass were executed in order to establish a scaling relation that is independent of mass and independent of the initial number of particles N. The aim is to allow us to make inferences towards more massive systems. Three full simulations, all of them with identical initial conditions but with different initial number of particles and thus different initial masses were carried out at a galactocentric distance of $R_{GC} = 8$ kpc. These three simulations have initial masses of $M = 6.3\times10^4 M_\odot$, $M = 4.9 \times 10^4 M_\odot$, and $M = 3.2 \times 10^4 M_\odot$ with initial particle numbers of N=100 000, 75 000, and 50 000 respectively. A unit-free relation that is interchangeable for these three simulations with different initial masses is M/M_0 vs. t/t_{rh}, where M_0 is the initial cluster mass and t_{rh} is the half-mass relaxation time (see also Baumgardt 2001).

The relation between M/M_0 vs. t/t_{rh} allows us to derive a predicted value of the half-mass radii after a Hubble time of evolution for simulations with twice the number of initial particles (i.e. N= 200 000) as described below. More massive clusters have longer relaxation times t_{rh} (Spitzer 1987). In fact, at any particular time, a star cluster with N= 200 000 has a t/t_{rh} smaller by a factor of 3/4 than the t/t_{rh} of a star cluster with half the number of particles. We predict that after a Hubble time of evolution, the half-mass radii of clusters with N=200 000 are equivalent to the half-mass radii of the simulations carried out here but at an earlier stage of their evolution. For instance, a simulated star cluster evolving at $R_{GC} = 8$ kpc with an initial number of particles N=100 000, undergoes 18 relaxation times after a Hubble time. The simulated cluster with the same characteristics but with an initial number of particles N=200 000 undergoes 13.5 relaxation times after a Hubble time of evolution. The half-mass radius, at a Hubble time, for the

latter cluster is equivalent to the half-mass radius of the simulated star cluster with half the initial number of particles but only after 13.5 relaxation times. The predicted values of half-mass radii for models starting with N=200 000 are plotted in Figure 5.4 as blue stars. As this shows, the relation of half-mass radius vs. galactocentric distance postulated above (Eq. 5.12) holds true for models with higher masses. The simulations with different N were used to test the validity of the scaling outlined above.

5.6.4 Comparison With Observations

Hwang et al. (2011) derived the two-dimensional half-light radii of star clusters and extended star clusters in the halo of the dwarf galaxy NGC 6822. The main body of this dwarf galaxy has a scale length of 2.3 kpc (Billett et al. 2002). The shape of the distribution of the effective radii of globular clusters from the center of NGC 6822 is strikingly similar to the half-mass radius vs. galactocentric distance relation shown in Figure 5.4. The distance at which the relation between half-light radius and galactocentric distance starts to plateau is about 4.5 kpc for NGC 6822.

In dwarf galaxies this r_{hm}^{max} can be observed due to the smaller scales involved that can fit within the field of view of HST detectors.

The coincidence between Fig. 5.4 and the results of Hwang et al. (2011) shown in Figure 5.5 is encouraging, however, no information is available on the orbits of these clusters. A set of models taking into account the characteristics of NGC 6822 will be needed before definite conclusions regarding the spatial distribution of the size of star clusters can be made.

5.6.5 Comparison With The Milky Way

Figure 5.6 shows the observational data (Mackey & van den Bergh 2005; Harris 1996) of half-light radii of Milky Way globular clusters as a function of galactocentric distance. The solid line on Figure 5.6 is a function of the form of Eq. 5.12 where r_h^{max} is 20 pc, and $\alpha = 0.03$. The hyperbolic tangent function derived to describe the behavior of the half-mass radii as a function of galactocentric distance provides also a good description for the half-light radii derived observationally.

The empirical power law $r_h = \sqrt{R_{GC}}$ (van den Bergh et al. 1991), marked in Figure 5.6 by a dotted line, does not describe the plateau in half-light radii reached by Galactic clusters at $\sim$ 40 kpc. Mackey & van den Bergh (2005) postulate that Galactic clusters with $R_{GC} > 15$ kpc evolve free from tidal interactions. Using the simulations presented above jointly with the observational data, we find that the galactocentric distance at which

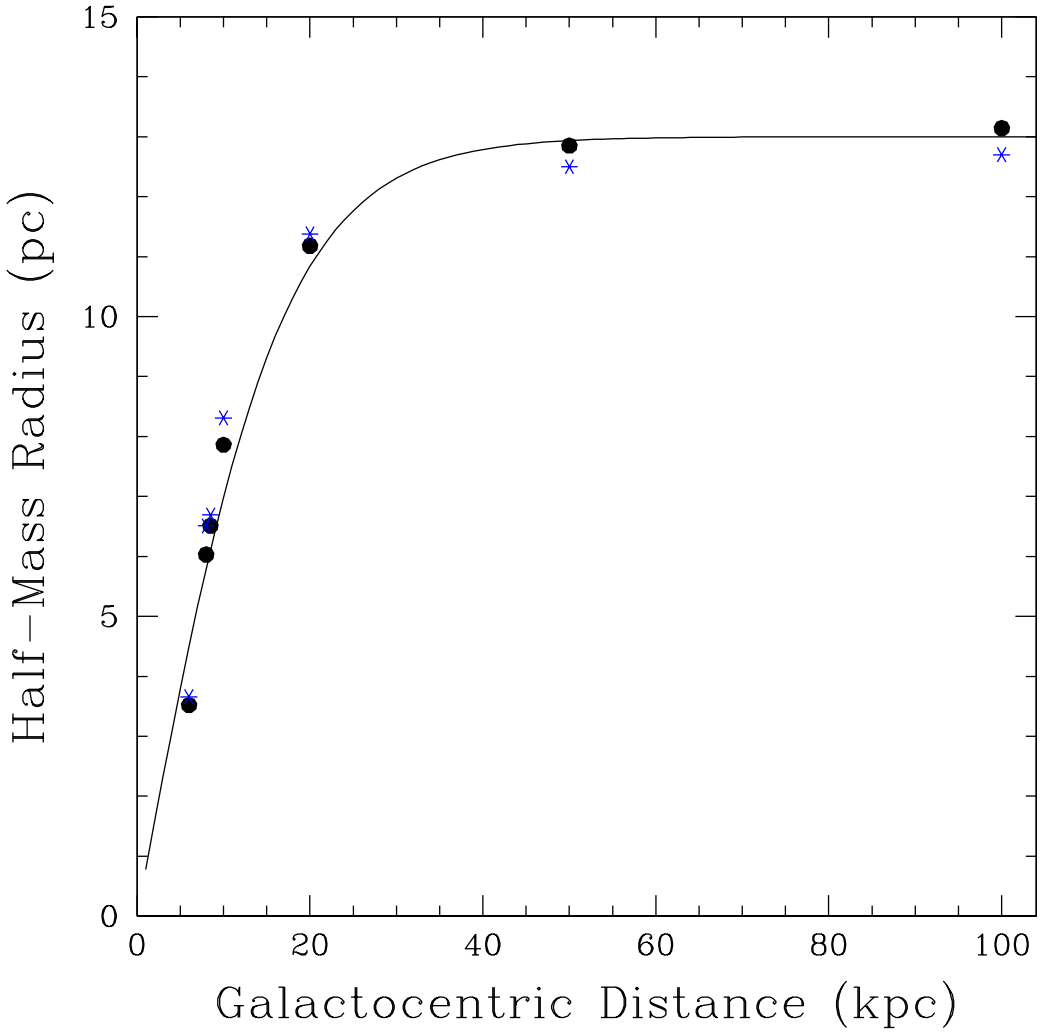

Figure 5.4 3D half-mass radius vs. galactocentric distance of simulated star clusters. Black dots give the half-mass radius of models at 13 Gyr. The solid line is simply a hyperbolic tangent describing a new relation between half-mass vs. galactocentric distance. Blue stars depict the predicted value of the half-mass radius after a Hubble time for simulations with twice the initial number of particles and twice the initial mass.

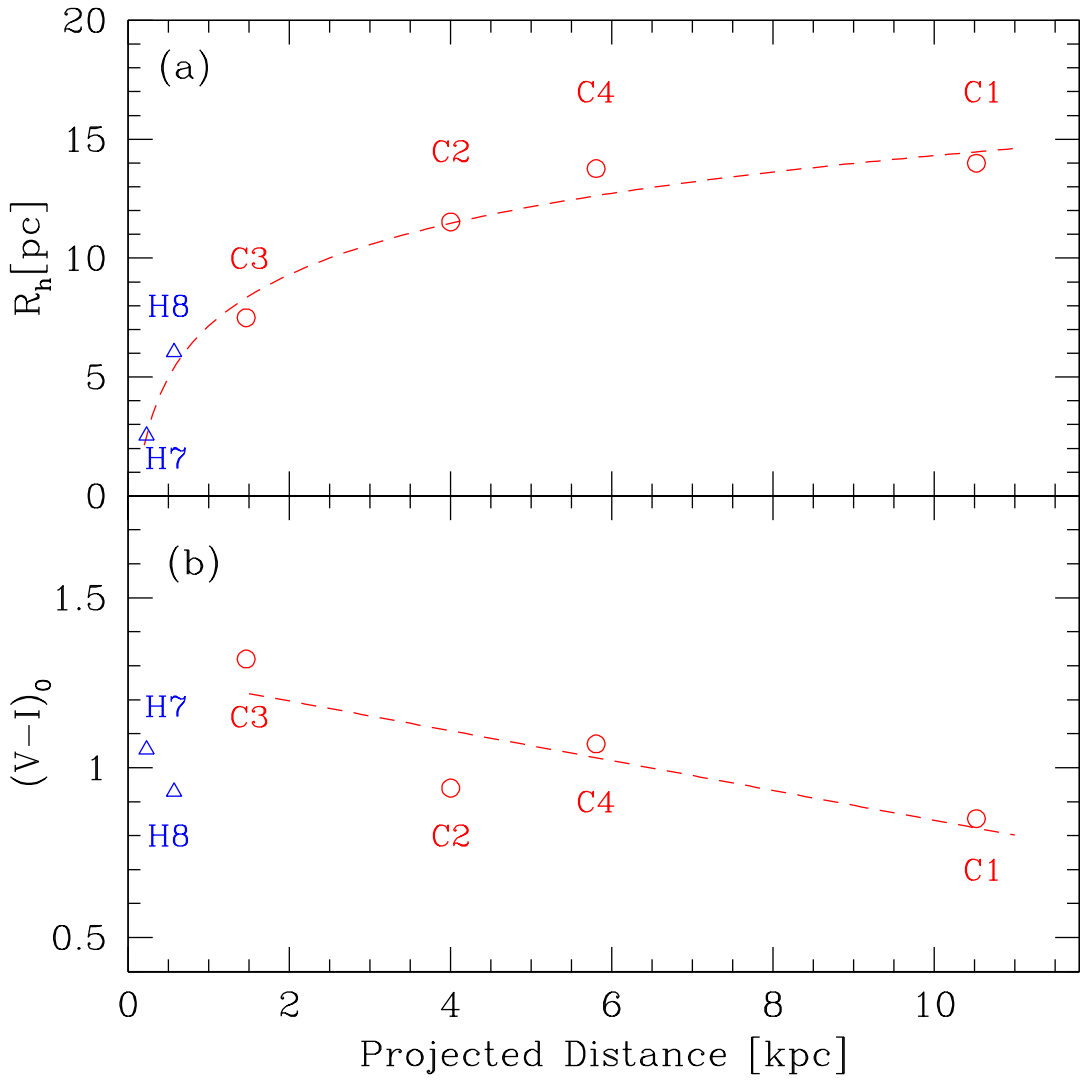

Figure 5.5 The top panel shows the half-light radii of star clusters vs. projected galactocentric distance to the center of NGC 6822. The bottom panel shows the color distribution of these clusters versus galactocentric distance. The dashed line of the top panel is a fit to the half-light radii of the stars clusters done by Hwang et al. (2011). The similarity of this fit with the formula derived in this chapter and shown in Figure 5.4 is clear. This figure was kindly provided by Narae Hwang and is reproduced with permission of the author.

clusters evolve free from tidal interactions is $R_{GC} \simeq 40$ kpc. This distance is shown as a dotted line in Figure 5.6.

In Figure 5.6, however, the scatter of observed half-light radius is evident. This scatter can be explained by non-circular orbits with different ellipticities and a spread in the original cluster sizes. We show below that a non circular orbit has an impact on the size of the star cluster. It is also natural to believe that the original distribution of size and mass of star clusters has an intrinsic spread that translates as a scatter in observed half-light radii of Figure 5.6.

5.6.6 Core Radius

The galactocentric distance of a star cluster also has an impact on its core radius, the onset of core collapse, and thus the ratio of core to half-mass radius. Figure 5.7 shows the evolution of the ratio of core to half-mass radius over 15 Gyr for simulations at a galactocentric distance of 4, 6, 10 and 100 kpc. Only selected simulations are plotted to preserve the clarity of the figure. The ratio r_c/r_{hm} has been used in various ways to characterize the dynamical state of globular clusters, including as a possible indicator of the presence of an intermediate-mass black hole (see Hurley 2007 for a discussion).

The core radius, not directly depicted here, expands rapidly within the first 2 Gyr from ~ 2.6 pc to ~ 4.1 pc. While the expansion of the core is similar at different galactocentric distances, the core to half-mass radius ratio is different for simulations evolving within and beyond the inner 10 kpc of the galaxy. For simulations at 4 and 6 kpc the ratio r_c/r_{hm} increases significantly during the initial 5 Gyr of evolution. Accentuated mass loss at small galactocentric distances also precipitates the onset of core collapse as seen in Figure 5.7. Core collapse is reached at ~ 7 Gyr for a star cluster at 4 kpc from the galactic center, just prior to dissolution, while core collapse is reached at 11 Gyr for a cluster at 6 kpc. Figure 5.7 shows that clusters in orbits of 10 and 100 kpc do not reach the end of the core collapse phase in a Hubble time. This will continue to be true for more massive clusters as the relaxation time will be even larger.

5.6.7 The Impact of Orbital Ellipticity

As a test of the impact of orbital ellipticity on the size of star clusters a simulation with a non-circular orbit was executed. This simulated star cluster has a perigalacticon of 4 kpc and an apogalacticon of 8 kpc, thus interposed between the two circular orbits at 4 and 8 kpc. The mass-loss rate of the simulated star cluster evolving on an elliptical orbit closely resembles the mass-loss rate of the cluster evolving on a circular orbit at 8 kpc. In

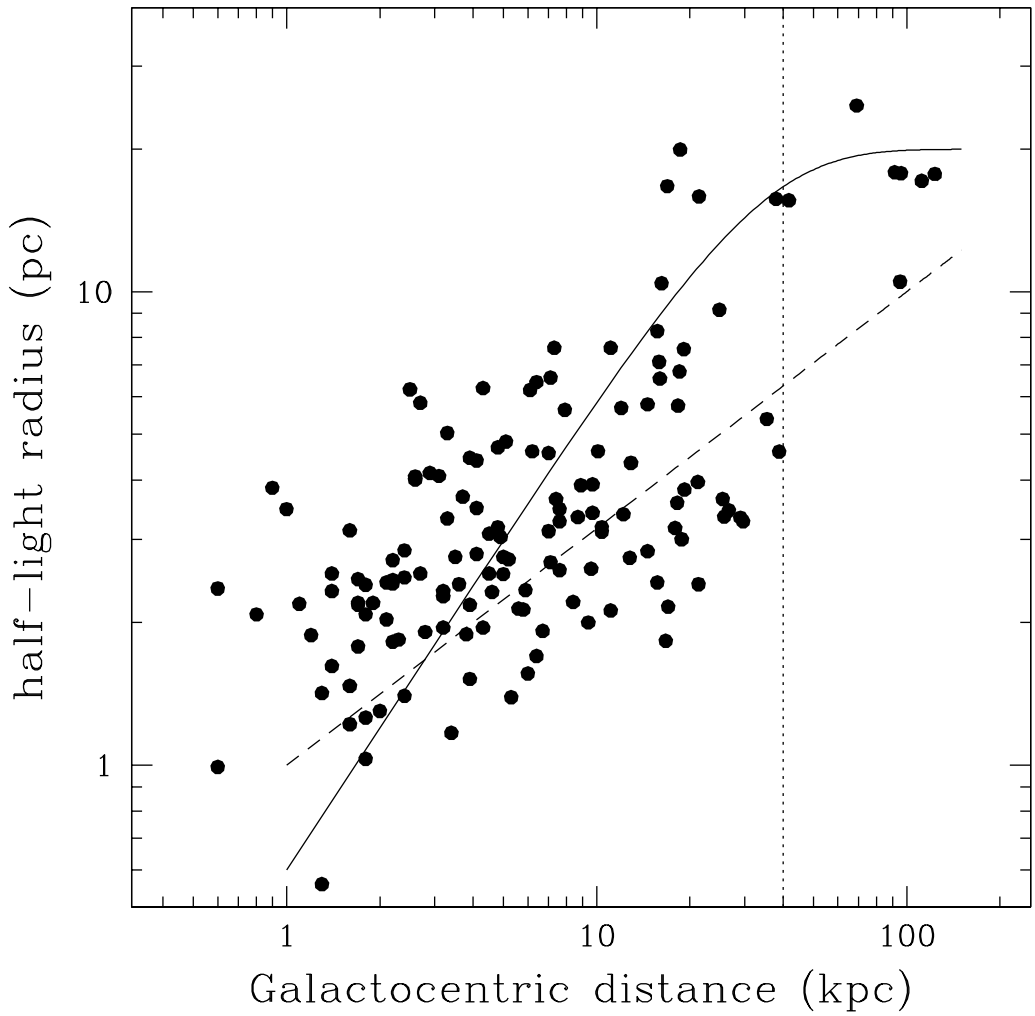

Figure 5.6 Effective radius vs. galactocentric distance for Milky Way globular clusters. The solid line represents the equation $r_h = r_h^{max} \times tanh(\alpha R_{GC})$. The dashed line represents a power law of the form $r_h = \sqrt{R_{GC}}$. The dotted line marks 40 kpc from the galactic center, at this distance the effective radii of globular clusters plateaus.

fact, after a Hubble time of evolution the difference in mass between these two simulated clusters is only $\sim 10\%$. That is, the simulation on a circular orbit at 8 kpc has $\sim 10\%$ more mass than the simulation on an elliptical orbit. Similarly, the half-mass radius is $\sim 12\%$ larger for the circular simulation at 8 kpc after a Hubble time.

King (1962) postulated that the tidal radius is imposed at perigalacticon however this has been recently debated (Küpper et al. 2010b, Baumgardt et al. 2010). The exploratory findings presented above show that the half-mass radius is closer to being set at apogalacticon.

5.6.8 Extended Outer Halo Star Clusters

Mackey & van den Bergh (2005) find a deficit of compact galactic young halo clusters at $R_{GC} > 40$ kpc. All clusters at these distances have larger than average effective radius, i.e. $r_h > 10$ pc, in agreement with the proposed relation of effective radius with galactocentric distance for star clusters $r_h \propto \sqrt{R_{GC}}$ (van den Bergh et al. 1991, McLaughlin 2000).

These extended clusters are believed to be accreted from now-destroyed satellite dwarf galaxies with milder tidal fields (Mackey & van den Bergh 2005). Under the initial conditions of the simulations carried out in this study, Figure 5.2 shows that there is no need for merger events with dwarf galaxies to grow extended star clusters in the Milky Way at large galactocentric distances.

The simulated star clusters evolving at 50 and 100 kpc from the galactic center undergo the initial expansion due to mass loss triggered by stellar evolution and then experience a small yet steady increase in half-mass radii (Figure 5.2). The tidal field is too weak at large distances from the galactic center to exert its truncating effects. Smaller initial sizes would lead to slightly smaller observed sizes. However, increased initial masses would more than compensate for this effect and still produce extended clusters at large galactocentric distances.

5.6.9 A Bimodal Size Distribution of Star Clusters Orbiting Dwarf Galaxies

Da Costa et al. (2009) find a bimodal distribution in the effective radius of globular clusters that are satellites of dwarf galaxies. Two peaks are seen in the size distribution of star clusters: one at ~ 3 pc and a second peak at ~ 10 pc. Da Costa et al. (2009) postulate that the second peak at 10 pc is present when globular cluster systems evolve in a weak tidal field. They also note that extended star clusters in the Andromeda galaxy, the Large Magellanic Cloud, and the Milky Way are found at large galactocentric distances.

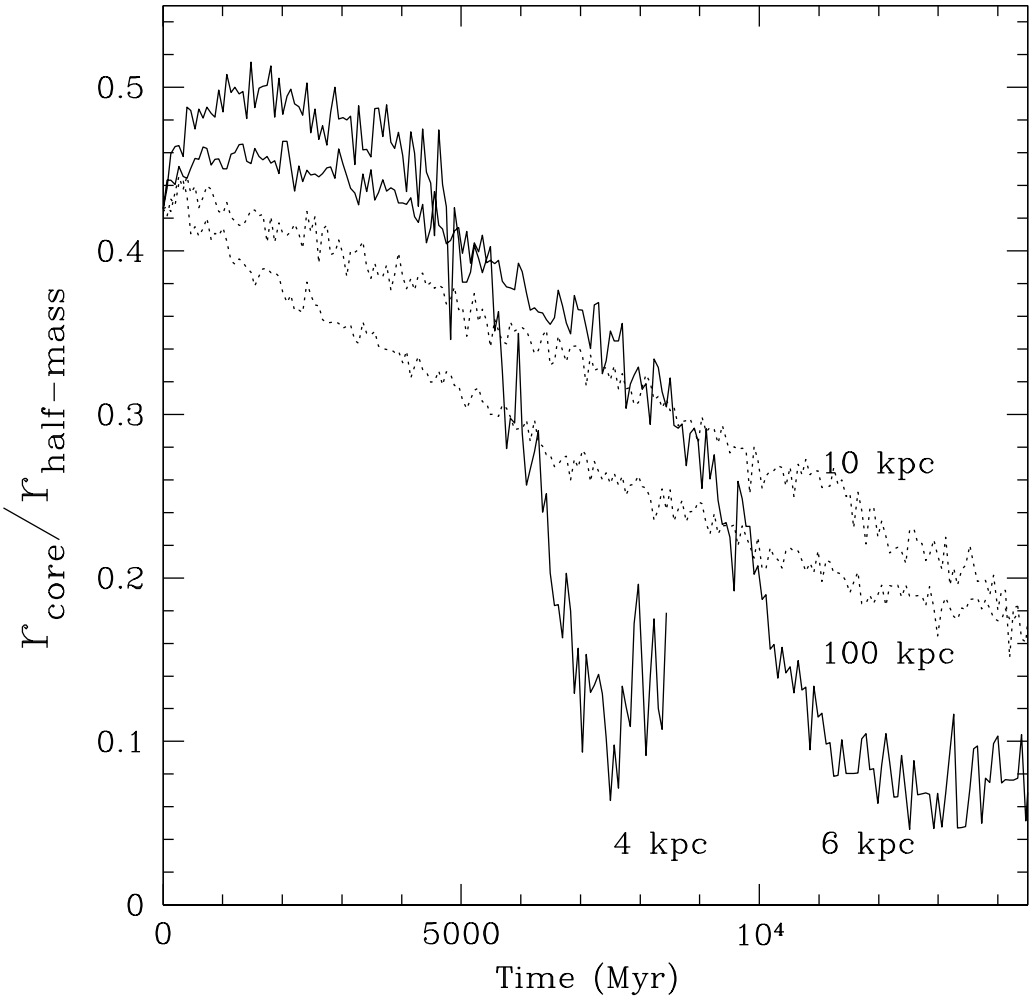

Figure 5.7 Time evolution of the ratio of core over half-mass radius. Solid lines are models at 4 and 6 kpc while dotted lines are models at 10 and 100 kpc from the galactic center. Both clusters with orbits at 4 and 6 kpc from the galactic center reach core collapse before a Hubble time.

From the N-body models carried out for this work it can be seen that the first peak of the size distribution found by Da Costa et al. (2009) at $r_h \sim 3$ pc can be explained by clusters that are originally massive enough to survive the mass loss due to tidal stripping. Their size however is determined by tidal interactions with the host galaxy. The second peak in the distribution at $r_h \sim 10$ pc would be created by star clusters evolving in a benign tidal environment, determined only by stellar evolution and internal dynamics.

5.7 The Dissolution of a Star Cluster

Figures 5.1 and 5.2 show that the model cluster evolving on a circular orbit with a radius of 4 kpc around the galactic center does not survive a Hubble time. The fierce mass loss of a cluster evolving at 4 kpc from the galactic center drives the cluster to dissolution after 8.4 Gyr. This particular simulation was run twice with a different seed for the initial particle distribution to ensure that the dissolution before a Hubble time was reproducible.

A simulation with a more dense and compact star cluster evolving at 4 kpc from the galactic center was also computed. This simulation has an initial half-mass radius of 3.1 pc and the same mass of the other simulations presented here, i.e. $M_{tot} \approx 6.3 \times 10^4 M_{\odot}$. A higher density provides shielding from the tidal field evident from this denser simulation surviving up 13.3 Gyr. However it has less than one thousand stars remaining after 12.5 Gyr and is only left with $M_{tot} = 764 M_{\odot}$. This work provides a solid lower limit to the initial mass of star clusters seen today evolving at close range from the center of a Milky Way type galaxy.

The dissolution of the simulated star cluster at 4 kpc is real and of significance to explain the galactic globular cluster system radial density profile. The radial density distribution of Galactic globular clusters is described by a power law with a core (Djorgovski & Meylan 1994). A simple power law is a good fit for the radial distribution of globular clusters at large galactocentric distances. However, at $R_{GC} \leq 3.5$ kpc, a flattening of the radial distribution of clusters occurs making the overall distribution better described by a Sérsic profile (Sérsic, 1968) with a Sérsic index of n=3 (Bica et al. 2006).

The central flattening of the globular cluster density profile has been explained as a result of a primordial density distribution with a depleted core (Parmentier & Grebel 2005), incompleteness due to obscuration, or the result of enhanced destruction rates of globular clusters in the central regions of the galaxy. Near infrared surveys of the galactic core and Spitzer data have revealed a number of candidate globular clusters towards the galactic centre, e.g. Longmore et al. (2011). Incompleteness, however, remains a minor

factor when accounting for the apparent depletion of star clusters in the inner 3.5 kpc of the galaxy. Given that the simulation of a star cluster orbiting at 4 kpc from the Galaxy core shows its complete dissolution before it reaches a Hubble time, this is an argument in favor of tidal disruption being responsible for an enhanced destruction rate of star clusters in the inner 4 kpc of the Galaxy, particularly those at the lower end of the globular cluster mass function.

5.8 Binary Fraction

Recent estimates of binary fractions in young star clusters yield values of 30-40% and even higher for certain stellar types (Hu et al. 2010; de Grijs et al. 2013). Does a higher binary fraction in our simulations affect the results presented in this chapter? Indeed it is widely accepted that the presence of binaries will play an important role in the dynamics of star clusters (Heggie & Hut 2002). What is thus the impact of a higher primordial binary fraction on mass loss rates and effective radii?

As we already mentioned, the "standard" binary fraction in the simulations presented in this thesis is 5% of the initial 100 000 stars. This value is in agreement with previous estimates of binary fractions in globular clusters (Davis et al. 2008) and numerical simulations (e.g. Hurley et al. 2007).

We ran three independent simulations with initial binary fractions of 10%, 15%, and 20% in order to compare the results with our simulations having an initial binary fraction of only 5%. The initial value of N is kept constant at N=100 000 with the percentage of these stars that are binaries increasing. We should note that increasing the binary fraction in our simulations increases the total number of stars, also increasing the required computing time. Naturally, the initial mass of the star cluster also increases with larger binary fractions. The range of initial masses goes from $M_{tot} \approx 6.3 \times 10^4 M_{\odot}$ for the star cluster with a binary fraction of 5% to $M_{tot} \approx 7.3 \times 10^4 M_{\odot}$ for a binary fraction of 20%. The simulations for this section were all run at the same galactocentric distance of $R_{GC} = 8$ kpc.

The mass loss rates over ∼10 Gyr of evolution for four simulations with different binary fractions are plotted in Figure 5.8. The masses of the clusters have been normalized to unity given that the initial masses differ slightly as mentioned above. Figure 5.8 shows that the mass loss rates are practically indistinguishable between clusters with different binary fractions. The evolution of the half-mass radius is also very similar between simulations with increasing binary fractions. After 8 Gyr of evolution the simulated star clusters with

binary fractions of 10% or more have half-mass radii ∼0.2 pc bigger than the star cluster with a binary fraction of 5%. The overall size difference, however, is less than 2%, as shown in Figure 5.9. The exercise above shows that the results presented in this chapter remain valid for star clusters with initial binary fractions as high as 20%.

With these simulations we determine that the binary fraction remains roughly constant over time. For instance, after 12 Gyr of evolution, the simulation with an initial 20% binary fraction has a total number of systems (single stars + binaries) of N=30151, and a total number of binaries of N_B= 6812, that is a binary fraction of 23%. These results are consistent with the findings of Hurley et al. (2007).

5.9 Final Remarks

The parametrization of the size scale of star clusters presented above can be used as a primary test of the radial distribution of extragalactic globular clusters with respect to the host galaxy in observational studies where spectroscopic information is not available. Globular clusters with $r_h \gtrsim 10$ pc are expected to be at large galacocentric distances, extended clusters at $R_{GC} \lesssim 40$ kpc can be expected to be artifacts of projection. A well characterized size distribution of globular clusters across bulge, disk, and halo can also be used as an independent test of the mass of the different structural components of galaxies.

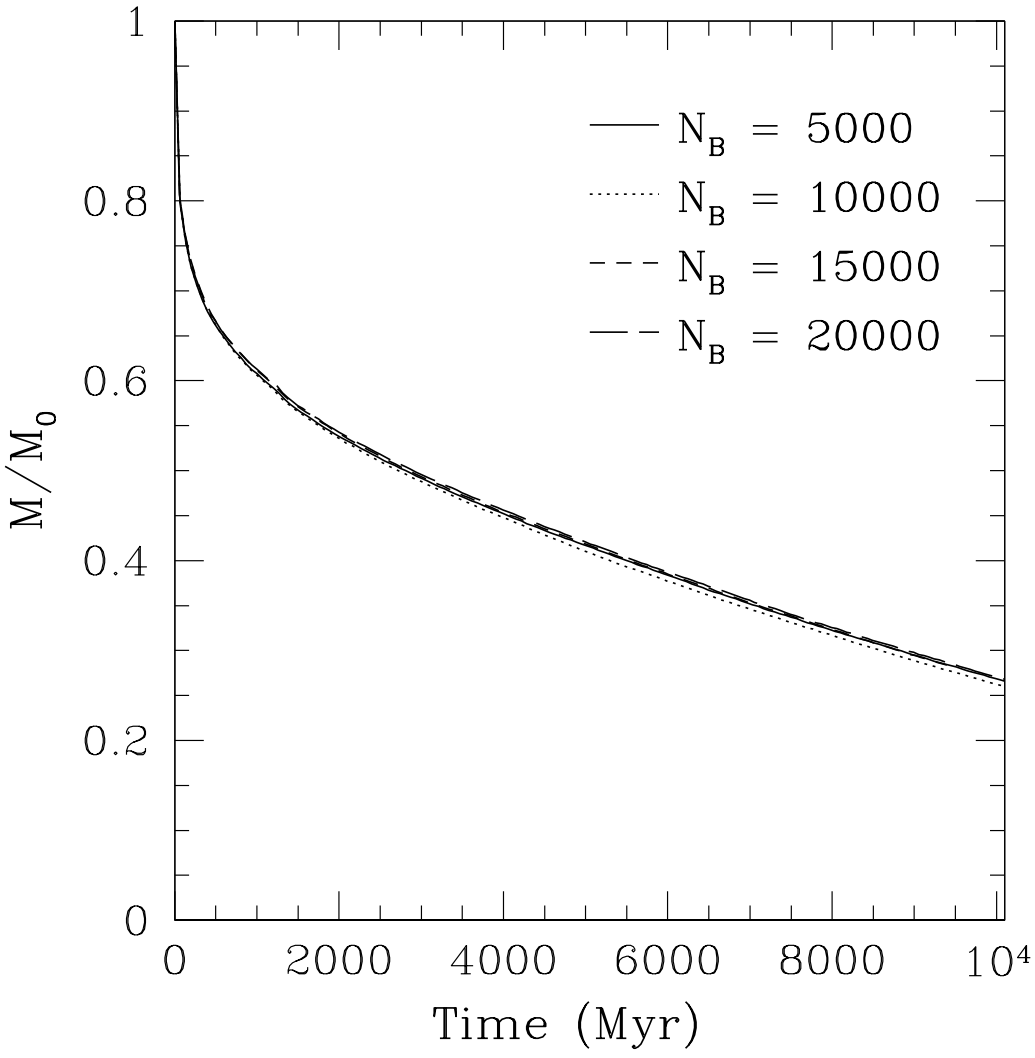

Figure 5.8 Normalized mass vs. time for simulated star clusters with different binary fractions. The total mass, and thus the mass loss rates are independent of the number of primordial binaries – up to N_B=20 000.

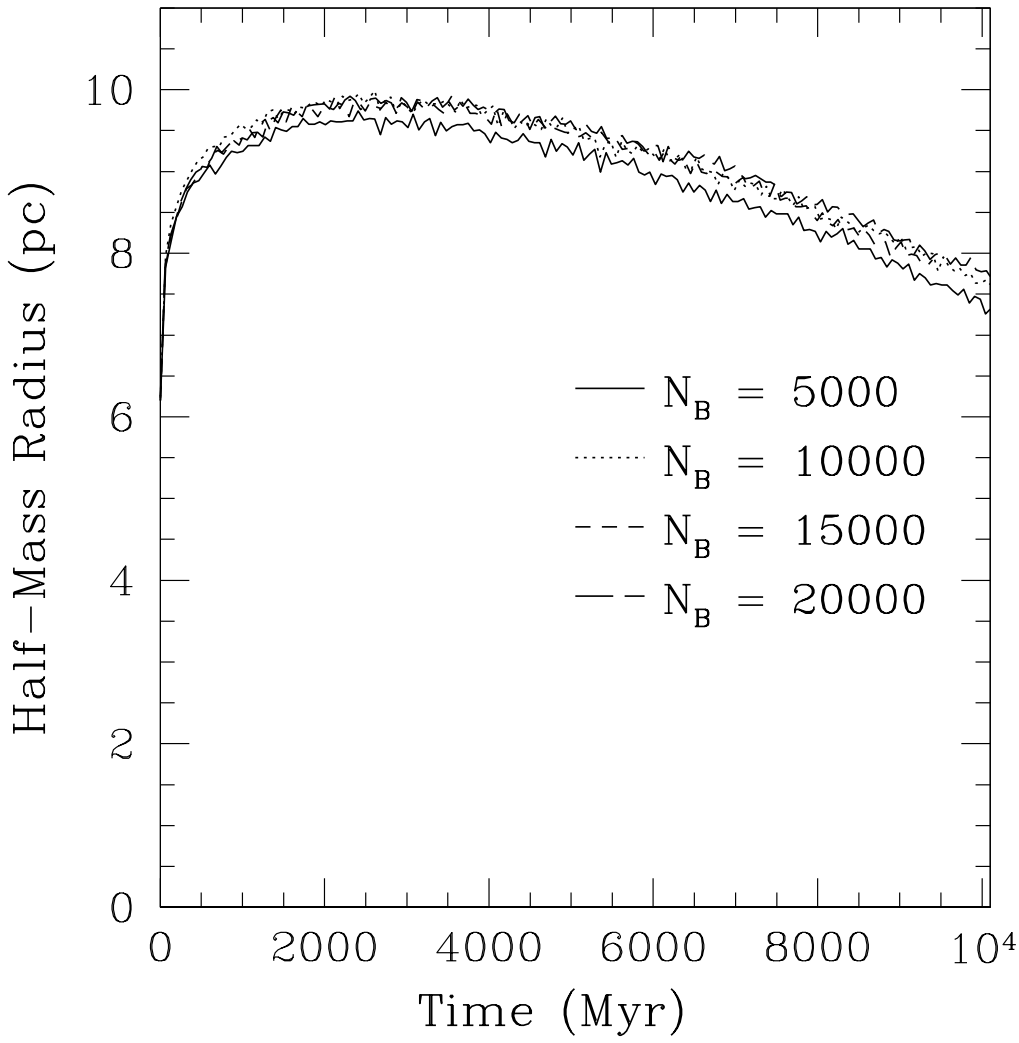

Figure 5.9 Half-mass radius vs. time for simulated star clusters with different binary fractions. The overall size difference between simulations with different binary fractions is less than 2% after 10 Gyr of evolution.

Table 5.1: **Parameters of Simulated Star Clusters after a Hubble Time.** The simulated star cluster evolving on a 4 kpc orbit dissolves before a Hubble time. Column 1 gives the galactocentric distance of the circular orbit in which the clusters evolve; Column 2: 3D half-mass radius; Column 3: mass in solar masses; Column 4: number of stars; Column 5: number of binaries; Column 6: number of half-mass relaxation times that have elapsed in a Hubble time (13 Gyr/t_{rh}).

R_{GC} (kpc) (1)	r_{hm} (pc) (2)	Mass $M_\odot$ (3)	N stars (4)	N binaries (5)	t/t_{rh} (6)
4	–	–	–	–	–
6	3.5	3.1 $\times 10^3$	4653	453	90.4
8	6.0	1.3 $\times 10^4$	25789	1703	17.9
8.5	6.7	1.5 $\times 10^4$	31602	1916	13.8
10	7.9	1.9 $\times 10^4$	44393	2331	9.1
20	11.2	3.0 $\times 10^4$	79591	3575	4.0
50	12.9	3.5 $\times 10^4$	94666	4069	3.0
100	13.1	3.6 $\times 10^4$	97506	4161	2.8

6

Shocking of Star Clusters by the Galactic Disk

6.1 Introduction

In the current paradigm of galaxy formation smaller structures merge into larger ones from the Big Bang up to the present day (White & Rees 1978). Galaxies grow through two main processes: the hierarchical merging with smaller galaxies and the accretion of fresh gas fuelling new star formation. These different mechanisms contribute to the growth of the disk, bulge and halo.

As the first significant stellar structures to form, globular clusters witness the entire evolution of their host galaxy as satellite systems. Indeed, globular clusters are believed to follow galaxies during galaxy mergers and close encounters (e.g. West et al. 2004). The gravitational potential of their host galaxy has a direct influence on the survival of globular clusters: they lose stars through tidal stripping and disk shocking. In turn, these lost stars contribute to the build-up of the galaxy's stellar halo. The evolution of host galaxy and globular clusters are clearly connected.

The aim of this work is to derive, using numerical simulations, the importance of the host galaxy disk mass and size on the evolution and survival of star clusters. How are satellite stellar systems affected by disks and bulges of changing mass and with different geometries? And reciprocally, how do satellite stellar systems contribute, through their dissolution, to the formation of the halo of the host galaxy?

D'Onghia et al. (2010) show that halo and disk shocking efficiently deplete the satellite population of dark matter halos within 30 kpc of the Milky Way center. The baryonic matter that constitute star clusters, with higher densities than dark matter substructures, experience strong interactions with the host galaxy disk.

In their important paper, Gnedin & Ostriker (1997) model the dynamical evolution of the Galactic globular cluster system using a Fokker-Planck code. These authors build on

earlier analytical work by Aguilar, Hut & Ostriker (1988) and Kundic & Ostriker (1995) among others. Gnedin & Ostriker (1997) give analytical expressions to estimate the impact of disk shocking and also call for numerical simulations to be carried out.

With the recent progress in computational capacity, large N-body simulations can now be carried out in order to determine the physical mechanisms that govern the dynamical evolution of globular clusters in a galactic potential. The approach in our work is purely numerical and different in nature to Gnedin & Ostriker (1997) given that no assumptions or explicit expressions to treat the impact of the disk are used.

N-body models of star clusters were run where the properties of the star cluster remain identical but the mass and geometry of the galactic disk change. The effect of the disk on the star cluster is computed as a part of the numerical calculations of the gravitational force experienced by each star.

The above is carried out with the code `NBODY6` used for the study of the dynamics of star clusters through N-body simulations. `NBODY6` now includes a detailed model of the host galaxy where star clusters evolve as satellites (Aarseth 2003). The current set-up of `NBODY6` includes the tools to model a Milky-Way type galaxy with three distinct components: disk, bulge, and halo (see Chapter 5). The gravitational force for each star of the cluster is computed at each time step by taking into account the effect of all other stars, and of the disk, bulge, and halo. We make use of this new capacity of `NBODY6` to run several models of star clusters where the mass and physical size of the disk are different between models.

Throughout this work, a Hubble time of 13.5 Gyr is adopted, in agreement with the results of the Wilkinson Microwave Anisotropy Probe (Spergel et al. 2003).

6.2 Models Set-up

`NBODY6` includes the different components of the galactic that model are static in time, as discussed in Chapter 5. Indeed the mass of the disk is assumed to be constant over time. In `NBODY6` the disk component of the galaxy is modeled following the prescriptions of Miyamoto and Nagai (1975):

$$\Phi(r,z) = \frac{GM}{\sqrt{r^2 + [a + \sqrt{(z^2 + b^2)}]^2}} \tag{6.1}$$

where G is the gravitational constant and M is the mass of the disk. The geometry of the disk can be easily modified by changing the parameters a (scale length) and b (scale

height). Different values adopted in previous work for these two parameters and the disk mass are given in Table 6.1. While different values of these scale parameters are explored in this work, the most often assumed values are $a = 4$ kpc and $b = 0.5$ kpc. Also, a commonly used value for the mass of the bulge is $M = 1.5 \times 10^{10} M_{\odot}$ (Xue et al. 2008) which we model as a point mass.

For a more detailed description of the simulated star clusters the reader is referred to Madrid et al. (2012; Chapter 5). Briefly, the star clusters start with N=100 000 stars, an initial mass of 6.4×10^4 $M_{\odot}$, a half-mass radius of 6.2 pc, and a spatial distribution that assumes a Plummer sphere (Plummer 1911). Models are run at 6 kpc from the galactic center, unless otherwise stated. At this distance, $R_{GC} = 6$ kpc, star clusters are free from bulge shocking while the effect of disk shocking is still strong within the configuration described above. With a few clearly identified exceptions simulated star clusters follow a circular orbit with an initial inclination of $\theta = 22.5$ degrees with respect to the galaxy disk. In cartesian coordinates the plane of the disk is in the (x, y) plane. The modelled clusters usually reach a high of $z_{max} = 2$ kpc. A definition and a discussion of the tidal radius used in this work is given in Section 6.6 and also in Chapter 5.

All the models for this chapter are performed on the new GPU Supercomputer for Theoretical Astrophysical Research (gSTAR) hosted at Swinburne University. Each model is computed on one NVIDIA Tesla C2070 GPU in combination with six processing cores on the host node. The approximate computer time to carry out one model of N=100 000 stars is three weeks. Two different machines were used to run the models presented in this thesis "Supermicro" and gSTAR. Supermicro was used to compute about half the models presented in Chapter5. We ran an identical model on the two different machines to ensure that the results were identical. These models are clearly independent of the hardware in use. For instance, the total mass vs. time graphs are virtually undistinguishable between the simulations that we ran on gSTAR and on Supermicro, i.e. the results differ by less than 0.1%.

6.3 A Heavier or Lighter Disk

Independent models of globular clusters are run with different masses for the host galaxy disk. The mass of the disk is made to vary between $1 \times 10^{10} M_{\odot}$ and $10 \times 10^{10} M_{\odot}$ by incremental steps. The first step is of $1.5 \times 10^{10} M_{\odot}$ while subsequent steps are of $2.5 \times 10^{10} M_{\odot}$. This range of values covers the different masses that a disk has during its evolution according to galaxy formation theory (e.g. Leitner 2012). These disk masses

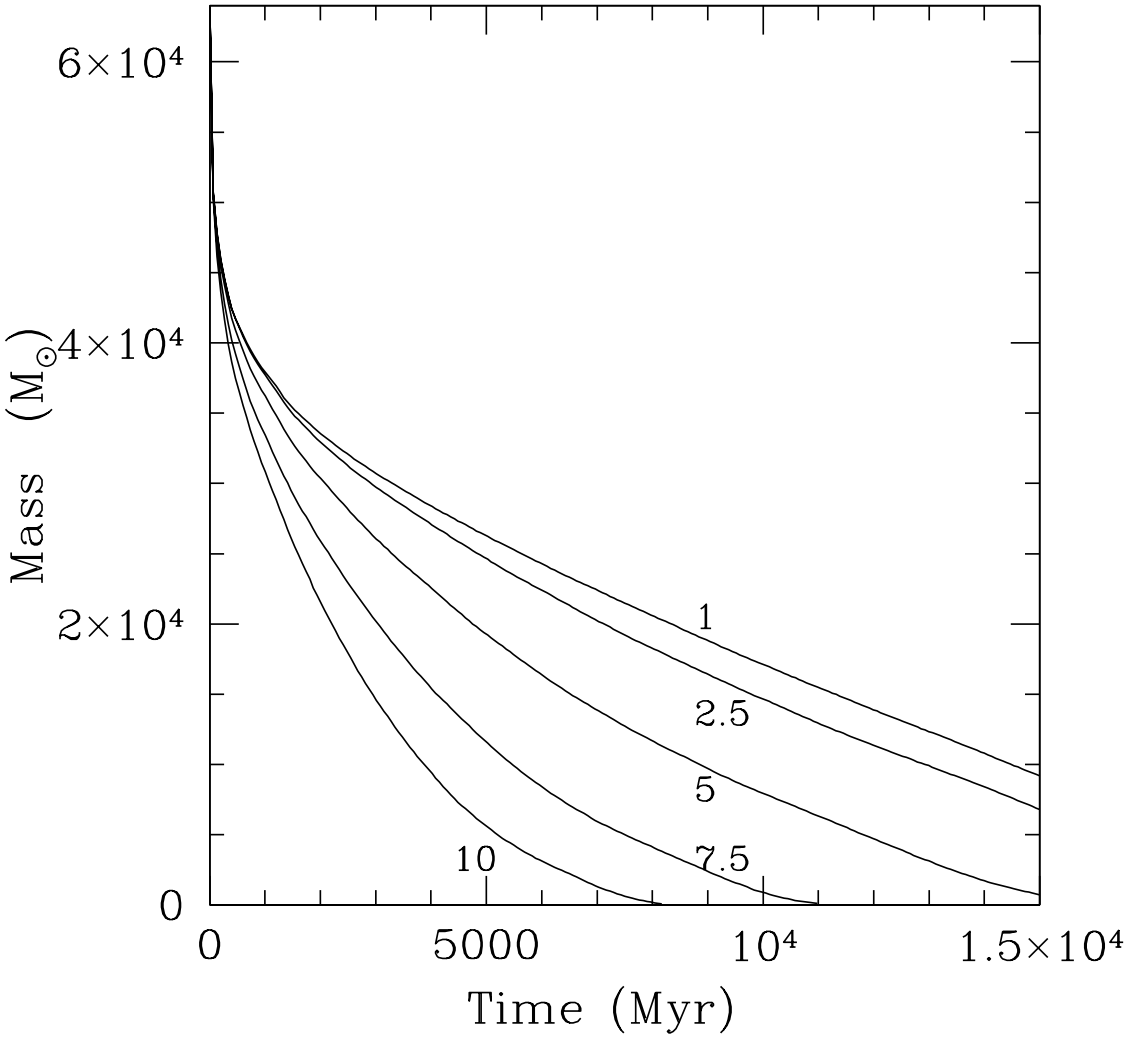

Figure 6.1 Total mass of simulated star clusters vs. time for models with disks of different masses. The labels give the mass of the disk in units of 10^{10} $M_\odot$, the lightest disk being 1×10^{10} $M_\odot$. Heavier disk masses enhance mass loss rates and accelerate the dissolution of star clusters.

are also consistent with values published in the literature and shown in Table 6.1. This series of models are run at the same galactocentric distance of 6 kpc, and with the same properties, the only parameter that changes in the simulations is the disk mass. The geometry of the disk is kept constant with $a = 4$ kpc and $b = 0.5$ kpc.

The total mass of simulated star clusters vs. time in simulations with different disk masses is plotted in Figure 6.1. A natural result of these simulations is that a more massive disk enhances the mass loss rate of an orbiting star cluster owing to a stronger tidal field. An enhanced mass loss rate implies a shortened dissolution time. The star cluster that orbits a "light" disk with a mass of $1 \times 10^{10} M_{\odot}$ has a remaining mass of $1.2 \times 10^{4} M_{\odot}$, or 19% of its initial mass, after a Hubble time of evolution. On the other extreme, a star cluster that evolves within a "heavy" disk with a mass of $10 \times 10^{10} M_{\odot}$ is completely dissolved after 8.2 Gyr of evolution. As expected, disks with masses between these two examples define intermediate regimes of mass loss, as shown in Figure 6.1.

Table 6.1: **Published Values for Mass and Structural Parameters of the Galactic Disk.** This table gives published values for the mass and structural parameters of the disk for Milky-Way type galaxies. The values of a and b correspond to the disk scale length and disk scale height

Reference	Disk Mass ($M_{\odot}$)	a (kpc)	b (kpc)
(1)	(2)	(3)	(4)
Bullock & Johnston (2005)	1.0×10^{11}	6.5	0.26
Gómez et al. (2010)	7.5×10^{10}	5.4	0.30
Paczynski (1990)	8.1×10^{10}	3.7	0.20
Peñarrubia et al. (2010)	7.5×10^{10}	3.5	0.3
Read et al. (2006)	5.0×10^{10}	4.0	0.50

By introducing the half-mass relaxation time t_{rh}, also computed by `NBODY6`, we can derive a simple relation between the number of relaxations a star cluster undergoes before dissolution and the mass of the disk. The half-mass relaxation time, already given in Chapter 5, is:

$$t_{rh} = \frac{0.14N}{\ln \Lambda} \sqrt{\frac{r_{hm}^3}{GM}}, \tag{6.2}$$

where $\Lambda = 0.4N$ is the argument of the Coulomb logarithm, N is the number of stars, and

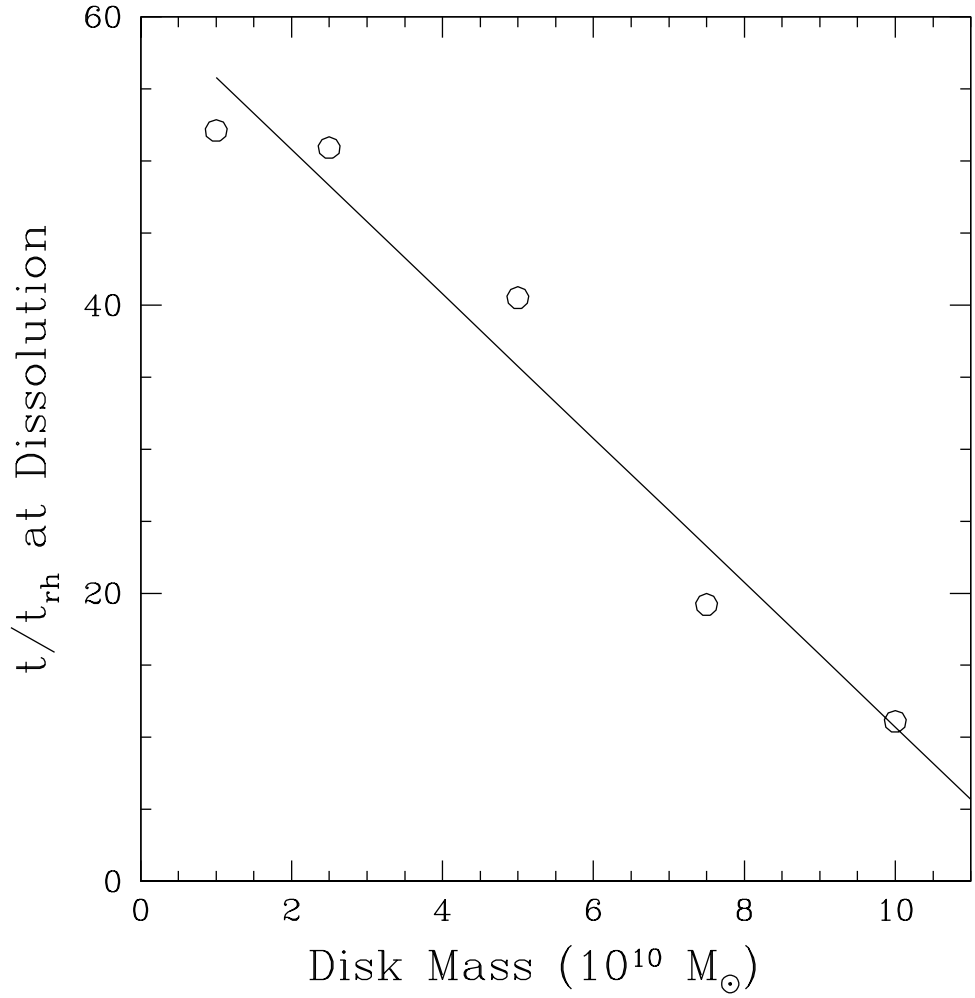

Figure 6.2 Dissolution time/relaxation time (t/t_{rh}) vs. disk mass for star clusters orbiting at 6 kpc from the galactic center. t/t_{rh} is computed when the star cluster has only 10% of its initial mass left. A heavier disk shortens the number of relaxations a star cluster undergoes before dissolution.

r_{hm} the half-mass radius, (Spitzer & Hart 1971; Binney & Tremaine 1987). Figure 6.2 shows the number of relaxation times (t/t_{rh}) vs. mass of the disk at the time when the cluster has only 10% of its initial mass left. This quantity ($10\%M_0$) is preferred over the time it takes for the cluster to completely dissolve since numerical simulations become noisy for low N owing to small number statistics. The best fitting linear relation between relaxation time and disk mass is plotted in Figure 6.2 and is given by

$$t/t_{rh} = -5 \times \frac{M}{10^{10} M_{\odot}} + 61. \tag{6.3}$$

We find that doubling the mass of the disk from $5 \times 10^{10} M_{\odot}$ to $10 \times 10^{10} M_{\odot}$ leads to the dissolution of the star cluster in half the time.

6.4 Disk Geometry

The current set-up of `NBODY6`, based on the formula of Miyamoto and Nagai (1975), allows the geometry of the disk to be modified by changing the values of the parameters a and b of Eq. 6.1 (or Eq. 5.8). Table 6.1 shows that the mass and structural parameters of the Galactic disk take a range of values in different studies. Eighteen models of star clusters where the disk has different scale parameters were carried out in order to evaluate the impact of disk geometry on the survival and evolution of star clusters.

Selected parameters of models executed for this section are listed in Table 6.2. The middle panel of this table also lists some of the models presented in Chapter 5, i.e. models 12 through 15. Other models such as those with smaller number of initial particles used for scaling and those with higher binary fractions are not included in this table.

Three disk geometries are considered where the concentration of the disk mass density profile varies from a disk mass highly concentrated towards the center of the galaxy to a disk mass with an extended mass profile. In these different models the disk has the same mass but different spatial distribution. Values for the disk scale parameters are $a = 0.4$ kpc and $b = 0.5$ kpc for the first set of models (models 1 through 5 in Table 6.2). By running models with $a = 0.4$ kpc and $b = 0.5$ kpc the shape of the disk changes to a more centrally concentrated one, as the value of the scale length parameter a is ten times smaller than the standard value used in the second set of models. The second set of models (labels 9 and 12 to 15 on Table 6.2) have disk parameters $a = 4.0$ kpc and $b = 0.5$ kpc. A third set of models was carried out with a "flattened" or more extended disk where the scale parameters are $a = 8$ kpc and $b = 0.5$ kpc (models 16 to 20 in Table 6.2).

The disk density profiles of the three different disk geometries are represented in Fig-

ure 6.3. The disk model with the Miyamoto and Nagai scale parameters $a = 0.4$ kpc and $b = 0.5$ kpc is represented on the top panel. In this model, the mass of the disk is highly concentrated towards the center of the galaxy with a very steep fall off: the disk mid-plane density drops from $3.5{\times}10^9$ $M_\odot/kpc^3$ at $R_{GC} = 1$ kpc to 1×10^7 $M_\odot/kpc^3$ at $R_{GC} = 7$ kpc.

For each disk profile we study the evolution of an identical star cluster at six different radii from the galactic center. Models were executed at $R_{GC} = 4$, 6, 8, 10, 12.5, and 15 kpc from the galactic center. In Figure 6.3, circles with sizes proportional to the masses of the simulated star clusters, after 10 Gyr of evolution, are drawn at their respective orbital distances. The percentage of the initial star cluster mass remaining after 10 Gyr is also given in Figure 6.3.

Several simulated clusters do not survive to 10 Gyr, let alone up to a Hubble time. For the first set of models, with a very concentrated disk, the simulated star cluster evolving at 4 kpc from the center of the galaxy is totally dissolved at a record time of only 334 Myr. The simulated star cluster at an orbit of 6 kpc has a remaining mass of only $\sim$870 $M_\odot$ at 10 Gyr, just, $\sim$1% of its initial mass. At 8 kpc from the galactic center the modelled star cluster has 28% of its initial mass after 10 Gyr of evolution.

The middle panel of Figure 6.3 shows the disk density profile for a disk model with $a = 4$ kpc and $b = 0.5$ kpc, i.e. the same geometry as the models of Section 3. In this second set of models, the star cluster orbiting at 4 kpc is also completely dissolved before 10 Gyr.

The star cluster orbiting at 6 kpc in this more extended disk model (middle panel) has a mass of 7972.8 $M_\odot$ after 10 Gyr of evolution, nine times the mass of the star cluster retained in a centrally peaked disk model. Clusters on orbits of 8 kpc in both models have virtually the same mass, i.e. only 1% difference, after 10 Gyr of evolution. Similarly, for models at $R_{GC} = 10$ kpc and beyond their mass difference is clearly measurable but on the order of 3% for clusters at $R_{GC} = 10$ and 12.5 kpc and 2% for clusters at $R_{GC} = 15$ kpc.

A third set of models, with a more extended disk, was also studied. These models are represented in the bottom panel of Figure 6.3. With this disk geometry, that is $a = 8$ kpc and $b = 0.5$ kpc, the mass of the disk is more spread out and the additive tidal effects of bulge and disk are not strong enough to completely disrupt the star cluster evolving at $R_{GC} = 4$ kpc. This innermost star cluster survives 10 Gyr of evolution with 8% of its initial mass.

The models presented above show that disk geometry has a clear impact on the globular

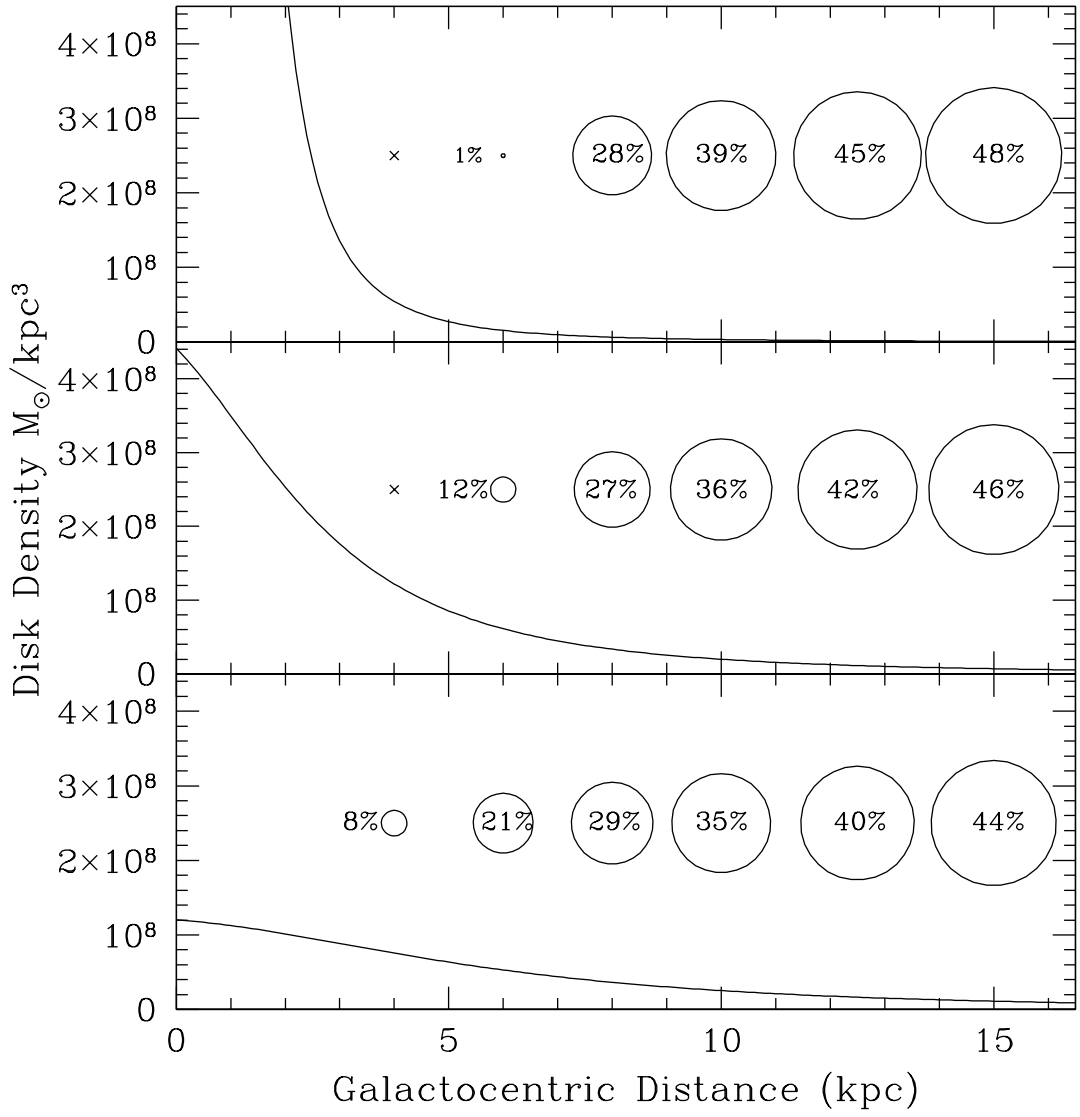

Figure 6.3 Effect of a different disk geometry, at constant disk mass, on orbiting star clusters. The mass density profiles, at the midplane ($z = 0$), for three different disk geometries are plotted as a solid line in each panel. The size of the circles symbolizes the mass remaining in a star cluster after 10 Gyr of evolution. The percentage of the initial mass left is also given for all models. Star clusters are represented at their respective galactocentric distances. *Upper panel*: A galaxy disk with its mass concentrated at the center of the galaxy with scale length parameters of a=0.4 kpc and b=0.5 kpc (models 1 to 6 in Table 6.2). *Middle panel*: Galaxy disk with commonly used parameters a=4 kpc and b=0.5 kpc (models 10, 13 to 17). *Lower panel*: A more extended galaxy disk, a=8 kpc and b=0.5 kpc (models 18 to 23).

cluster mass function. This impact is more evident in the inner regions of the galaxy where a centrally concentrated disk (upper panel of Figure 6.3) adds to the tidal effects of the bulge and enhances the destruction rate of globular clusters within 6 kpc of the galactic center. At $R_{GC} = 8$ kpc there is a switch or transition in the tidal effects following the different disk geometries. Star clusters at $R_{GC} = 10$ kpc and beyond have more mass on the first set of models with the centrally concentrated disk than on the second and third set of models with more extended disks. The tidal effects of the disk are still clearly measurable out to $R_{GC} = 15$ kpc but are small in intensity, of the order of 3 to 5% of the initial mass.

During 10 Gyr of evolution most of the mass of star clusters within $R_{GC} = 6$ kpc will be transfered to the host galaxy. Mass transfer from globular clusters to the host galaxy in the form of stellar tidal tails has been well documented observationally in Galactic globular clusters and modelled by Küpper et al. (2010a). Odenkirchen et al. (2001) described the presence of two tidal tails emerging from Palomar 5 using SDSS data. After dissolution, the stars that formed the star cluster become part of the host galaxy stellar population.

6.5 Heating and Cooling During Disk Crossings

Gnedin & Ostriker (1997) describe the effect of disk shocking as a shock or impulse of extra energy given to each star in the cluster as it crosses the disk (see also Spitzer 1958; Gnedin & Ostriker 1999). Stars close to the tidal boundary can be lost during disk crossing events given that this extra energy allows them to escape from the star cluster. This section presents a close-up of the mass-loss and velocity dispersion of star clusters at each disk crossing.

A simulation with output given at more frequent intervals (every 1 Myr) was carried out to sample in detail the effects of a single disk crossing on a star cluster. The simulated star cluster is placed at 6 kpc from the galactic center with disk scale parameters of a= 4 kpc and b= 0.5 kpc, an initial orbital inclination of $\theta = 22.5$ degrees and an orbital period of ∼150 Myr. The height of the star cluster above the plane of the disk and the internal velocity dispersion are represented in Figure 6.4. The internal velocity dispersion shown in Figure 6.4 corresponds to the velocity dispersion of the outer 50% of the mass of the cluster, this is the section of the star cluster where individual stars experience the greatest changes in energy during each disk crossing. The velocity dispersion depicted in Figure 6.4 has been offset from an average level of ∼2 km/s. For comparison, the average internal velocity dispersion of the entire star cluster is ∼3 km/s after 3 Gyr of evolution.

The maximum height reached by a star cluster is 2 kpc from the plane of the disk.

A periodic impulse given to the velocity dispersion of the outer layers of the star cluster at each disk crossing is evident in Figure 6.4. The amplitude of this impulse, measured from an average level before disk crossing, is of 0.11 km/s. This increase is 5.2% in the average velocity dispersion of the stars that make up the outer 50% of the star cluster mass. There is a time delay of ∼7 Myr between the star cluster crossing the equatorial plane of the disk (i.e. z=0) and the peak of the impulse in velocity dispersion. This time delay is of the same order of magnitude as the crossing time that is in this case $t_{cross} \sim 2$ Myr. Following its peak the velocity dispersion of the star cluster experiences a reduction of ~ 0.14 km/s on average. Gnedin et al. (1999) mention a "refrigeration effect" or slight reduction in the energy dispersion of a star cluster following a disk shock. Figure 6.4 shows that at every disk crossing an increase is followed systematically by a decrease in velocity dispersion.

The same velocity dispersion discussed above and the mass of the cluster outside its tidal radius (M_{out}) are plotted in Figure 6.5. The tidal radius is defined as it was in Madrid et al. (2012; Ch. 5), that is following the formula of Küpper et al. (2010):

$$r_{\rm t} \simeq \left(\frac{GM_{\rm C}}{2\Omega^2}\right)^{1/3} \tag{6.4}$$

where Ω is the angular velocity of the cluster, M_G is the mass of the galaxy, and G is the gravitational constant. We define an escape radius beyond which stars are no longer part of the simulation. This escape radius scales with the tidal radius over the time evolution of the cluster. The escape radius is at least two times the length of the tidal radius, see Madrid et al. (2012; Ch 5) for more details. The mass outside the tidal radius M_{out} plotted in Figure 6.5 corresponds to the mass between the tidal radius and the escape radius.

Figure 6.5 shows that at each disk crossing (z=0) the mass outside the tidal radius reaches a minimum, reflecting the strength of the tidal field felt by the star cluster. Over the ten disk crossings represented in Figure 6.5 the star cluster loses ∼2600 $M_\odot$, that is on average 260 $M_\odot$ per disk crossing. After the star cluster passes the disk its velocity dispersion decreases and the mass outside the tidal radius increases as this region of the cluster fills up due to a weaker tidal field. M_{out} reaches a maximum when the star cluster is at the furthest distance from the disk.

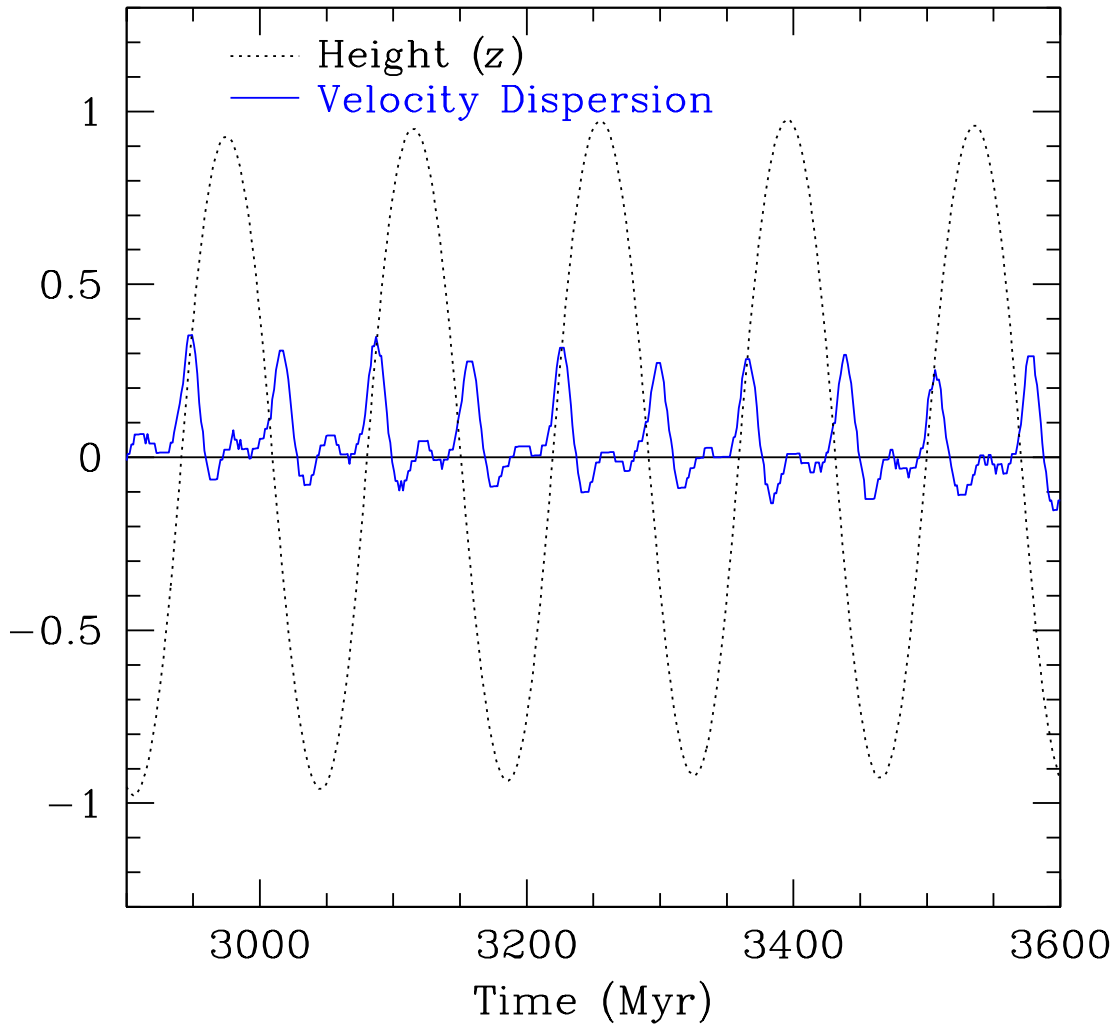

Figure 6.4 Star cluster height above the plane of the disk and velocity dispersion of stars in the outer 50% of the star cluster mass. At each disk crossing the outer layers of the star cluster experience an increase in their internal velocity dispersion. Both height and velocity dispersion have been scaled vertically for display purposes. The average velocity dispersion decreases slightly over the time plotted in this figure, a slope with a factor of $1 \times 10^{-4} \times$Time that has been added as a correcting factor for display purposes. The maximum height in the orbit of the star cluster is 2 kpc above the plane of the disk.

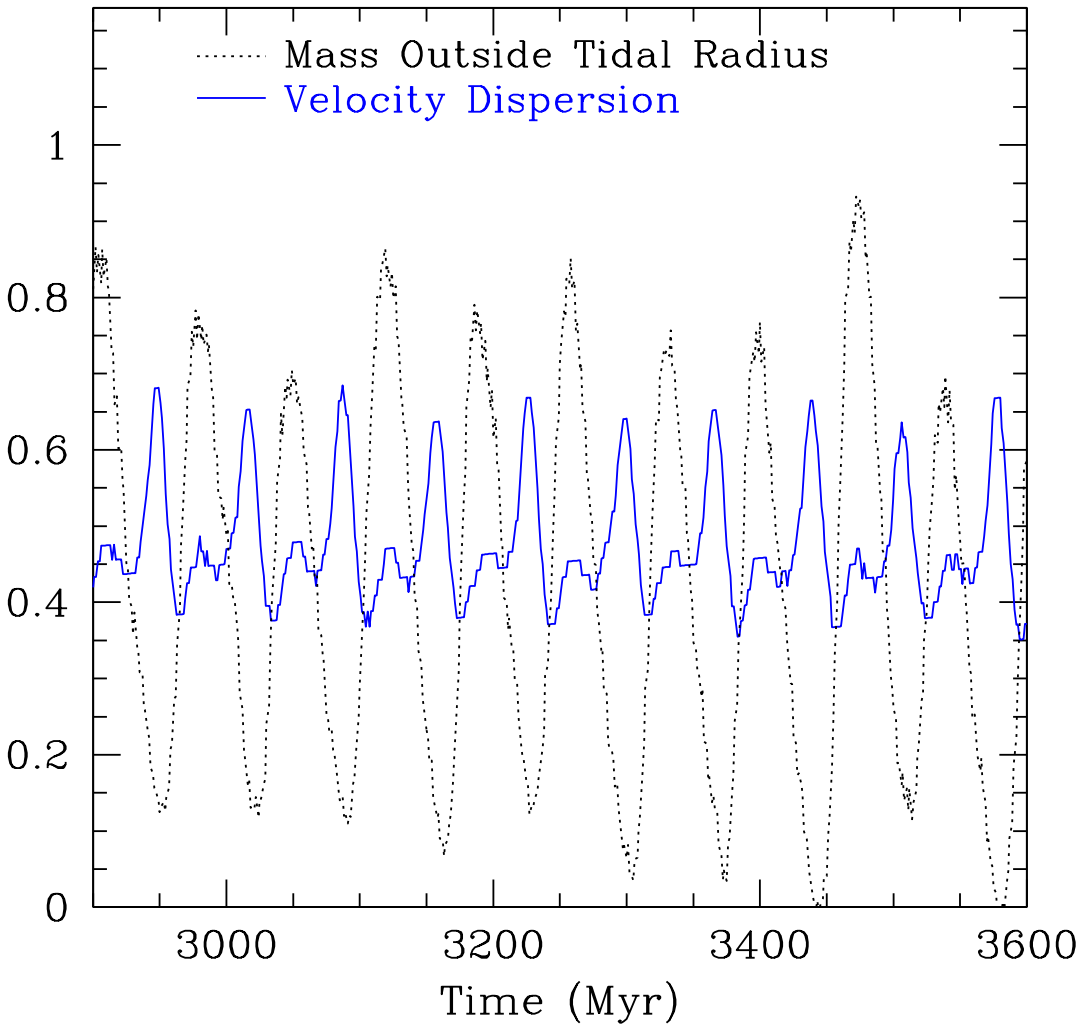

Figure 6.5 Mass of the star cluster outside the tidal radius and velocity dispersion of stars in the outer 50% of the star cluster mass. The minimum and maximum physical values of the velocity dispersion oscillations are 1.89 and 2.03 km/s. The mass outside the tidal radius oscillates between 127 and 305 $M_{\odot}$ during the time represented above. Both quantities have been scaled for display purposes.

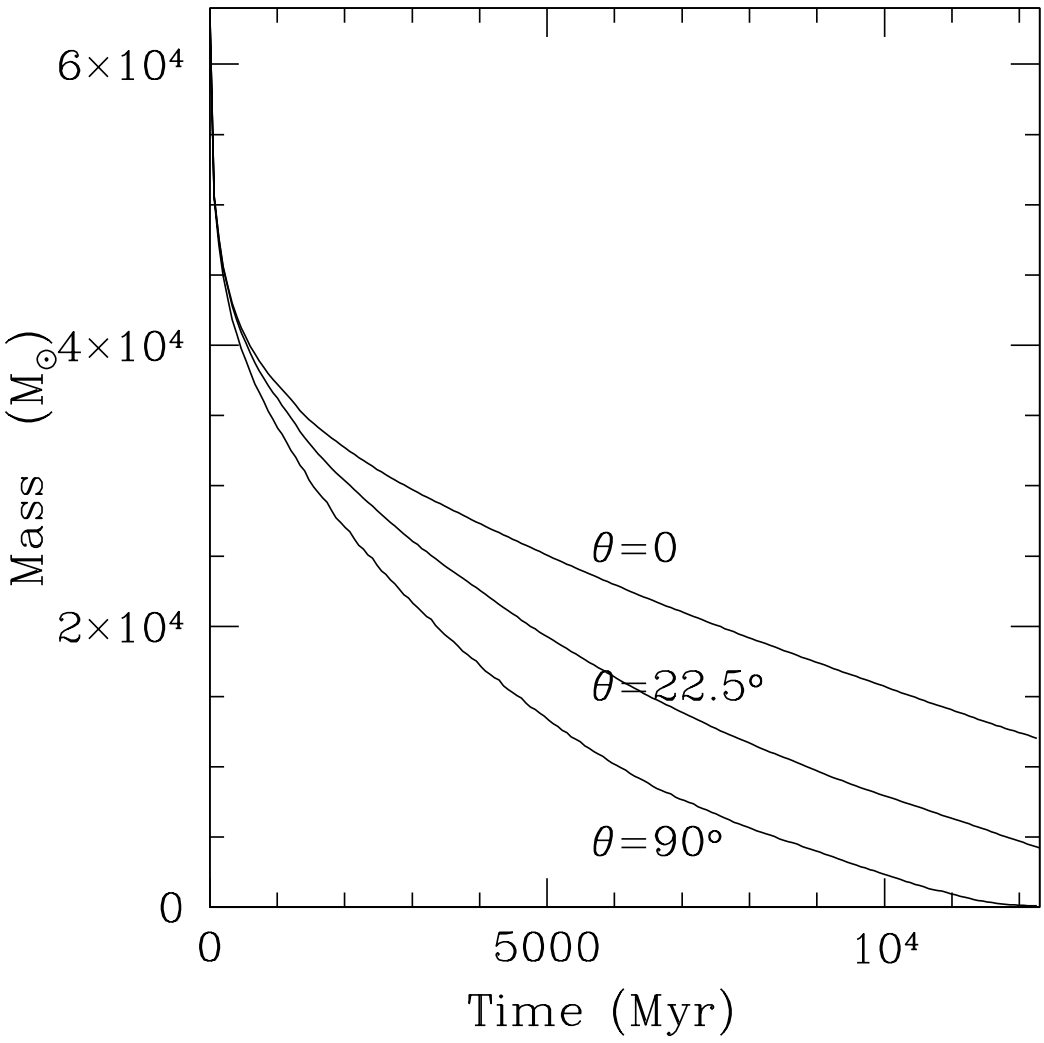

Figure 6.6 Star cluster mass vs. time for three clusters with different orbital inclination. Three inclinations are shown here: a star cluster orbiting in the plane of the disk $\theta = 0$, with a "standard" orbit $\theta = 22.5°$, and perpendicular to the disk $\theta = 90°$.

6.6 Orbital Inclination

For a cluster on an inclined orbit the passage through the disk implies an enhanced, or impulsive, gravitational force owing to the proximity of the mass that constitutes the disk, as shown in the previous section. Is the transient nature of the energy shift that stars receive during disk passages more important than a high but constant tidal field? In order to properly disentangle the tidal effects and those of disk shocking, two simulations with different orbital inclination were carried out. One simulated star cluster orbits the galaxy in the plane of the disk, that is, all its initial velocity is in the y direction $V = V_y, (\theta = 0)$. A second simulation, with the same characteristics of the previous simulation, evolves in an orbit perpendicular to the disk ($\theta = 90^\circ$), in this case, $V = V_z$. Both simulations evolve at a galactocentric distance of 6 kpc, with a disk mass of $5 \times 10^{10} M_\odot$ and are otherwise identical to the previous simulations with $\theta = 22.5^\circ$.

The impact of orbital inclination on the mass of the star cluster is shown in Figure 6.6. We plot the total mass vs. time taking as a reference a simulated star cluster in a "regular" or "standard" orbit with an inclination of $\theta \sim 22.5^\circ$. We also plot the total masses of the simulated star clusters with orbits on the plane of the disk ($\theta = 0$), and perpendicular to it ($\theta = 90^\circ$).

Figure 6.6 shows that the star cluster in a perpendicular orbit to the plane of the disk is affected by a stronger mass loss than the cluster in a less inclined orbit or the cluster in an orbit in the plane of the disk. The simulated cluster on the orbit perpendicular to the disk is fully dissolved in 12.3 Gyr. After 12 Gyr of evolution, the simulated cluster evolving in the plane of the disk is 87 times more massive than the cluster on the orbit perpendicular to the disk. That is a total mass difference of 4477 $M_\odot$.

The models discussed in this section show that the compressive shocks experienced by the star cluster at each disk crossing are a dominant factor driving its dissolution. The variable gravitational potential generated by the presence of the disk on the orbit of the star cluster plays a more important role in the dissolution of the cluster than a constant and higher tidal field experienced by a star cluster that evolves in the plane of the disk. Note that star clusters with a small inclination angle with respect to the disk will experience additional shocking due to the presence of spiral arms (Gieles et al. 2007).

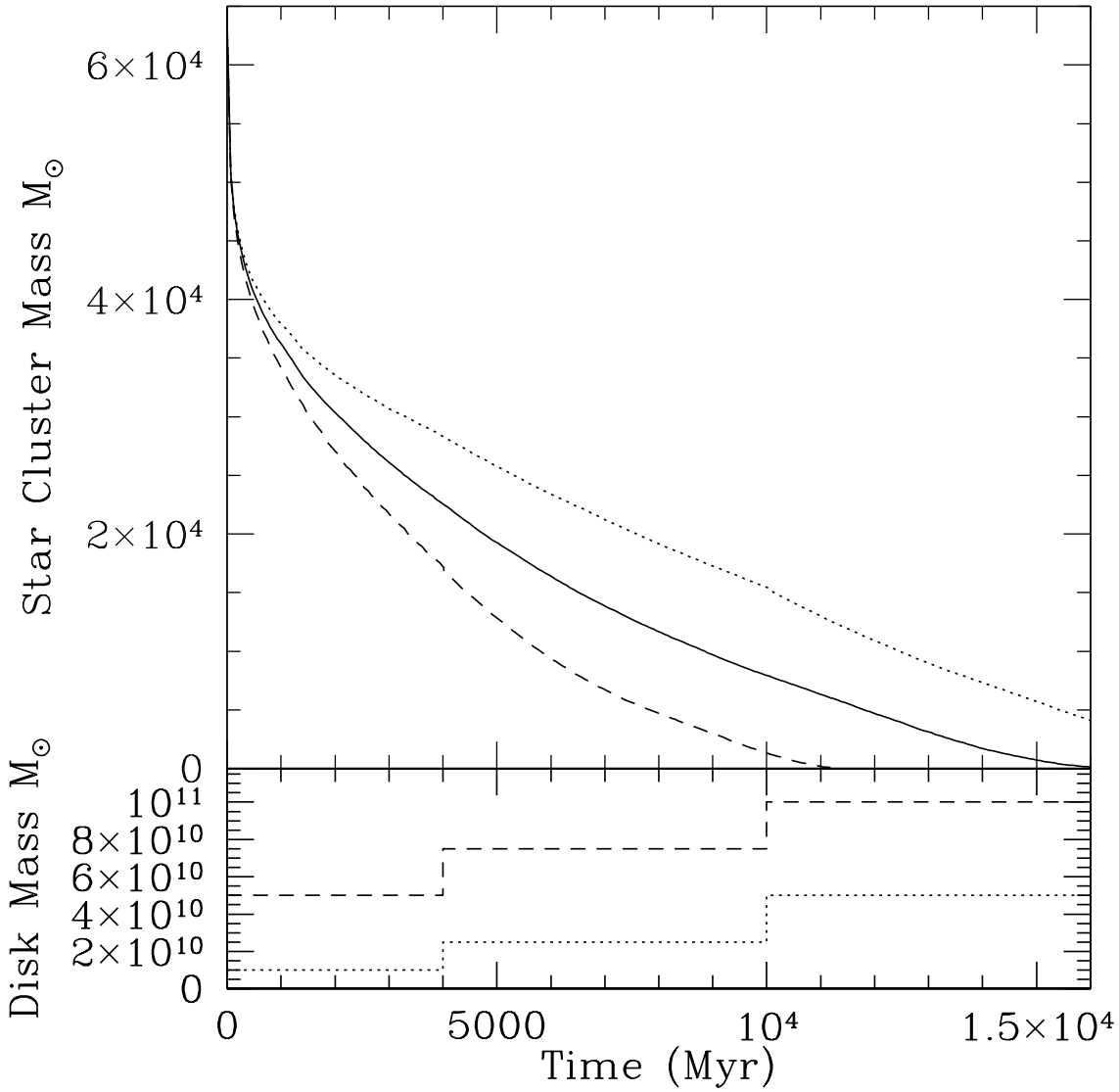

Figure 6.7 Star cluster mass vs. time for different evolution scenarios. The accretion events experienced by the host galaxy can determine the survival or dissolution of a satellite star cluster. The lower panel displays the evolution of the disk mass that increases over time with discrete accretion events.

6.7 Galaxy Evolution and the Survival or Dissolution of a Star Cluster

At the present time NBODY6 does not allow for a dynamic host galaxy model. However, the first steps to include a time dependent potential have already been taken by Renaud et al. (2011). An exciting future perspective is to have upcoming versions of NBODY6 with a fully incorporated time dependent host galaxy potential.

Within the current framework of NBODY6, and in order to investigate the fate of a star cluster whose host galaxy grows with time, different simulations of star clusters evolving with different disk masses are combined together. These are the simulations presented in Section 6.3.

Two different pathways for the evolution of a star cluster are built. The first series of accretion events experienced by the host galaxy leads to the survival of the star cluster after a Hubble time. The second scenario, where mass accretion lead to a more massive disk than in the first case, brings the star cluster to a complete dissolution before a Hubble time.

In the first scenario a simulated star cluster evolves during 4 Gyr as the satellite of a host galaxy with a disk mass of $1 \times 10^{10} M_{\odot}$. At 4 Gyr the host galaxy undergoes an instantaneous accretion event that brings the mass of the disk to $2.5 \times 10^{10} M_{\odot}$. At 10 Gyr the host galaxy experiences a second accretion event that brings the host galaxy disk to a mass of $5 \times 10^{10} M_{\odot}$. In this scenario, after a Hubble time, the star cluster has more mass than a simulated star cluster that evolves for a Hubble time in a galaxy with a constant disk mass of $5 \times 10^{10} M_{\odot}$, as expected.

In the second scenario the star cluster begins its evolution in a galaxy with a disk mass of $5 \times 10^{10} M_{\odot}$, at 4 Gyr the disk mass increases to $7.5 \times 10^{10} M_{\odot}$ and at 10 Gyr it increases again to become $10 \times 10^{10} M_{\odot}$. The simulated star cluster is fully dissolved before a Hubble time due to the enhanced mass loss rates induced by these series of accretion events that built a more massive disk. Note that during this exercise the geometrical parameters of the disk are kept constant $a = 4$ and $b = 0.5$ kpc.

The evolution of the total mass of the star cluster as a function of time in the two scenarios of accretion undergone by the host galaxy described above are given in Figure 6.7. In addition to these two accreting models the mass evolution of a star cluster evolving around a disk with a constant mass of $5 \times 10^{10} M_{\odot}$ is also plotted. This exercise shows how different accretion histories can lead to different depletion rates of satellite star clusters.

6.8 Final Remarks

The simulations presented in this work show that star clusters experience first hand the merger and accretion history of their host galaxy. The mass of the host galaxy disk plays an important and measurable role in the evolution of satellite star clusters, by affecting their mass loss rates and thus their structural parameters. The N-body models of star clusters have shown that the different masses and geometries of the host galaxy disk generally adopted in the literature lead to different substructure within the inner 15 kpc of the galactic center. The mass and geometry of the disk affect directly the depletion rates of satellite stellar systems in a similar manner as dark matter halos are affected (D'Onghia et al. 2010).

Assuming a constant disk mass over a Hubble time can lead to an overestimate (or underestimate) of the mass of the star cluster, that is depending on the merger and accretion history of the host galaxy.

Table 6.2: **Parameters of Models Executed.** Column 1 gives the model label; Column 2: bulge mass in solar masses; Column 3: disk mass in solar masses; Column 4: Miyamoto disk scale length a; Column 5: Miyamoto scale height b; Column 6: Galactocentric distance; Column 7: half-mass relaxation time (t_{rh}); Column 8 time when the star cluster has only 10% of the initial mass left $t_{10\%}$ – Columns 7 and 8 are proxies for the dissolution time.

Label	Bulge Mass	Disk Mass	a	b	R_{GC}	t_{rh}	$t_{10\%}$
	$M_\odot$	$M_\odot$	kpc	kpc	kpc	Gyr	Gyr
(1)	(2)	(3)	(4)	(5)	(6)	(7)	(8)
1	1.5×10^{10}	5×10^{10}	0.4	0.5	4	0.1	0.3
2	1.5×10^{10}	5×10^{10}	0.4	0.5	6	1.1	7.2
3	1.5×10^{10}	5×10^{10}	0.4	0.5	8	2.6	–
4	1.5×10^{10}	5×10^{10}	0.4	0.5	10	4.5	–
5	1.5×10^{10}	5×10^{10}	0.4	0.5	12.5	6.6	–
6	1.5×10^{10}	5×10^{10}	0.4	0.5	15	8.6	–
7	6.5×10^{10}	0	–	–	6	8.7	6.1
8	1.5×10^{10}	1.0×10^{10}	4.0	0.5	6	2.6	16.8
9	1.5×10^{10}	2.5×10^{10}	4.0	0.5	6	2.3	15.3
10	1.5×10^{10}	5.0×10^{10}	4.0	0.5	6	1.7	11.0
11	1.5×10^{10}	7.5×10^{10}	4.0	0.5	6	1.2	6.8
12	1.5×10^{10}	10×10^{10}	4.0	0.5	6	0.9	4.8
13	1.5×10^{10}	5×10^{10}	4.0	0.5	4	0.9	5.1
14	1.5×10^{10}	5×10^{10}	4.0	0.5	8	2.8	–
15	1.5×10^{10}	5×10^{10}	4.0	0.5	10	4.0	–
16	1.5×10^{10}	5×10^{10}	4.0	0.5	12.5	5.6	–
17	1.5×10^{10}	5×10^{10}	4.0	0.5	15	7.2	–
18	1.5×10^{10}	5×10^{10}	8.0	0.5	4	1.4	9.2
19	1.5×10^{10}	5×10^{10}	8.0	0.5	6	2.3	14.5
20	1.5×10^{10}	5×10^{10}	8.0	0.5	8	3.1	18.6
21	1.5×10^{10}	5×10^{10}	8.0	0.5	10	3.9	22.8
22	1.5×10^{10}	5×10^{10}	8.0	0.5	12.5	5.0	–
23	1.5×10^{10}	5×10^{10}	8.0	0.5	15	6.3	–

7

Conclusions and Future Work

7.1 Conclusions

The main conclusions of this thesis are summarized below:

- We have validated an observational method that uses HST data in two bands to find Ultra-Compact Dwarfs and Extended Star Clusters. Combining structural parameters derived with high resolution data with magnitudes and color is a solid method to discover new compact stellar systems.

- The method above was confirmed with Gemini spectroscopy of UCDs in the fossil group NGC 1132 as part of this thesis and with Keck spectroscopy in the case of the Coma cluster. The spectroscopic confirmation of UCDs in Coma was carried out by an independent group.

- By analyzing the large number of UCDs present in the Coma cluster we were able to determine that UCDs were present at the bright tip of *both* subpopulations of globular clusters. Previous observations have reported UCDs only on *either* the bright tip of the red subpopulation or the blue subpopulation of globular clusters.

- We find that UCDs also seem to follow the mass-metallicity relation of the brightest globular clusters. UCDs are not circumscribed to galaxy clusters as previously thought. This thesis supports the hypothesis recently put forward that UCDs are likely to be a common occurrence in all environments with large globular cluster systems.

- We discovered and spectroscopically confirmed a particularly bright UCD with the characteristics similar to those of compact elliptical galaxies.

- This work shows that UCDs can be used as test particles to determine the dynamical properties of galaxy groups or other galaxies out to a distance of 100 Mpc. Globular clusters, and planetary nebulae, have been used as test particles to derive the dynamical properties of galaxies at closer distances.

- By running advanced N-body simulations we established a new relation: the scale size of star clusters is proportional to the hyperbolic tangent of the galactocentric distance.

- These simulations also show that the half-mass radius of individual star clusters varies significantly over a Hubble time. Size measurements carried out today are rarely indicative of the early size of star clusters.

- Extended star clusters, such as the ones observed in Chapters 2 and 3, and simulated in Chapter 5 can form and evolve in the outer regions of Milky-Way type galaxies.

- A series of N-body simulations allowed us to derive a relationship between disk mass and star cluster dissolution. We show that the dissolution time of a star cluster is inversely proportional to disk mass.

7.2 Future Work

With a new mindset, and combining high resolution HST data with spectroscopy obtained with 8m class telescopes we can now build the true fundamental relations of compact stellar systems. The existing HST public archive has a very interesting data set of elliptical galaxies with hundreds of globular clusters and compact elliptical galaxies as their satellites. Hundreds of UCDs candidates are waiting to be discovered by analyzing existing HST data. Photometric and size information of these systems derived with HST data can be combined with spectroscopy to obtain metallicities, ages and mass-to-light ratios. The spectroscopic work is important. As pointed out recently by Brüns & Kroupa (2012) only one fifth of all published Ultra-Compact Dwarfs have been so far spectroscopically confirmed. That is more than 600 objects in need of spectroscopic follow-up.

The brightest UCDs have similar characteristics to compact elliptical galaxies, and as pointed out by Ferrarese et al. (2012) the study of UCDs will provide new insights into the origin of compact, high surface brightness systems which to date remains unexplained.

7.2.1 HST Observing Programs

During this thesis we collaborated in two HST observing proposals, one with W. E. Harris (McMaster University) and the second one with M. G. Lee. (Seoul National University). HST GO program 12532 approved in Cycle 19 (PI Harris) has recently acquired WFC3 + ACS data of globular clusters in the halo of Messier 87. This program is aimed at measuring precise structural parameters of globular clusters in the M87 halo over a large range of galactocentric distances. Ten fields at five different distances from the center of M87 (0, 2.36′, 6.56′, 11.12.36′, 16.5′) will be analysed as part of this program. Each distance is imaged with both WFC3 and ACS. For the first time the trend of globular cluster size vs. galactocentric distance will be analyzed with a homogenous dataset over 80 kpc. This program will derive effective radii, luminosities, colors, and concentration parameters for over 4200 globular clusters in M87. The results of this program can be combined with NGC 6822 data, Milky Way data and extended modelling of Chapter 5 to explore a size vs. R_{gc} relation independent of host galaxy type.

A second proposal to obtain the structural parameters of the Intracluster Globular Cluster population of the Virgo cluster was also submitted to the HST TAC (PI Lee) but not yet approved; this project will be resubmitted in future cycles. The limited sample of Intergalactic Globular Clusters reported by Williams et al. (2007a, 2007b) have tidal radii larger than the typical Galactic globular cluster. A larger than normal tidal radii for a globular cluster shows that it has evolved in a benign tidal field. Intracluster Globular Clusters have spent a significant (yet unknown) fraction of their lifetimes free of disk and bulge shocking, a primary physical mechanism that shapes star cluster size scales and the globular cluster luminosity function (Gnedin & Ostriker 1997, Chapter 6). One of the possible precursors of globular clusters are dwarf galaxies that have been downsized by losing their stars to a parent galaxy due to gravitational interactions (Böker 2008). Intracluster Globular Clusters can actually represent these primordial stellar systems with scale sizes similar to those of extended star clusters and Ultra Compact Dwarfs.

7.2.2 Numerical Simulation of an Entire Globular Cluster System

Sophisticated N-body simulations are now able to match observations of star clusters, in many cases, star by star. Observed color-magnitude diagrams can be matched by simulated ones where each star has very well determined evolution thanks to computer models. A good example is given by Hurley et al. (2005) with a detailed model of the open cluster M67. By matching each star on a present day color-magnitude diagram N-body simulations tell us the initial mass function (IMF) of the star cluster.

It is now the time to carry out numerical simulations of an entire globular cluster system. The Galactic globular cluster system, for instance, has ∼150 members (Harris 2010). Detailed numerical simulations of 150 star clusters are now within reach of modern computing facilities, in a very realistic timescale. Thus, a complete simulation of the Galactic globular cluster system can, for the first time, be carried out within a year. One current assumption to explain color bimodality is a different metallicity of globular clusters. Is this different metallicity a primordial metallicity difference? Or does the metallicity bimodality arise during a Hubble time of evolution? Would the standard color bimodality of globular cluster systems appear naturally even in a system that has the same initial metallicity for all clusters? Or would the only way to recover the bimodal color distribution be to start with a bimodal metallicity distribution in the simulated clusters? These simulations can help settle the current debate on color-metallicity relations for globular cluster systems, as discussed in Chapter 1.

We can now couple results from scales that have not been coupled before. The impact of stellar and dynamical evolution within individual globular clusters can be linked to the overall properties observed for the ensemble of globular clusters belonging to a galaxy.

7.2.3 Primordial Binaries

The impact of the primordial binary fraction on the structural parameters of star clusters would be interesting to explore in detail in the future. We saw in Chapter 5 that having up to 20% of primordial binaries does not have an important impact on the results presented in this thesis. But what is the binary fraction threshold above which binaries will generate a significantly larger radius or different mass-loss rates? Simulations with larger number of binaries take much longer to run than the standard simulations presented in this work.

7.2.4 A Million Particle Simulation

As mentioned above, N-body simulations can now match observations of star clusters star by star. Simulations of star clusters have been historically limited by the existing computer power. Initial simulations of star clusters were carried out with barely 25 star-particles (von Hoerner 1975). Today, simulations with $N = 150,000$ star particles can be carried out in about three weeks time. These are simulations that have an initial mass of $M \sim 10^5 M_\odot$ but final masses of $M \sim 10^4 M_\odot$ or less.

With the new computer infrastructure now available within Australia, simulations with much larger particle numbers and thus more massive star clusters are within reach. A million particle simulation that simulates a large globular cluster, star by star, can be

expected to be performed with gSTAR, within the time frame of this fellowship. Such a large simulation will help us understand the dynamical evolution of systems at the fundamental plane boundary between globular clusters and Ultra-Compact Dwarfs. With this simulation, the evolution over a Hubble time of the mass and half-mass radius of the system can be derived.

The simulations with a realistic galaxy potential presented here yield, after a Hubble time of evolution, star clusters with the characteristics observed today. Further exploring the initial values used for the set-up of the simulations is a natural follow-up to this work. The initial values for the effective radius and concentration parameters can have an impact on the observed size distribution function (Harris et al. 2010). We will also aim to make a comparison with the prescriptions of star cluster evolution put forward by Alexander & Gieles (2012).

New computing capabilities enabled by GPUs will allow simulations with a larger initial number of star-particles. This should demonstrate that massive clusters can survive at small galactocentric distances, i.e. $R_{GC} = 4$ kpc. Such simulations will improve our understanding of the initial size and mass distribution of globular clusters and test the theories that claim that globular clusters are the remnant nuclei of disk galaxies (Böker 2008).

Bibliography

Aarseth, S. J. 1999, PASP, 111, 1333

Aarseth, S. J. 2003, Gravitational N-body Simulations: Tools and Algorithms (Cambridge Monographs on Mathematical Physics). Cambridge University Press, Cambridge

Aguilar, L., Hut, P. & Ostriker, J. P. 1988, ApJ, 335, 720

Alamo-Martínez, K. A., West, M. J., Blakeslee, J. P. et al. 2012, A&A, 546, 15

Alexander, P. & Gieles, M. 2012, MNRAS, 422, 3415

Bailin, J. & Harris, W. E. 2009, ApJ, 695, 1082

Barsdell, B. R., Barnes, D. G., Fluke, C. J. 2010, MNRAS, 408, 1936

Bastian, N. & Goodwin, S. P. 2006, MNRAS, 369, L9

Baumgardt, H. 2001, MNRAS, 325, 1323

Baumgardt, H. & Makino, J. 2003, MNRAS, 340, 227

Baumgardt, H. & Makino, J., Ebisuzaki, T. 2004, ApJ, 613, 1133

Baumgardt, H. & Kroupa, P. 2007, MNRAS, 380, 1589

Baumgardt, H., Parmentier, G., Mark, G., Vesperini, E. 2010, MNRAS, 401, 1832

Bica, E., Bonatto, C. Barbuy, B., Ortolani, S. 2006, A&A, 450, 105

Binney, J. & Tremaine, S. Galactic Dynamics, Princeton University Press, Princeton, New Jersey, 1987, p. 514.

Bekki, K., Couch, W. J., Drinkwater, M. J., & Gregg, M. D. 2001, ApJ, 557, L39

Bekki, K., Couch, W. J., Drinkwater, M. J., & Shioya, Y. 2003, MNRAS, 344, 399

Bertin, E., & Arnouts, S. 1996, A&AS, 117, 393

Bertin, G., & Varri, A. L. 2008, ApJ, 689, 1005

Billett, O. H., Hunter, D. A., & Elmegreen, B. G. 2002, AJ, 123, 1454

Binney, J. & Tremaine, S. Galactic Dynamics, Princeton University Press, Princeton, New Jersey, 1987, p. 514.

Blakeslee, J. P. & Barber DeGraaff, R. 2008, AJ, 136, 2295

Blakeslee, J. P. & Tonry, J. L. 1995, ApJ, 442, 579

Böker, T. 2008, ApJ, 672, L111

Brodie, J. P. & Larsen, S. S. 2002, AJ, 124, 1410

Brodie, J. P., Romanowsky, A. J., Strader, J., Forbes, D. A. 2011, AJ, 142, 199

Brodie, J. P., Usher, C., Conroy, C. et al. 2012, ApJ, 759, L33

Brüns, R. C. & Kroupa, P. 2012, A&A, 547, 65

Bullock, J. S. & Johnston, K. V. 2005, ApJ, 635, 931

Buzzoni, A. 2005, MNRAS, 361, 725

Carter, D., et al. 2008, ApJS, 176, 424

Chiboucas, K., et al. 2009, BAAS, 41, 234

Chiboucas, K. et al. 2010, ApJ, 723, 251

Chiboucas, K., Tully, R. B., Marzke, R. O. et al. 2011, ApJ, 737, 86

Chilingarian I. V. & Mamon, G. A. 2008, MNRAS, 385, L83

Church, R. P., Tout, C. A., Hurley, J. R. 2009, PASA, 26, 92

Cid Fernandes, R., Mateus, A., Sodré, L., Stasinzka, G., & Gomes, J. M., 2005, MNRAS, 358, 363

Cocatto, L., O. Gerhard, M., Arnaboldi, P. Das, et al. 2009, MNRAS, 394, 1249

Colless, M. 2001, Coma Cluster in Encyclopedia of Astronomy and Astrophysics, Nature Publishing Group, Basingstoke, UK

Collobert, M., Sarzi, M., Davies, R. L., Kuntschner, H. & Colless, M. 2006, MNRAS, 370, 1213

Dabringhausen, J., Hilker, M., & Kroupa, P. 2008, MNRAS, 386, 864

Da Costa, G. S., Grebel, E. K., Jerjen, H., Rejkuba, M., & Sharina, M. E. 2009, AJ, 137, 4361

Dariush, A., Khosroshahi, H. G., Ponman, T. J., Pearce, F., Raychaudhury, S., & Hartley, W. 2007, MNRAS, 382, 433

Da Rocha, C., Mieske, S., Georgiev, I. Y., Hilker, M., Ziegler, B. L., & Mendes de Oliviera, C. 2011, A&A, 525, A86

Davis, D. S., Richer, H. B., Anderson, J., Brewer, J., Hurley, J., et al. 2008, AJ, 135, 2155

Davoust, E., Sharina, M. E., & Donzelli, C. J. 2011, A&A, 528, 70

De Grijs, R., Li, C., Zheng, Y., Deng, L., Hu Y., Kouwenhoven, M. B. N., Wicker, J. E. 2013, ApJ, 765, 4

Díaz-Giménez, E., Zandivarez, A., Proctor, R., Mendes de Oliveira, C., & Abramo, L. R. 2011, A&A, 527, A129

Dirsch, B. et al. 2003, AJ, 125, 1908

Djorgovski, S. & Meylan, G. 1994, AJ, 108, 1292

D'Onghia, E., Springel, V., Hernsquist, L., & Keres, D. 2010, ApJ, 709, 1138

Drinkwater, M. J., Jones, J. B., Gregg, M. D., Phillipps, S. 2000, PASA, 17, 227

Drinkwater, M. J. et al. 2003, Nature, 423, 519

Dutra, C. M. & Bica, E. 2000, A&A, 359, L9

Evstigneeva, E. A., Drinkwater, M. J., Jurek, R., Firth, P., Jones, J. B., Gregg, M. D., & S. Phillipps, S. 2007, MNRAS, 378, 1036

Evstigneeva, E. A., Gregg, M. D., Drinkwater, M. J., & Hilker, M 2007, AJ, 133, 1722

Evstigneeva, E. A. et al. 2008, AJ, 136, 461

Faber, S. M. & Jackson, R. E. 1976, ApJ, 204, 668

Ferrarese, L., Côté, P. et al. 2012, ApJS, 200, 4

Forbes, D. A. et al. 2008, MNRAS, 389, 1924

Francis, K. J., Drinkwater, M. J., Chilingarian, I. V., Bolt, A. M. & Firth, P 2012, MNRAS, 425, 325

Geha, M., Wilman, B., Simon, J. D., et al. 2009, ApJ, 692, 1464

Gieles, M. et al. 2007, MNRAS, 376, 809

Gieles, M., Baumgardt, H., Heggie, D. C., Lamers, H. 2010, MNRAS, 408, L16

Gieles, M., Heggie, D. C., & Zhao, H 2011, MNRAS, 413, 2509

Giersz, M. 1998, MNRAS, 298, 1239

Giersz, M., Heggie, D. C. 1994, MNRAS, 268, 257

Gierz, M. & Heggie, D. C. 1997, MNRAS, 286, 709

Gierz, M. & Heggie, D. C. 2011, MNRAS, 410, 2698

Gilmore, G., Wilkinson, M. I., Wyse, R. F. G. et al. 2007, ApJ, 663, 948

Gnedin, O. Y. & Ostriker, J. P. 1997, ApJ, 474, 223

Gnedin, O. Y., & Ostriker, J. P. 1999, ApJ, 513, 626

Gómez, F. A., Helmi, A., Brown, A. G., & Li, Y-S. 2010, MNRAS, 408, 935

Goodwin, S. P. & Bastian, N. 2006, MNRAS, 373, 752

Graham, A. W. 2002, ApJ, 568, L13

Grevesse, N. & Sauval, A. J. 1998, Space Science Reviews, 85, 161

Hamada, T., et al. 2009, Computer Science Research and Development, 24, 21

Hammer, D. et al. 2010, ApJS, 191, 143

Harris, W. E. 1996, AJ, 112, 1487

Harris, W. E. 2009a, ApJ, 699, 254

Harris, W. E. 2009b, ApJ, 703, 939

Harris, W. E., Whitmore, B. C., Karakla, D., Okon, W., Baum, W. A., Hanes, D. A., & Kavelaars, J. J. 2006, ApJ, 636, 90

Harris, W. E., et al. 2009, AJ, 137, 3314

Harris, W. E., et al. 2010, MNRAS, 401, 1965

Harris, W. E. 2010, Philosophical Transactions of the Royal Society A: Mathematical, Physical and Engineering Sciences, 368, 889

Harris, W. E., Sills, A., Webb, J. J., Hurley, J. R. & Madrid, J. P. 2011, HST GO Program 12532, The Scale Sizes of Globular Clusters: Tidal Limits, Evolution, and the Outer Halo

Hasegan, M., et al. 2005, ApJ, 627, 203

Hau, G. K., et al. 2009, MNRAS, 394, L97

Heggie, D. C. & Hut, P. 2002, The Gravitational Million-Body Problem, Cambridge University Press, UK

Heggie, D.C. & Mathieu, R.D. 1986, in Hut P., McMillan S.L.W., eds., The Use of Supercomputers in Stellar Dynamics. Springer-Verlag, Berlin, p. 233

Hilker, M., Infante, L., Vieira, G., Kissler-Patig, M., Richtler, T. 1999, A&AS, 134, 75

Hilker, M. 2006, UCDs – A mix bag of objects, in ESO Astrophysics Symposia: Globular Clusters Guides to Galaxies, Springer, Berlin

Hodge, P. W. 1960, ApJ, 131, 351

Hodge, P. W. 1962, PASP, 74, 248

Hu, Y., Deng, L., de Grijs, R., Liu, Q., & Goodwin, S. P. 2010, ApJ, 724, 649

Hurley, J. R., Onno, O. R., Tout, C. A., 2000, MNRAS, 315, 543

Hurley, J. R., et al. 2005, MNRAS, 363, 293

Hurley, J. R. 2007, MNRAS, 379, 93

Hurley, J. R., Aarseth, S.J., Shara, M. M. 2007, ApJ, 665, 707

Hurley, J. R. 2008a, Lecture Notes in Physics, 760, The Cambridge N-body Lectures, Springer-Verlag, Berlin, p. 283

Hurley, J. R. 2008b, Lecture Notes in Physics, 760, The Cambridge N-body Lectures, Springer-Verlag, Berlin, p. 321

Hurley, J. R. & Bekki, K. 2008, MNRAS, 389, L61

Hurley, J. R. & Mackey, A. D. 2010, MNRAS, 408, 2353

Huxor, A. P., et al. 2005, MNRAS, 360, 1007

Hwang, N. et al. 2011, ApJ, 2011, 738, 58

Hypki, A. & Giersz, M. 2013, MNRAS, 429, 1221

Jones, L. R., Ponman, T. J., Horton, A., Babul, A., Ebeling, H. & Burke, D. J. 2003, MNRAS, 343, 627

Jordán, A. 2004, ApJ, 613, L117

Jordán, A., et al. 2005, ApJ, 634, 1002

Khosroshahi, H. G., Ponman, T. J. & Jones, L. R. 2007, MNRAS, 377, 595

King, I. R. 1962, AJ, 67, 471

King, I. R. 1966, AJ, 71, 64

Koekemoer, A. M., Fruchter, A. S., Hook, R. N., & Hack,W. 2002, in The 2002 HST Calibration Workshop: Hubble after the Installation of the ACS and the NICMOS Cooling System, ed. S. Arribas, A. Koekemoer, & B. Whitmore, Baltimore, STScI, 339

Kravstov, A. V. & Gnedin, O. Y. 2005, ApJ, 623, 650

Kroupa, P. 2001, MNRAS, 322, 231

Kundic, T. & Ostriker, J. P. 1995, ApJ, 438, 702

Kundu, A., Whitmore, B. C. et al. 1999, ApJ, 513, 733

Küpper, A. H., Kroupa, P., Baumgardt, H., Heggie, D. C. 2010a, MNRAS, 401, 105

Küpper, A. H., Kroupa, P., Baumgardt, H., Heggie, D. C. 2010b, MNRAS, 407, 2241

Küpper, A. H., Maschberger, T., Kroupa, P., Baumgardt 2011, MNRAS, 417, 2300

Laidler, V. et al. 2005, Synphot User's Guide, Version 5.0 (Baltimore, MD: STScI)

Lamb, D. Q., 2012, March issue of Scientific American, Supercomputers Can Save U.S. Manufacturing

Larsen, S. S. 1999, A&AS, 139, 393

Larsen, S. S., & Brodie, J. P. 2000, AJ, 120, 2938

Larsen, S. S. & Brodie 2003, ApJ, 593, 263

Larsen, S. S., et al. 2001, AJ, 121, 2974

Larsen, S. S., et al. 2008, MNRAS, 383, 263

Lee, M. G., et al. 2010, Science, 328, 334

Leitner, S. N. 2012, ApJ, 745, 149

Lintott, C. et al. 2011, MNRAS, 410, 166

Longmore, A. J. et al. 2011, MNRAS, 416, 465

Loubser, S. I., Sánchez-Blásquez, P., Sansom, A. E., & Soechting, I. K. 2009, MNRAS, 398, 133

Mack, J., et al. 2003, ACS Data Handbook, Version 2.0, Baltimore, STScI

Mackey, A. D., et al. 2006, ApJL, 653, L105

Mackey, A. D., & van den Bergh, 2005, MNRAS, 360, 631

Madrid, J. P., Harris, W. E., Blakeslee, J. P., Gómez, M. 2009, ApJ, 705, 237

Madrid, J. P., Graham, A. W., Harris, W. E., et al. 2010, ApJ, 722, 1707 (Paper I)

Madrid, J. P. 2011, ApJL, 737, L13 (Paper II)

Madrid, J. P., Hurley, J. R., Sippel, A. C. 2012, ApJ, 756, 167

Mahdavi, A., Geller, M. J., Bohringer, H., Kurtz, M. J. & Ramella, M. 1999, ApJ, 518, 69

Makino, J., Fukushige, T., Koga, M., Namura, K. 2003, PASJ, 55, 1163

Mardling, R. A., Lecture Notes in Physics, 760, The Cambridge N-body Lectures, Springer-Verlag, Berlin, p. 59

Masters, K., et al. 2010, ApJ, 715, 1419

McLaughlin, D. E. 2000, ApJ, 539, 618

McLaughlin, D. E. & Fall, S. M. 2008, ApJ, 679, 1272

Mendes de Oliveira, C. L. & Carrasco, E. R. 2007, ApJ, 670, L93

Mieske, S., et al. 2004, AJ, 128, 1529

Mieske, S., et al. 2006, AJ, 131, 2442

Mieske, S., et al. 2007, A&A, 472, 111

Mieske, S., et al. 2008, A&A, 487, 921

Mieske, S., Hilker, M., & Misgeld, I. 2012, A&A, 537, A3

Mikkola, S., Lecture Notes in Physics, 760, The Cambridge N-body Lectures, Springer-Verlag, Berlin, p. 31

Misgeld, I., Mieske, S., & Hilker, M. 2008, A&A, 486, 697

Misgeld, I. & Hilker, M. 2011, MNRAS, 414, 3699

Miyamoto, M. & Nagai, R. 1975, PASJ, 27, 533

Monachesi, A., et al. 2011, ApJ, 727, 55

Mulchaey, J. S. & Zabludoff, A. I. 1999, ApJ, 514, 133

Muñoz, R. R., Geha, M., Côté, P., et al. 2012, ApJ, 753, L15

Murray, N. 2009, ApJ, 691, 946

Nitadori, K. & Aarseth, J. S. 2011, MNRAS, 424, 545

Norris, M. A. & Kannappan, S. J. 2011, MNRAS, 414, 739

Odenkirchen, M. et al. 2001, ApJ, 548, L165

Ortiz-Gil, A., Guzzo, L., Schuecker, P., Böringer, H. & Collins, C. A. 2004, MNRAS, 348, 32

Paczynski, B. 1990, ApJ, 348, 485

Parmentier, G. & Grebel, E. K. 2005, MNRAS, 359, 615

Peng, E. W., et al. 2006, ApJ, 639, 95

Peng, E. W., et al. 2008, ApJ, 703, 42

Peng, E. W. et al. 2009, ApJ, 703, 42

Peng, C. Y., Ho, L. C., Impey, C. D., Rix, H-W. 2002, AJ, 124, 266

Peñarrubia, J., Belokorov, V., Evans, N. W., et al. 2010, MNRAS, 408, L26

Phillipps, S. et al. 2001, ApJ, 560, 201

Pisani, A., Ramella, M. & Geller, M. 2003, AJ, 126, 1677

Plummer, H. C. 1911, MNRAS, 71, 460

Pols, O., Hurley, J., Tout, C. 1998, MNRAS, 298, 525

Ponman, T. J., Allan, D. J., Jones, L. R., Merrifield, M., McHardy, I. M., Lehto, H. J. & Luppino, G. A. 1994, Nature, 369, 462

Praagman, A., Hurley, J., Power, C. 2010, New Astronomy, 15, 46

Price, J. et al. 2009, MNRAS, 397, 1816

Puzia, T. H., Zepf, S. E., Kissler-Patig, M., Hilker, M., Minniti, D. & Goudfrooij, P. 2002, A&A, 391, 453

Read, J. I., Wilkinson, M. I., Evans, N. W., Gilmore, G., Kleyna, J. T. 2006, MNRAS, 366, 429

Read, J. I., Wilkinson, M. I., Evans, N., Gilmore, G., & Kleyna, J. T. 2006, MNRAS, 367, 387

Renaud, F., Gieles, M., & Bioly, M. C. 2011, MNRAS, 418, 759

Romanowsky, A. J., Strader, J., Spitler, L. R., Johnson, R., Brodie, J. P., Forbes, D. A., Ponman, T. 2012, AJ, 137, 4956

Sales, L. V., Navarro, J. F., Lambas, D. G., White, S. D. M., Croton, D. J. 2007, MNRAS, 382, 1901

Sérsic, J. L. 1968, Atlas de Galaxias Australes (Córdoba: Observatorio Astronómico, Univ. Nac. Córdoba)

Shara, M. M., et al. 2009, AJ, 138, 402

Sirianni, M. et al. 2005, PASP, 117, 1049

Sirianni, M., Gilliland, R., & Sembach, K. 2006 Technical Instrument Report ACS 2006-02, Baltimore, STScI

Sippel, A. C., Hurley, J. R., Madrid, J. P., Harris, W. E. 2012, MNRAS, 427, 167

Skrutskie, M., F., et al. 2006, AJ, 131, 1163

Spergel, D. N., et al. 2003, ApJSS, 148, 175

Spitler, L. R. et al. 2006, AJ, 132, 1593

Spitzer, L. 1958, ApJ, 127, 17

Spitzer, L., & Hart, M. H. 1971, ApJ, 164, 399

Spitzer, L., & Thuan, T. X. 1972, ApJ, 175,31

Spitzer, L. 1987, Dynamical Evolution of Globular Clusters, ed. J. P. Ostriker (Princeton: Princeton Univ. Press)

Springel, V., et al. 2005, Nature, 435, 629

Strader, J., Brodie, J. P., Spitler, L., & Beasley, M. A. 2006, AJ, 132, 1593

Strader, J., Romanowsky, A. J., Brodie, J. P., Spitler, L. R. et al. 2011, ApJS, 197, 33

Thomas, D., Maraston, C., Bender, R. 2003, MNRAS, 339, 897

Tonini, C. 2013, ApJ, 762, 39

Tonry, J. L. 2001, ApJ, 546, 681

Toomre, A. 1963, ApJ, 138, 385

Toomre, A. & Toomre, J. 1972, ApJ, 178, 623

Tout, C. A., Lecture Notes in Physics, 760, The Cambridge N-body Lectures, Springer-Verlag, Berlin, p. 297 van de Ven G. et al. 2006, A&A, 445, 513

Vanbeveren, D., De Donder, E., van Bever, J., van Rensbergen, W., De Loore, C. 1998, New Astronomy, 3, 443

van den Bergh, S., Morbey, C., & Pazder, J. 1991, ApJ, 375, 594

Vesperini, E. & Heggie, D. C. 1997, MNRAS, 289, 898

Vink, J. S., de Koter, A., & Lamers, H. 2000, A&A, 362, 295

von Hoerner, S. 1957, ApJ, 125, 451

Webb, J. J., Harris, W. E., Sills, A. & Hurley, J. R. 2013, ApJ, 764, 124

Wehner, E. M. H. & Harris, W. E. 2007, ApJ, 668, L35

Wehner, E. M. H., et al. 2008, ApJ, 681, 1233

West, M. J., Côté, P., Marzske, R. O., Jordán, A. 2004, Nature, 427, 31

White, S. D. M. & Rees, M. J. 1978, MNRAS, 183,

Williams, B. F. et al. 2007a, ApJ, 654, 835

Williams, B. F. et al. 2007b, ApJ, 656, 756

Worthey, G., Faber, S. M., Gonzalez, J. J. & Burstein, D. 1994, ApJS, 94, 687

Wright, E. L. 2006, PASP, 118, 1711

Xue, X. X., et al. 2008, ApJ, 684, 1143

Xue, Y-J. & Wu, X-P 2000, ApJ, 538, 65

Yoon, S-J, Yi, S. K., Lee, Y-W., 2006, Science, 311, 1129

Zinn, R. & West, M. J. 1984, ApJS, 55, 45

A

Example Input file for simulations

```
1 1000000.0
KSTART TCOMP
100000 1 100 20017 400 1
N FIX NCRIT NRAND NNBMAX NRUN
0.02 0.02 0.15 2.0 10.0 12000.0 1.0E-02 8.0 0.6
ETAI ETAR RS0 DTADJ DELTAT TCRIT QE RBAR ZMBAR
2 0 0 0 1 0 1 5 0 0
0 3 0 3 2 1 0 1 3 7
1 0 2 0 0 2 2 1 0 1
1 0 2 2 1 0 0 2 0 3
0 0 0 0 0 0 0 0 0 0
OPTIONS 1-50
2.0E-06 0.0001 0.2 1.0 1.0E-06 0.001
DTMIN RMIN ETAU ECLOSE GMIN GMAX
2.3 50.0 0.1 5000 0 0.001 0.0 50.0
ALPHAS BODY1 BODYN NBIN0 NHI0 ZMET EPOCH0 DTPLOT
0.5 0.0 0.0 6.5
Q VXROT VZROT RTIDE
1.5D+10 5.0D+10 4.0 0.5 220.0 8.5 6.0 0.0 0.0 -10.0 200.0 100.0
GMG DISK A B VCIRC RCIRC RG(x,y,z) VG(x,y,z)
0.0 1.0 1.0 1.0
MP AP MPDOT TDELAY
0.0005 -2.0 1.0 250.0 1 0 0
SEMI ECC RATIO RANGE NSKIP IDORM ICIRC
```

Definition of physical parameters and numerical values in the example input file. From the `define.f` subroutine in `NBODY6` (Aarseth 2003).

```
KSTART  1 Control index (1: new run; >1: restart; 3, 4, 5: new params).
TCOMP   1000000.0 Maximum CPU time in minutes (saved in CPU).
N       100000 Number of objects ($N_s + 2*N_b$; singles + 3*NBIN0 $<$ NMAX).
NFIX    1 Output frequency of data save or binaries (options 3 & 6).
NCRIT   100 Final particle number (alternative termination criterion).
NRAND   20017 Random number sequence skip.
NNBMAX  400 Maximum number of neighbours ($<$ LMAX - 5).
NRUN    1 Run identification index.

ETAI    0.02 Time-step parameter for irregular force polynomial.
ETAR    0.02 Time-step parameter for regular force polynomial.
RS0     0.15 Initial radius of neighbour sphere (N-body units).
DTADJ   2.0  Time interval for parameter adjustment (N-body units).
DELTAT  10.0 Output time interval (N-body units).
TCRIT   12000 Termination time (N-body units). Set to 22000 when evolving
        past a Hubble time
QE      1.0E-02 Energy tolerance (restart if $DE/E > 5*QE$ \& KZ(2) $>$ 1).
RBAR    8.0 Virial cluster radius in pc (set = 1 for isolated cluster).
ZMBAR   0.6 Mean mass in solar units (=1.0 if 0; final depends on \#20).

Options KZ(J)

 1  2 COMMON save unit 1 (=1: 'touch STOP'; =2: every 100*NMAX steps).
 2  0 COMMON save unit 2 (=1: at output; =2: restart if DE/E > 5*QE).
 3  0 Basic data unit 3 at output time (unformatted, frequency NFIX;
       =1/2: standard /and tail; =3: tail only; >3: cluster + tail).
 4  0 Binary diagnostics on unit 4 (# threshold levels = KZ(4) < 10).
                                  (currently suppressed in ksint.f.)
 5  1 Initial conditions (if#22 =0 then read initial spatial dist from
   file ; =0: uniform & isotropic sphere);
          =1: Plummer; =2: two Plummer models in orbit, extra input;
          =3: massive perturber and planetesimal disk, extra input;
```

```
          =4: massive initial binary, extra input: A, E, M1, M2;
          =5: Jaffe model;
         >=6: Zhao BH cusp model, extra input if #24 < 0: ZMH, RCUT.
 6  0 Significant & regularized binaries at main output (=1, 2, 3 & 4).
 7  1 Lagrangian radii (>0: RSCALE; =2, 3, 4: output units 6, 7, 12);
          >=2: Lagrangian radii for two mass groups on unit 31 & 32;
          >=2: harmonic radii for three mass groups on unit 6;
           =5: density, rms velocity & mean mass on unit 26, 27 & 36;
           =6: pairwise values of mean mass and radii on unit 28.
 8  5 Primordial binaries (=1 & >=3; >0: BINOUT; >2: BINDAT; >3: HIDAT;
                          =4: Kroupa 1995 period distribution).
 9  0 Individual bodies on unit 6 at main output (MIN(5**KZ9,NTOT)).
10  0 Diagnostic KS output (>0: begin KS; >1: end; >=3: each step).
11  0 (reserved for post-Newtonian code NBODY7).
12  3 HR diagnostics of evolving stars (interval DTPLOT).
13  0 Interstellar clouds (=1: constant velocity; >1: Gaussian).
14  3 External force (=1: standard tidal field; =2: point-mass galaxy;
       =3: point-mass + disk + halo + Plummer; =4: Plummer model).
15  2 Triple, quad, chain (#30 > 0) or merger search (>1: full output).
16  1 Updating of regularization parameters (>0: RMIN, DTMIN & ECLOSE);
             >1: RMIN expression based on core radius (experimental);
             >2: modify RMIN for GPERT > 0.05 or < 0.002 in chain.
17  0 Modification of ETAI, ETAR (>=1) and ETAU (>1) by tolerance QE.
18  1 Hierarchical systems (=1: diagnostics; =2: primordial; =3: both).
19  3 Mass loss (=1: old supernova scheme; =3: Eggleton, Tout & Hurley).
20  7 Initial mass function (=0: Salpeter type using ALPHAS; =1: Scalo;
      =2, 4, 6 and 7 also: Kroupa; =3, 5: Eggleton; > 1: primordial binaries).
21  1 Extra output (>0: MODEL #, TCOMP, DMIN, AMIN; >1: NESC by JACOBI).
22  0 Initial m, r, v on #10 (=1: output; >=2: input; >2: no scaling);
      =3: input of stellar parameters on unit 12 (routine INSTAR);
      =4: input from mcluster.c code on fort.10 (also NBIN0 > 0);
      =-1: astrophysical input (M_sun, km/s, pc) on unit #10.
23  2 Escaper removal (>1: diagnostics in file ESC with V_inf in km/s);
                    >=3: initialization & integration of tidal tail.
24  0 Initial conditions for subsystem (M,X,V routine SCALE; KZ(24)= #);
```

```
                    <0: ZMH & RCUT (N-body units) Zhao model (#5>=6).
25  0 Partial reflection of KS binary orbit (GAMMA < GMIN; suppressed).
26  2 Slow-down of two-body motion (>=1: KS; >=2: chain; =3: rectify).
27  2 Tidal effects (=1: sequential; =2: chaos; =3: GR energy loss);
                  =-1: collision detector, no coalescence, #13 < 0.
28  1 GR radiation for NS & BH binaries (with #19 = 3; choice of #27);
                  =3: and #5 >= 6: input of ZMH = 1/SQRT(2*N).
29  0 Boundary reflection for hot system (suppressed).
30  1 Multiple regularization (=1: all; >1: BEGIN/END; >2: each step);
                         =-1: CHAIN only; =-2: TRIPLE & QUAD only.
31  1 Centre of mass correction after energy check.
32  0 Increase of output intervals (based on single particle energy).
33  2 Histograms at main output (>=1: STEP; =2: STEPR, NBHIST & BINARY).
34  2 Roche-lobe overflow (=1: Roche & Synch; =2: Roche & BSE synch).
35  1 Time offset (global time from TTOT = TIME + TOFF; offset = 100).
36  0 Step reduction for hierarchical systems (suppressed).
37  0 Neighbour additions in CHECKL (>0: high-velocity; >1: all types).
38  2 Force polynomial corrections (=0: I > N; >0: single particles).
39  0 No unique density centre (skips velocity modification of RS(I)).
40  3 Neighbour number control (=1: increase if <NNB>  <  NNBMAX/2);
              >=2: fine-tuning at NNBMAX/5; =3: reduction of NNBMAX.

41-50  0 Currently free.

DTMIN   2.0E-06 Time-step criterion for regularization search.
RMIN    0.0001 Distance criterion for regularization search.
ETAU    0.2 Regularized time-step parameter (6.28/ETAU steps/orbit).
ECLOSE  1.0 Binding energy per unit mass for hard binary (positive).
GMIN    1.0E-06 Relative two-body perturbation for unperturbed motion.
GMAX    0.001 Secondary termination parameter for soft KS binaries.

ALPHAS  2.3 Power-law index for initial mass function (used if #20 < 2).
BODY1   50.0 Maximum particle mass before scaling (KZ(20): solar mass).
BODYN   0.1 Minimum particle mass before scaling.
NBIN0   5000 Number of primordial binaries (for IMF2 with KZ(20) > 1).
```

```
NHI0    0 Primordial hierarchies (may be needed in IMF if > 0).
ZMET    0.001 Metal abundance (in range 0.03 - 0.0001).
EPOCH0  0.0 Evolutionary epoch (in 10**6 yrs; NB! < 0 for PM evolution).
DTPLOT  50. 0 Plotting interval for HRDIAG (N-body units;
        not to be lower than DELTAT).

Q       0.5 Virial ratio (Q = 0.5 for equilibrium).
VXROT   0.0 XY-velocity scaling factor (> 0 for solid-body rotation).
VZROT   0.0 Z-velocity scaling factor (not used if VXROT = 0).
RTIDE   6.5 Unscaled tidal radius (#14 >= 2; otherwise copied to RSPH2).
        the tidal radius gets multiplied by RBAR 6.5x8=52pc

GMG     1.5D+10 Point-mass galaxy (solar masses).
DISK    5.0D+10 Mass of Miyamoto disk (solar masses).
A       4.0 Softening length in Miyamoto potential (in kpc).
B       0.5 Vertical softening length (kpc).
VCIRC   220 Galactic circular velocity (km/sec) at RCIRC (=0: no halo)
RCIRC   8.5 Central distance for VCIRC with logarithmic potential(kpc)
RG      6.0 x 0.0 y 0.0 z Initial position; GMG+DISK=0, VG(3)=0
VG      -10.0 x 200.0 y 100.0 z Initial cluster velocity vector (km/sec), for a
        circular orbit.

MP      0.0 Total mass of Plummer sphere (in scaled units).
AP      1.0 Plummer scale factor (N-body units; square saved in AP2).
MPDOT   1.0 Decay time for gas expulsion (MP = MP0/(1 + MPDOT*(T-TD)).
TDELAY  1.0 Delay time for starting gas expulsion (T > TDELAY).

SEMI    0.0005 Max semi-major axis in model units (all equal if RANGE = 0).
ECC     -2.0 Initial eccentricity (< 0 for thermal distribution).
RATIO   1.0 Mass ratio M1/(M1 + M2); (= 1.0: M1 = M2 = <M>; not #20 > 1).
RANGE   250 Range in SEMI for uniform logarithmic distribution (> 0).
NSKIP   1 Binary frequency of mass spectrum (#20 < 2; body #1 first).
IDORM   0 Indicator for dormant binaries (>0: merged components).
ICIRC   0 Eigenevolution (=1: Kroupa & Mardling; =2: Kroupa 199
```